Tensile Failure and Fracture of Three-Dimensional Brittle Nanolattices

Thesis by

Arturo José Mateos Arrieta

In Partial Fulfillment of the Requirements

for the Degree of

Doctor of Philosophy in Aeronautics

California Institute of Technology

Pasadena, California

2018

(Defended 30 May 2018)

Arturo José Mateos Arrieta

ORCID: 0000-0002-9306-3531

Para mis mejores y eternos amigos – Mia, Alejandro y Andrea.

Acknowledgements

Many people helped me throughout this journey, and therefore there are many people I need to thank. Prime among them is my adviser Professor Julia Greer. I would be entirely astray without her guidance, her expertise, her encouragement, and her tremendous patience. I am deeply grateful for the academic freedom that she has given me throughout my time at Caltech and I am sincerely honored to have had the opportunity to work with such an incredible human being.

Thanks are also due to members of my dissertation committee, Professor Katherine Faber, Professor Guruswami 'Ravi' Ravichandran, and Professor Sergio Pellegrino, for their time and their commitment. I am extremely grateful to the academically-gifted professors with whom I have interacted. I make a special acknowledgement to Professor Michael Ortiz, who introduced me to the GALCIT family and exposed me to a unique way of thinking. I am grateful for the many opportunities that I had to discuss my work with Professor Dennis Kochmann, Professor Ares Rosakis, and Professor Kaushik Battacharya.

Many thanks to the current members of the Greer Group for ideas, discussions, support, and friendship, in particular, Daryl Yee, Carlos Portela, and Bryce Edwards; my officemates, Dylan Tozier and Xiaoxing Xia; and lastly, Ottman Tertuliano, who later became instrumental during the weekends. I could not have done all this work without the training and guidance of past group members and colleagues; thank you Lucas Meza for your mentorship and Lauren Montemayor for your guidance. I also need to thank Alessandro Maggi, Zach Aitken, David Chen, Wendy Gu, Viki Chernow, and Alex Zelhofer for invaluable intellectual discussions and support.

Thanks to my friends at the Student-Faculty Program Office. In particular, Carol Casey and Candace Rypisi for always keeping me in mind. I need to thank Felicia Hunt and Kate McAnulty for their endless support, especially when I needed them the most. The experiments of this thesis required the use of numerous labs and user facilities around Caltech. I am especially grateful for the Kavli Nanoscience Institute (KNI), Professor Harry Atwater, and Professor Nate Lewis for their support and for the availability of facilities throughout my time here.

I would like to thank those with unique resourceful offices at Caltech who helped enrich my experience. Thank you Christine Ramirez for making everything run smoothly; thank you Jim Barry for giving me an artistic outlet; and thank you Lydia Suarez for making Caltech feel like

home. I am also thankful and honored to have been part of the Keck Institute of Space Studies in which I was lucky enough to get to know Michele Judd.

Friends played a key role in my graduate school experience. Thank you Arnold Deffo and Matteo Ronchi for being there every week. Jason and Susie Schlup, Nathan Martin, and Noah Braun — thank you for making this journey a fun one. Special thanks to David and Nikky Huynh for letting me get to know you and for being there since the very first day.

I have had the opportunity to work with and mentor a number of outstanding students during my time at Caltech. I truly valued my research experiences while I was an undergrad so it was a great pleasure to be able give back to the next generation of scientists and engineers. Thank you Katrina Gonzalez, Sean Harris, Jake Larson, Talia Minear, and Zach Zimmerman for all your hard work, and I wish you all the best in your future careers.

Abstract

The emergence of a new class of cellular solids, i.e., nano- and micro-architected materials, poses the question of whether they can be characterized as a continuum solid. Extensive research has shown that these ultralight and strong structural metamaterials are particularly attractive for mechanically-demanding applications; yet their susceptibility to flaws, fracture behavior, and discrete-continuum duality remains relatively unexplored. In the course of this work, we report the fabrication and tensile-to-failure response of three-dimensional ceramic nanolattices, comprised of $50nm$-thick alumina tubes that are arranged into periodic $5um$-wide octet-truss unit cells, with and without pre-fabricated through-thickness center notches oriented at different angles to the loading direction. In-situ uniaxial tensile experiments revealed that for all notch orientations, failure always initiated at the notch root, as would be in a monolithic material, with the tube walls at nodal junctions fracturing first, followed by instantaneous crack propagation through the discrete lattice architecture along nodal planes orthogonal to the loading direction. Measured tensile strength of $27.4MPa$ was highest for the unnotched samples and decreased systematically with the increase of notch orientation to its minimum of $7.2MPa$ in the orthogonally-notched samples. We found the specific tensile strength of hollow-tube octet alumina nanolattices to be $\sim 4x$ higher than what has been reported for architected and bulk materials at similar low densities. Three-dimensional finite element simulations closely reproduce the observed failure mechanism and trends in failure strength. A direct comparison is made between the experimental measurements, finite element simulations, and predictions of linear elastic fracture mechanics for a self-similar monolithic tensile samples made out of an ideally-brittle solid. Results are in good agreement with the scaling of failure strengths from classical mode I fracture criteria and suggest that trajectory of crack propagation can be adequately explained by considering the connectivity of the lattice architecture. These findings imply that the continuum nature of nano-architected materials offers predictability of failure stresses, which helps enable the development of advanced materials through informed architectural design.

Contents

Acknowledgements **iv**

Abstract **vi**

List of Figures **viii**

List of Tables **xvii**

1 Introduction **1**

1.1 Overview of Architected Materials 1

1.2 Approach and Objectives 2

2 Design and Fabrication **4**

2.1 Center-Notched Tension Design for Three-Dimensional Nanolattices 4

2.2 Fabrication of Nano-Architected Center-Notched Tensile Specimens 4

2.3 Creating an Architected Hollow-Tube Gauge section 8

2.4 Sample Survival Rate 9

2.5 Relative Density Calculations 10

3 Experimental Methods **13**

3.1 Introduction 13

3.2 In-situ Nanomechanical Experiments 13

3.3 Data Analysis Methods 14

4 Tensile Response of Nanolattices **18**

4.1 Specific Tensile Strength of Hollow Octet Nanolattices 19

4.2 Weibull Statistical Analysis 20

4.3 Failure Surface Morphology 23

4.4 Failure Mechanisms 25

5 Tensile Response of Flaw-Containing Nanolattices **27**

5.1 Introduction . . . 27

5.2 Path of Crack Propagation . . . 28

5.3 Onset of Failure . . . 28

5.4 Weibull Statistical Analysis . . . 29

6 Continuum Approach to Center-Notched Tension Specimens **32**

6.1 Motivation . . . 32

6.2 Linear Elastic Fracture Mechanics . . . 32

6.2.1 Direction of Fracture Initiation . . . 36

6.2.2 Onset of Failure . . . 38

7 Continuum-Discrete Aspect of Three-Dimensional Hollow Octet Nanolattices **41**

7.1 Introduction . . . 41

7.2 Path of Crack Propagation . . . 43

7.3 Onset of Failure . . . 43

7.4 Tensile-Shear Stress Criterion . . . 44

7.5 Net Section Yielding . . . 47

7.6 Stiffness analysis . . . 52

7.7 Failure Envelope . . . 54

7.8 Finite Element Modeling . . . 55

8 Conclusions **62**

8.1 Open Questions . . . 63

A Supplemental Videos **65**

B Experimental Data **67**

C Details of Experimental Setup **77**

D Details of Finite Element Simulations **79**

Bibliography **82**

List of Figures

2.1 Schematic representation of the multi-step fabrication process employed to create hollow tube tensile nanolattices. The process starts by designing the lattice unit cells and using these files as input during the two-photon lithography direct laser writing (DLW) process to write a monolithic polymer lattice. The sample is then coated with alumina using an atomic layer deposition (ALD) process. One edge of the sample is milled using a focused ion beam (FIB) to expose and etch away the polymeric core using an O_2 plasma barrel asher. The final tensile sample consists of a hollow tube nanolattice gauge section supported by polymer-alumina composite structures. 5

2.2 Architected center-notched tension specimen geometry and constituent features. (A-D) Scanning electron micrographs show an unnotched and notched specimen and their gauge section features. (A-B) The gauge section consists of a 27 x 17 x 2 array of octet unit cells (scale bar: $50\mu m$). (C) Octet unit cells are tessellated in space to generate an architected gauge section (scale bar: $5\mu m$). (D) Each octet unit cell is composed of hollow $3.3\mu m$-long tubes with a mean radius r of $491 \pm 62nm$ (scale bar: $1\mu m$). (E) Computed-aided designs illustrate a representative octet unit cell with a unit cell length l of $4.72 \pm 0.03\mu m$ and a wall thickness t of $50nm$. 6

2.3 SEM images of fabricated architected notched tensile specimens. (A) Specimens are subjected to a uniaxial tensile load by displacing a tension grip upwards. (B-E) SEM images show a notched specimen and its gauge section features. (B) The gauge sections are pre-fabricated with an inclined notch with fixed length-to-width ratio, $2a/W$ of 0.45; the notch orientation β varies with respect to the direction of loading. (C) The notch is designed by omitting tubes during the fabrication process. (scale bar: $5\mu m$). (D) Unit cells are composed of hollow $3.3\mu m$-long tubes with a mean radius r of $491 \pm 62nm$ (scale bar: $1\mu m$). (E) The gauge section consists of hollow tube alumina unit cells with a few polymer-composite unit cells near the boundaries. 7

2.4 Center-notch geometry generated by MATLAB scripts. (A) Architected gauge sections of notched samples contain a pre-defined through-thickness notch composed of a collection of omitted tubes and nodes with relative notch lengths of $2a/W = 0.45$ and notch orientations varying from 0 to 90 degrees with respect to the direction of loading. (B-C) Close-up MATLAB image of notch oriented at 63.4 degrees and corresponding SEM image of final sample. 8

2.5 Focused Ion Beam (FIB) milling is employed to expose the polymeric core by removing sacrificial beams. 9

2.6 Etching profile. Sacrificial beams are removed from designated sites from both sides of the gauge section to expose the polymeric core to oxygen plasma. The duration of the etching process depends on the number of openings and the distance between the openings and the wavefront of polymer. Afterwards, the gauge section consists of hollow alumina tubes. 10

2.7 Samples were etched in O_2 plasma barrel asher and monitored to determine the etching rate and the total amount of time required to etch away the gauge section only without affecting the integrity of the support structures. 11

2.8 Most samples did not survive the O_2 plasma etching due to undesirable etching away from the gauge section. (A) For example, etching will simultaneously start at the gauge section and at the bottom support where defects were found. Since the etching rate is higher for the support compared to the tortuous paths of the gauge section, then the support will be completely hollowed out before the gauge section is ready for the tension experiment. (B-C) Cracks usually formed at the interface between the bottom support and the substrate, which propagated due to the shrinkage of the polymeric core and stress concentrations in the alumina thin film. The final tensile specimens were designed to alleviate stresses on the thin film and prevent the formation of cracks after the resin development and etching processes. 12

3.1 Custom tension grip used to test nano-architected tensile samples. The tension grip was machined on the head of a $0.8mm$ stainless steel screw by electrical discharge machining. 14

3.2 Representative displacement data for an unnotched sample and corresponding displacement and strain rates as a function of time. After initial settling events, all samples are loaded under constant strain rate conditions. 15

3.3 Displacement and strain for the hollow gauge section only can be obtained by subtracting the contribution of the additional compliance from the effective compliance recorded by the nanomechanical instrument. 16

3.4 Comparison between raw data, compliance-corrected data, and video-assisted corrected data. 17

4.1 Stress-strain response of unnotched samples. The Young's modulus is averaged over all samples is also plotted and shown as a dashed line. For visual simplicity, one representative curve has been highlighted (purple). 19
4.2 Cyclic loading of an unnotched sample. Minimal degradation of elastic properties is seen after 10 loading-unloading cycles. 20
4.3 Specific tensile strength versus relative density. Architected lattices known to be tested in tension and material groups have also been plotted for comparison. 21
4.4 Tensile strength of material groups and architected materials known to be tested in tension. 22
4.5 Weibull probability diagram for unnotched specimens. The Weibull modulus is denoted by the slope of the linear fit. Guidelines for a survival probability (the fraction of samples that would survive a given stress level) of 95% and 10% are also included for visual assistance. 23
4.6 Failure surface morphology of center-notched tensile samples. SEM images show crack propagation from crevices at nodal junctions; arrows indicate path trajectories across tube wall. Scale bar denotes $5\mu m$, unless stated otherwise. 24
4.7 Failure surface morphology of unnotched tensile samples. SEM images of failure surface morphology and corresponding failure load. (Row A) A low percentage of fabricated samples exhibited high tensile strengths with failure localized in one plane of nodes perpendicular to the applied load. These samples make up the set of unnotched specimens used in this work. (Row B) The majority of unnotched tensile samples failed at lower strengths coupled with uneven failure surfaces and discarded from the analysis section of this work. Scale bar denotes $50\mu m$. 24
4.8 Failure mechanisms of hollow-tube nanolattices can be simplified to the energetic competition between fracture of the tube walls and buckling instabilities, as described in ref. [1]. 26

5.1 Failure surface morphology for notched and unnotched specimens (scale bar: $25\mu m$). . 27
5.2 Global and local failure surface morphology. Scanning electron micrographs of (A) notched sample after failure (scale bar: $10\mu m$) and (B) local crack propagation trajectory on nodal junctions and through hollow tubes (scale bar: $2\mu m$). 28

5.3 Representative stress-strain data for notched and unnotched specimens. All samples show linear-elastic behavior up to catastrophic failure. The mean Young's moduli (dotted line) for each case is also plotted. The point at failure is denoted with an 'x' for all samples. 29

5.4 Stress at failure for all notched samples as a function of notch orientation. The failure strength for the unnotched samples is also plotted as a band corresponding to a 95% confidence interval centered at the mean strength of all unnotched samples. 30

5.5 Weibull probability diagram for unnotched and notched specimens. The Weibull modulus (denoted by the slope of each linear fit) is consistent for all notched cases and similar to the unnotched case. Guidelines for a survival probability of 95% and 10% are also included. 30

5.6 Weibull distribution for unnotched and notched tensile specimens. (A) The probability density function for all unnotched and notched cases, and (B) the corresponding Weibull modulus, which is the shape factor of the distribution; that is, as m decreases, the distribution widens. 31

6.1 Evaluation of local stresses near the crack tip. 33

6.2 Modes of fracture. There exists three types of crack opening: Mode-I denotes symmetric crack opening, Mode-II is characterized by an antisymmetric separation of the crack surfaces, and Mode III describes the separation due to relative displacements in the direction tangent to the crack front. In this work, we consider in-plane mixed-mode loading where mode-I and mode-II are superimposed while mode-III is not present. . . 33

6.3 LEFM stress-based analytical predictions for crack deflection angle for a center-cracked linear-elastic continuum plate. The deflection angle defines the direction of fracture initiation as a function of notch orientation. 37

6.4 LEFM stress-based analytical predictions of stress at failure for a center-cracked linear-elastic continuum plate. 39

6.5 LEFM stress-based analytical predictions for mixed-mode failure of a center-cracked linear-elastic continuum plate. 40

7.1 As the characteristic features of three-dimensional architected materials are reduced to the microscale, a question arises of whether they are better described as discrete structures or continuum-like materials. 41

7.2 Crack deflection angle for hollow-tube octet nanolattices and analytical predictions for an equivalent center-cracked linear-elastic continuum plate. The error bars for the experimental data denote one standard deviation. The continuum-based predictions consist of a shaded area defined by a characteristic distance r_c of $0.04\mu m$ and $2\mu m$, respectively. 42

7.3 Normalized tensile strength for hollow-tube octet nanolattices and analytical predictions for an equivalent center-cracked linear-elastic continuum plate. Variation of normalized critical stress with crack orientation of nanolattices, where error bars denote one standard deviation. Predictions for a plate according to stress-based continuum criteria and net-section strength criterion are also plotted, where the top and bottom boundaries of the shaded area are defined by a characteristic distance r_c of $0.04\mu m$ and $2\mu m$, respectively. The stress at failure for unnotched specimens is plotted as a band centered at the bootstrapped mean and bounded by a 95% confidence interval. 45

7.4 Equivalent linear-elastic center-cracked plate. 47

7.5 Relationship between the stress at failure and flaw length for a center-cracked plate. For an infinite sample, the stresses will follow the green dashed line where failure stresses, σ_f, depend on the flaw size, a, and parameterized by the stress intensity factor, K. If the stresses at failure are associated with yielding at the net section, then a conventional stress analysis can be used to describe the fracture stresses. 48

7.6 Evaluation of net-section yielding by relating the stress at failure with the flaw size. The black curve indicating a smooth, continuous relationship between the stress at failure and the notch length is generated by a K-parameterized regime in the center bounded by two linear regimes at short and long notch lengths. The curve depicted in this plot was generated by fitting a curve through the average dta points for the unnothced case and the 90°-notched specimen, which is the only notched specimen with a horizontal notch. However, by plotting the projected notch length for all other angled specimens, we see that they fall below the net section yielding limit and follow a similar scaling as predicted by the fracture mechanics analysis. 50

7.7 The net cross-sectional area of a notched sample is defined as the gross area of the ligaments to the side of the notched and perpendicular to the applied tensile load. (A) SEM image illustrating the net cross-sectional area of a 90°-notched specimen, which is denoted by the highlighted red areas. (B) SEM image of the top view of the cross-sectional area. 51

7.8 A net section strength criteria can be used to evaluate the strength of the ligaments of notched specimens. This criteria describes the stress at failure for notched specimens as a fraction of the tensile strength of the material (that is, the measured stress at failure for the unnotched case) and dictated by the net cross-sectional area. The piece-wise linear fashion of the curve is a result of the discrete nature of the architected material. As the length of the unit cell decreases, this curve becomes smooth and continuous; as expected for a monolithic solid. 53

7.9 Stiffness for hollow octet nanolattices tested in this study and that of an equivalent linear-elastic solid as a function of notch orientation. The stiffness for the unnotched samples are also plotted as a band corresponding to a 95% confidence interval centered at the mean stiffness for all unnotched samples. 54

7.10 Mixed-mode fracture loci for hollow octet nanolattices and for an equivalent center-notched linear-elastic continuum solid. 55

7.11 Contributions of the T-stress in mixed-mode loading for a center-notched linear-elastic continuum solid and hollow octet nanolattices. 56

7.12 Finite element models resembling as-fabricated center-notched tensile geometries. (A-C) SEM image and corresponding finite element model. (D-E) Octet unit cells are composed of shell elements. 57

7.13 Fracture surface morphology and stress-strain response for notched and unnotched nanolattices from finite element simulations. (Rows A, B) Finite element models of octet nanolattices for each notch orientation before and after tensile failure. (Row C) Stress-strain response (solid line) for notched and unnotched nanolattice samples under uniaxial tensile loading were plotted. The point of catastrophic failure is denoted by an ‘x’ for all samples and the Young’s modulus for each notch orientation is plotted by a dashed line. 58

7.14 Experimental and finite element simulation results for tensile strength of notched and unnothced nanolattices as a function of notch orientation. 59

7.15 Fractographic examination of tensile samples and corresponding finite element simulations. (A) SEM image of a notched sample after tensile failure with arrows pointing at the initial notch. Failure occurred at all nodes along two parallel lattice planes that were adjacent to the notch ends, orthogonal to the loading direction (scale bar: $10\mu m$). (B) Zoomed-in SEM image of fractured nodal junctions and neighboring hollow tubes within those failure planes (scale bar: $2\mu m$). (C) FE-generated contour plots of von Mises stress distributions in the specimen notched at 90 degree with respect to applied tension. Red boxes denote the most stressed nodal junctions, with a maximum stress of 5.167 GPa, where brittle fracture initiated. (D) FE-generated contour plots of von Mises stress distributions in the unnotched nanolattices. (E and F) FE-generated fracture surface morphology of notched nanolattices displayed in the same orientation and relative magnification as SEM images in (A,B). 60

7.16 Failure propagation paths as a progressing of applied strain of all notched nanolattices subjected to uniaxial tensile loading. 61

8.1 Fracture toughness of architected materials. (A-B) SEM image of a single edge notch bending specimen illustrating the notion of fabricating a three-dimensional specimen whose characteristic features at the unit cell length (l) are small compared to the flaw size (a) and the global dimensions of the sample (W). (Row C) Images of FE efforts to characterize the complex stress state of three-dimensional architected materials across multiple length scales. FEA images courtesy of Yong Wei Zhang and Hunag Wei. . . . 64

A.1 VIDEO S1: In-situ nanomechanical experiment of unnotched sample with corresponding load-displacement data. 65

A.2 VIDEO S2: In-situ nanomechanical experiment of notched sample with corresponding load-displacement data. 65

A.3 VIDEO S3: Visualization of MATLAB script capable of generating a lattice geometry with a center notch of varying orientation. 66

B.1 Representative load-displacement data for notched and unnotched specimens. all tested samples show linear-elastic behavior up to catastrophic failure. The mean stiffness (dotted line) for each case is also plotted. The point at failure is denoted with an 'x' for all tested samples. 68

B.2 Normalized K_I, K_II, K_eff, and $T-$stress data. Contributions of the fracture mode is plotted as a function of notch orientation for a homogeneous isotropic elastic solid predicted from linear elastic fracture mechanics (LEFM) and also those from the nanomechanical experiments. 69

B.3 Experimental data for all tested samples: Failure load and Young's modulus. 70
B.4 Experimental data for all tested samples: Failure load and stiffness. 71
B.5 Experimental data for all tested samples: Failure load and average strain rate. 72
B.6 Experimental data for all tested samples: Young's modulus and averaged strain rate. . 73
B.7 Experimental data for all tested samples: stiffness and average strain rate. 74
B.8 Experimental data for all tested samples: Failure load and loading rate. 75
B.9 Experimental data for all tested samples: Young's modulus and loading rate. 76

C.1 Previous version of center-notched tension samples. 77
C.2 MATLAB scripts allowed for geometrically-indistinguishable samples and, more importantly, reproducible notch roots, which are the locations of high stress concentrations. For example, for a 90°-notched specimen, diagonal beams are present at the node closest to the notch root. If focused-ion beam milling was used to create the notch, then the integrity of these structural elements might be compromised and the material composition at this location might change due to ion bombardment. 78
C.3 XeF_2 etching enables the creation of the simple supports for three-point bending experiments at the microscale. After deposition a polymeric plate on top of a silicon substrate, XeF_2 can be used to selectively etch away the substrate and by tuning the etching parameters, a point support can be fabricated. A microscopic three-point bending specimen with a lattice architecture can then be placed on top of these supports. 78

D.1 Von Mises stress distribution from finite element analysis of the central region of the 90°-notched sample. The location of highest stress is at the node closest to the notch root. The finite element simulations were performed by Dr. Yong-Wei Zhang (Institute of High Performance Computing, A*STAR, Singapore) and Dr. Huang Wei (Northwestern Polytechnical University, Xian, China). 79
D.2 To evaluate the scaling of stress with distance from the notch root, the von Mises stresses for half unit cells were averaged and plotted as a function of distance where the origin is located at the first element closest to the notch. If the different averaging area is selected, the average stresses will vary since there is a high stress concentration at the nodes; therefore, a dedicated study must be performed to assign an appropriate area. The finite element simulations were performed by Dr. Yong-Wei Zhang (Institute of High Performance Computing, A*STAR, Singapore) and Dr. Huang Wei (Northwestern Polytechnical University, Xian, China). 80

D.3 The finite element simulations do not take into account the effect of the geometric and material defects on the fracture strength of nanolattices, as shown by the SEM image. It would be computationally expensive to model the details of the hollow tube intersections in the finite element model. Scale bar denotes $4\mu m$ The finite element simulations were performed by Dr. Yong-Wei Zhang (Institute of High Performance Computing, A*STAR, Singapore) and Dr. Huang Wei (Northwestern Polytechnical University, Xian, China). 81

List of Tables

2.1 Duration of each step during the fabrication process and testing phase. 10

7.1 Screening criterion to generate a net section yielding relationship between the stress at failure and flaw size. 50

7.2 Effective material properties and geometric constants used for computing the stiffness of an equivalent linear elastic plate as a function of notch orientation 53

Chapter 1

Introduction

1.1 Overview of Architected Materials

"Materials by Design" is becoming a household phrase, which highlights the need to develop advanced materials with custom-tailored properties that cannot be attained through conventional processing routes. A successful approach to attain such properties has been through architectural design of materials. Architected materials, similar to cellular solids, are assemblies of geometrical unit cells made up of an interconnected network of solid struts or plates that pack together to fill space in either a stochastic fashion such as in stochastic foams or in an ordered fashion. By combining constitutive material properties and architectural elements, properties such as stiffness, strength, toughness, thermal conductivity, diffusivity, and so forth can be tailored to meet requirements that were traditionally thought to be mutually exclusive.

The potential to achieve enhanced mechanical properties has fueled the recent development of architected materials and propelled their use as structural materials [2, 3]. Devices and large scale structures can be created to reap further mechanical enhancement by employing an architecture at the micro and nanoscale to access the advantageous properties offered by nanomaterials. An early successful example of this creative thinking comes in the form of polymeric and metallic foams, which exploit material size effects [4–16]. However, the stochastic nature of foams prevents the achievement of optimal structural efficiency and yields poor scaling of stiffness and strength with relative density. Recent efforts in fabrication techniques have advanced the development of nano-architected materials with controllable architectures with nanoscale features that harvest structural efficiency across length scales [17, 18]. Three profitable techniques capable of producing these novel materials involve self-propagating photopolymer waveguides [19–23], micro-stereolithography [24–26], and direct laser writing two photon lithography [22, 27].

Self-propagating photopolymer waveguides produces the highest throughput out of these techniques. This scalable technique relies on on the difference in index of refraction between crosslinked and the initial resin bath. Subsequent fabrication steps can be used to coat the polymer structures

with thin films, remove the polymer core, and obtain hollow structures composed of the deposited material. The lattice architecture can be easily modified by changing the waveguides direction; however this technique is restricted to generating unit cell geometries that are highly directional, which restricts the deformation mode to be bending of lattice bars. Micro-stereolithography is also capable of producing microlattices via a layer-by-layer additive process. This technique is able to generate monolithic polymeric lattices and hollow tube structures who deformation is stretching or bending-dominated architectures. Microlattices fabricated with self-propagating photopolymer waveguides and micro-stereolithography produce mm-sized unit cells and wall thicknesses dictated by the thin film deposition technique. This provides the potential to take advantage of material size effects but the dimensions of the unit cells are too large to actually exploit the size effects. Structural analysis can adequately describe the response of these microlattices. When the unit cell size is decreased to the length scales comparable to the wall thicknesses, the effective mechanical properties can be classified as material properties and the effective structure as nano-architected material, or structural metamaterial. Direct laser writing via two photon lithography enables the fabrication of these architected materials with characteristic features at the micro- and nanoscale. Their mechanical properties depend on the properties of the constituent nanomaterial and the structural response of the architecture. The mechanical properties of architected materials are generally characterized by their constituent material properties, relative density, which is defined as the volume fraction of the solid material divided by the representative volume of the unit cell and by the structural architecture, which is defined by the connectivity of the struts or faces comprising the unit cell of the cellular solid [28].

1.2 Approach and Objectives

Research on three-dimensional architected materials whose characteristic features are on the order of nanometers and micrometers has revealed their enhanced mechanical properties [1, 2, 24, 25, 29–35]. Extensive research has been conducted to investigate the compressive strength and stiffness of materials with lattice architectures as a function of their geometry, dimensions, and material properties [36–40]. Recent work on 3D lattices with characteristic dimensions on nanometer length scales demonstrates mechanical resilience [1], greater-than-predicted strength [29], recoverability of brittle ceramics [30], tunable acoustic band gaps [41] and photonic crystals with a complete photonic bandgap [42]. Little work has been done on tensile and fracture properties of nano- and micro-lattices, mainly because of the challenges associated with fabricating tensile specimens out of these materials and the required equipment for nanomechanical experiments. Existing work is mainly computational and limited to 2D architectures [43–53]; experimental studies on tensile and fracture response of 3D architected materials are scarce and mainly focused on the response of

pristine samples to uniaxial loads without taking into account flaws or their discrete-continuum duality, fundamental features of fracture [25, 31, 32].

The aim of this thesis is to develop an understanding of mechanical response of nano-architected materials under tensile loads and characterize its fracture behavior. The fabrication and mechanical characterization of three-dimensional hollow ceramic nanolattices is reported, whose features sizes are $50nm$ for the wall thickness, $5\mu m$ for the unit cell size, and $0.1mm$ for the gauge section length. Notched and unnotched micro-sized tensile samples were fabricated that contained differently-oriented center notches and in-situ uniaxial tension experiments were conducted to characterize their tensile-to-failure behavior. Results show that failure always occurred along the nodes within the lattice architecture, with fracture surface always orthogonal to the loading direction regardless of notch orientation. Fracture surface was formed by local failures at nodal junctions, tube wall rupture, and crack branching along preferred orientations that form a global failure surface morphology perpendicular to the applied load. Stress at failure decreased from $27.4MPa$ in the unnotched samples to $7.2MPa$ in the samples whose notch was oriented at 90 degrees with respect to loading direction; similar to an equivalent linear elastic continuum. The relationship between tensile failure strength and notch orientation is discussed in the framework of linear elastic fracture mechanics (LEFM) and shows that these materials occupy a previously unattained region in the specific tensile strength property space.

Chapter 2

Design and Fabrication

2.1 Center-Notched Tension Design for Three-Dimensional Nanolattices

We designed center-notched tensile specimens with a nano-architected gauge section and monolithic supporting structures that brace the gauge section at the top and bottom to ensure uniform loading. SEM images in Fig. 2.2 show the bottom support that is attached to the substrate and the top support that is inserted into a custom-made tension grip in the nanomechanical instrument. This shape of the supports was designed to minimize the stress concentrations and premature failure initiation at the interfaces between the gauge section and the supports. Fig. 2.2A shows the final sample that consists of a ceramic hollow-tube gauge section braced by polymer-alumina composite supports. Fig. 2.2A shows that the gauge section consists of 27 (height) x 17 (width) x 2 (thickness) octet unit cells. The individual unit cell dimensions were designed to have a length of $4.72 \pm 0.03 \mu m$, an average outer tube diameter of $981 nm$ with eccentricity of 1.1, and alumina tube wall thicknesses of $50 nm$ (Fig. 2.2C-E). This octet unit cell is a rigid 3D architecture with a nodal connectivity of 12 and cubic symmetry, which categorizes it as a stretching-dominated cellular solid with a low degree of structural anisotropy [36]. We fabricated most of the samples to contain a pre-defined through-thickness notch, which was composed of a collection of omitted tubes and nodes with relative notch lengths of $2a/W = 0.45$ and notch orientations varying from 0 to 90 degrees with respect to the direction of loading (Fig. 2.3).

2.2 Fabrication of Nano-Architected Center-Notched Tensile Specimens

Adequate consideration of the sample design must be taken into account for a proper tensile test at any length scale. The sample design must prevent induced stress concentrations and premature

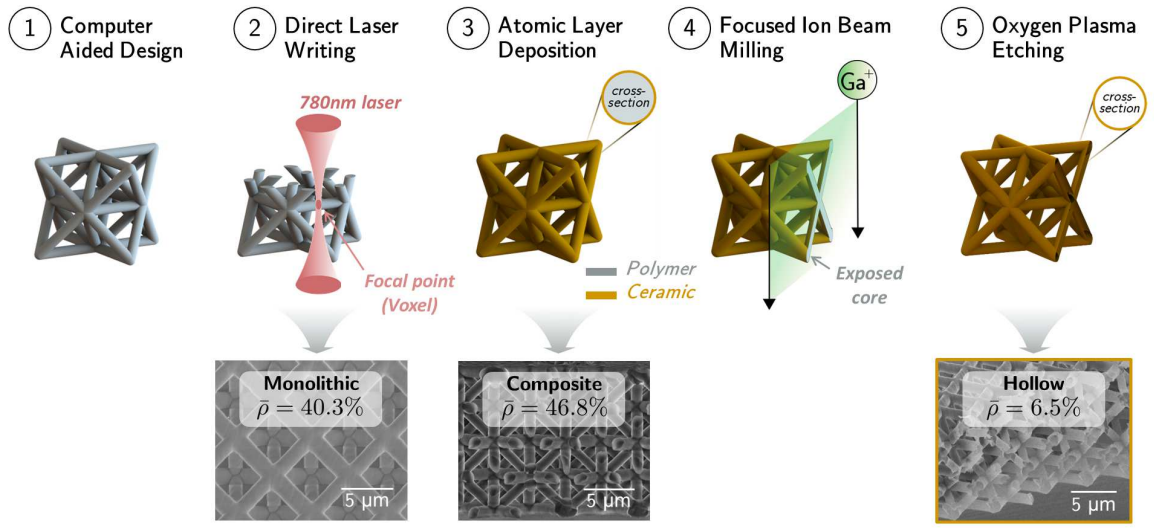

Figure 2.1: Schematic representation of the multi-step fabrication process employed to create hollow tube tensile nanolattices. The process starts by designing the lattice unit cells and using these files as input during the two-photon lithography direct laser writing (DLW) process to write a monolithic polymer lattice. The sample is then coated with alumina using an atomic layer deposition (ALD) process. One edge of the sample is milled using a focused ion beam (FIB) to expose and etch away the polymeric core using an O_2 plasma barrel asher. The final tensile sample consists of a hollow tube nanolattice gauge section supported by polymer-alumina composite structures.

failure initiation sites, introduced by the required supporting structures bracing the gauge section. The nanolattices in this work were designed to emulate conventional conditions for fracture experiments in monolithic materials, where samples take a dog-bone shape with a central gauge section of uniform width.

A multi-step fabrication process is employed to fabricate nanomechanical tensile specimens; as illustrated in Fig. 2.1. The gauge section geometry was generated using MATLAB scripts and the supporting structures were designed using a CAD model generated with Solidworks (Dassault Systmes). These CAD models were also used to determine the relative density of the samples. The notch geometry was designed to resemble naturally occurring cracks in lattices. For materials with lattice architectures, notches come in the form of a combination of structural imperfections, such as unconnected or broken struts and missing nodes. We fabricated some of the samples to contain a pre-defined through-thickness notch, which was composed of a collection of omitted tubes with relative notch lengths of $2a/W = 0.45$ and notch orientations varying from 0 to 90 degrees with respect to the direction of loading. Notch orientations are related to the in-plane cubic symmetry of the octet ranging from 0 to 90 degrees; that is, $\beta = \arctan(i) \cdot \left(\frac{180}{\pi}\right)$, where $i = [0, 0.5, 1, 2, 8, \infty]$. Fig. 2.4 illustrates the various notched gauge section designs used in this work. The addition of the notch to the pre-defined gauge section designs provides consistent means of fabricating nearly identical samples. The designs were used as input to the lithographic instrument. A visual representation of the notch generating scripts is provided with *Video S3*.

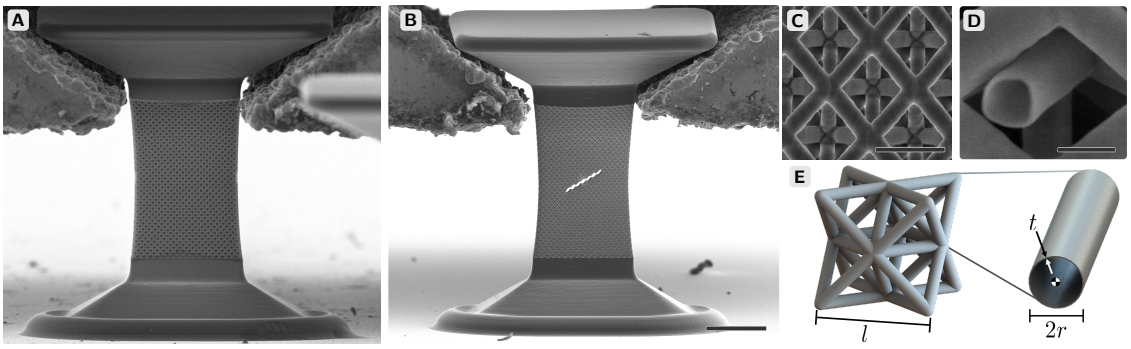

Figure 2.2: Architected center-notched tension specimen geometry and constituent features. (A-D) Scanning electron micrographs show an unnotched and notched specimen and their gauge section features. (A-B) The gauge section consists of a 27 x 17 x 2 array of octet unit cells (scale bar: $50\mu m$). (C) Octet unit cells are tessellated in space to generate an architected gauge section (scale bar: $5\mu m$). (D) Each octet unit cell is composed of hollow $3.3\mu m$-long tubes with a mean radius r of $491 \pm 62nm$ (scale bar: $1\mu m$). (E) Computed-aided designs illustrate a representative octet unit cell with a unit cell length l of $4.72 \pm 0.03\mu m$ and a wall thickness t of $50nm$.

Fabrication of all samples starts with the writing of a polymer sample made out of photoresist (IP-Dip photoresist, Nanoscribe GmbH) using two-photon lithography (TPL) direct laser writing (DLW) in a Photonic Professional lithographic system (Nanoscribe GmbH). Samples are written using laser powers in a range from 15-20 mW and a writing speed of 20000-50000 $\mu m/s$. The laser power is used to control the effective diameter of the tubes, and the speed varies slightly during the writing process to control the quality of the supporting structures. The samples were written on silicon wafers that were silanized to improve the adhesion between the sample and the substrate. The silanization process is essential to avoid delamination under tensile loading conditions.

	Silanization procedure
1	Prepare solution A by mixing: 9.3ml Ethanol, 0.5ml deionized H_20, and 0.2ml acetic acid.
2	Sonicate silicon chip in IPA for 15 mins
3	Sonicate chip in deionized H_20 for 15 mins
4	Add 0.2ml of silane to solution A. Shake well.
5	Pour solution A into a glass petri dish.
6	Take out Si chip from sonicator, dry chip briefly.
7	Immerse chip in solution A for 2 mins. Agitate gently by swirling the glass petri dish slowly.
8	Dip chip into a beaker of Ethanol and swirl gently.
9	Place chip onto hot plate at $\sim 90°$ for 2 hrs.

These samples were then critically-point dried with an Autosamdri 931 (Tousimis) and conformally coated with $50nm$ of alumina using atomic layer deposition (ALD) in a Nanotech S200 (Cambridge Inc.). We used oxygen plasma to etch away the polymeric core from the gauge section of the nanolattice. This was accomplished by Focused Ion Beam (FIB) milling of auxiliary struts,

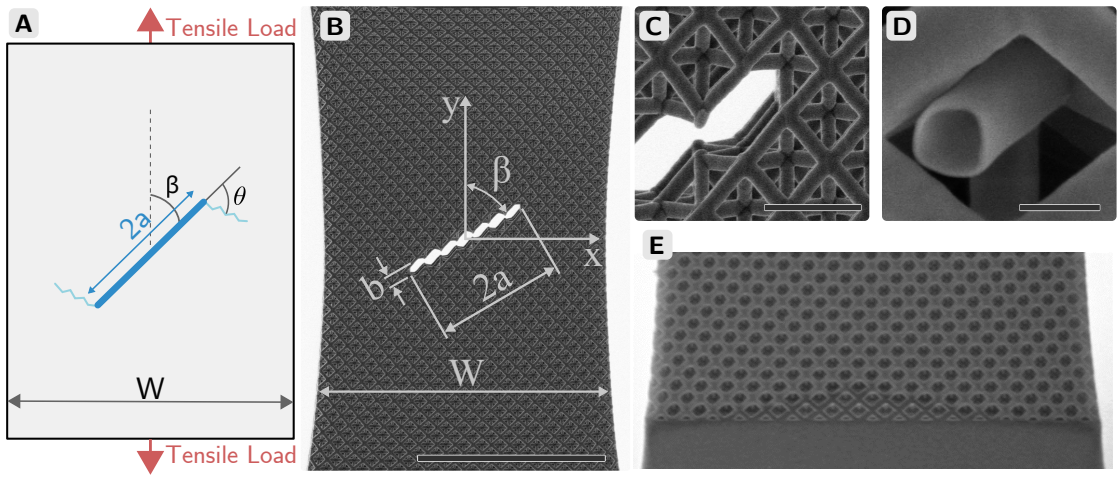

Figure 2.3: SEM images of fabricated architected notched tensile specimens. (A) Specimens are subjected to a uniaxial tensile load by displacing a tension grip upwards. (B-E) SEM images show a notched specimen and its gauge section features. (B) The gauge sections are pre-fabricated with an inclined notch with fixed length-to-width ratio, $2a/W$ of 0.45; the notch orientation β varies with respect to the direction of loading. (C) The notch is designed by omitting tubes during the fabrication process. (scale bar: $5\mu m$). (D) Unit cells are composed of hollow $3.3\mu m$-long tubes with a mean radius r of $491 \pm 62nm$ (scale bar: $1\mu m$). (E) The gauge section consists of hollow tube alumina unit cells with a few polymer-composite unit cells near the boundaries.

which enabled the exposure of the internal polymer to oxygen plasma with minimal ion bombardment in critical regions of the sample, e.g., the vicinity of the notch root. This multi-step process allowed us to create hollow-tube alumina nanolattices without affecting the structural integrity of the supporting structures.

The resulting polymeric sample is then critically-point dried with a Autosamdri 931 (Tousimis) and conformally coated with $50nm$ of aluminum oxide (alumina) using atomic layer deposition (ALD). Deposition is done at $150°C$ in a Cambridge Nanotech S200 ALD system using the following steps: H_2O is pulsed for 15ms, the system is purged for 20s, trimethyl aluminum (TMA) is pulsed for 15ms, the system is purged for 20s, and the process is repeated. The carrier gas is nitrogen, which is used at a flow rate of $20sccm$. The process was repeated for 500 cycles to obtain the desired thickness coating. The thickness of the coatings was verified using spectroscopic ellipsometry with an alpha-SE Ellipsometer (J.A. Wollam Co., Inc.). A detailed study on the mechanical properties of ALD alumina can be found in ref. [54].

After deposition, a focused ion beam (FIB) (Versa 3D DualBeam, FEI) is used to mill away auxiliary beams of the sample to expose the polymer to air, as shown in Fig. 2.5. Once the polymer is exposed, samples are placed into a SP100 oxygen plasma system (Anatech Ltd.) for between 50-80 hours at a pressure of $100mTorr$ and at $100W$ of power in order to remove the polymer from the gauge section. It is possible to determine whether the polymer has been fully etched away by looking for any contrast change in the beams using a scanning electron microscope, as shown in Fig.

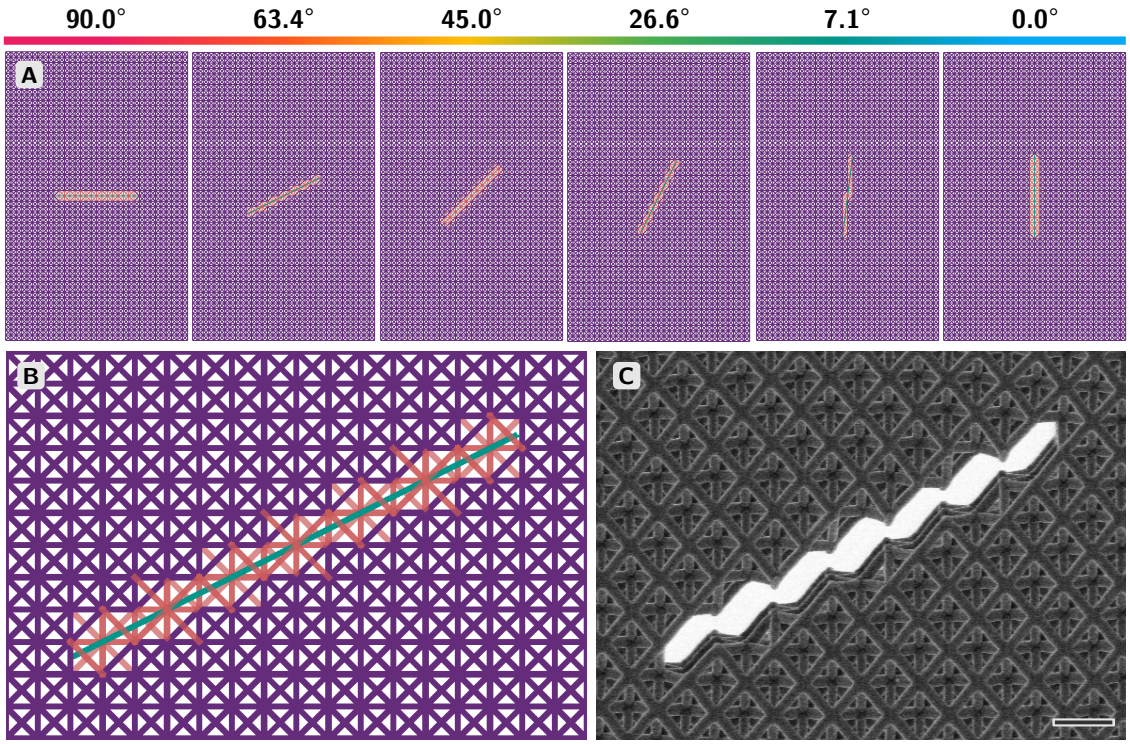

Figure 2.4: Center-notch geometry generated by MATLAB scripts. (A) Architected gauge sections of notched samples contain a pre-defined through-thickness notch composed of a collection of omitted tubes and nodes with relative notch lengths of $2a/W = 0.45$ and notch orientations varying from 0 to 90 degrees with respect to the direction of loading. (B-C) Close-up MATLAB image of notch oriented at 63.4 degrees and corresponding SEM image of final sample.

2.6. For tensile specimens, it is crucial to regularly measure the etching profile to prevent structural damage of the supporting structures.

2.3 Creating an Architected Hollow-Tube Gauge section

To expose and etch away the polymer core, auxiliary struts were included in the gauge section designs and milled by focused-ion beam (FIB) milling to provide an opening for oxygen plasma to ash the polymer using a SP100 oxygen plasma system (Anatech Ltd.) (Fig. 2.5 and Fig. 2.6). The addition of auxiliary struts enables the exposure of the internal polymer with minimal ion bombardment to sacrificial material and no damage in critical regions of the sample, such as the vicinity of the notch root. Excessive ion bombardment could induce material and geometric defects, such as changes in the material composition [55–57], and introduce external flaws in the form of missing struts or nodes. The final sample consists of a ceramic hollow-tube gauge section supported by polymer-alumina composite structures.

The progression of the etching profile can be evaluated by imaging the samples in an SEM

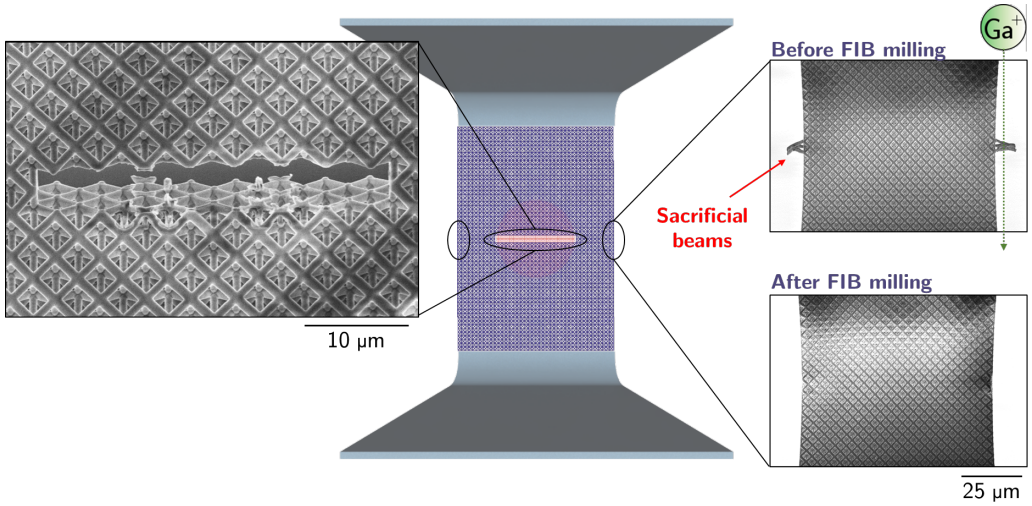

Figure 2.5: Focused Ion Beam (FIB) milling is employed to expose the polymeric core by removing sacrificial beams.

to nondestructively determine the amount of polymer that has been removed. Fig. 2.7 shows a representative sample that shows the location of monolithic polymer-alumina unit cells and hollow-tube alumina unit cells in the gauge section, which is denoted by a change in contrast of the sample. Samples were etched in O_2 plasma barrel asher and monitored to determine the etching rate and the total amount of time required to etch away the gauge section only without affecting the integrity of the support structures (Fig. 2.7). This delicate and time-consuming process was performed for all gauge sections with and without a notch, separately. Depending on the notch orientation, the etching process lasted more than 60 hours.

2.4 Sample Survival Rate

There are several critical steps in the fabrication process that reduced the sample survival rate. More than 1000 samples were successfully written on silicon substrates but $\sim$ 114 samples were used during the analysis of this work. Most samples were successfully developed, critically point dried, and coated with ALD alumina. Sacrificial beams and a pre-defined notch allowed for a high survival rate after focused ion beam milling; which enabled identical samples regardless of the presence of a notch or notch orientation. The survival rate after the etching process was low ($\sim$ 10%) making this the critical step in the fabrication process. The low survival rate is mostly due to the high probability of finding an unwanted defect in the alumina thin film which lets O_2 plasma etch the substrate at undesirable locations (see Fig. 2.8). For example, if a defect (in the form of a crack or void) is located at the interface between the bottom support and the substrate, then etching will simultaneously start at the gauge section and at the bottom support. Since the etching rate

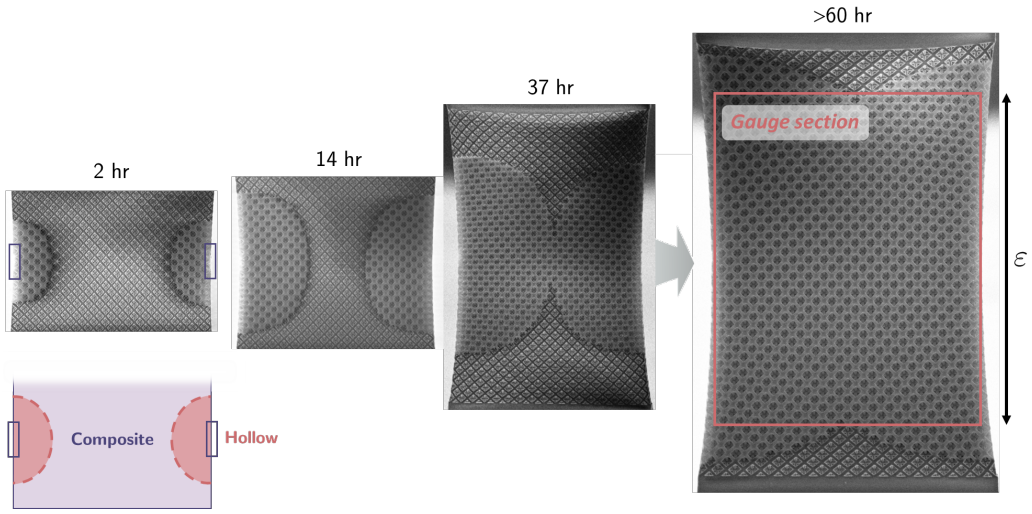

Figure 2.6: Etching profile. Sacrificial beams are removed from designated sites from both sides of the gauge section to expose the polymeric core to oxygen plasma. The duration of the etching process depends on the number of openings and the distance between the openings and the wavefront of polymer. Afterwards, the gauge section consists of hollow alumina tubes.

is higher for the support compared to the tortuous paths of the gauge section, then the support will be completely hollowed out before the gauge section is ready for the tension experiment. A visual inspection of the supports with a microscope does not necessarily allow the determination of failed samples, which leads to evaluating the integrity of the samples during the testing phase. The minimum hours required to fabricate an tension specimen with an architected gauge section is $>$ 84.5 $hr/sample$, as listed in Table 2.1.

Table 2.1: Duration of each step during the fabrication process and testing phase.

#	Process	Duration	Approx. survival rate
1	Substrate preparation	1 $hr/sample$	99%
2	Two-photon lithography	4 $hr/sample$	90%
3	Resin development	0.5 $hr/sample$	90%
4	Critical point drying	1 $hr/sample$	90%
5	Thin film deposition	6 $hr/sample$	90%
6	Focused ion beam milling	1 $hr/sample$	90%
7	O_2 plasma etching	$>$ 70 $hr/sample$	10%
8	Tension experiment	1 $hr/sample$	80%
	TOTAL	$>$ 84.5 $hr/sample$	10%

2.5 Relative Density Calculations

To calculate the volume of the final hollow-tube ceramic specimens, a SolidWorks model of the unit cell was used (Fig. 2.1). Dimensions of the structure in SolidWorks were set using the measured

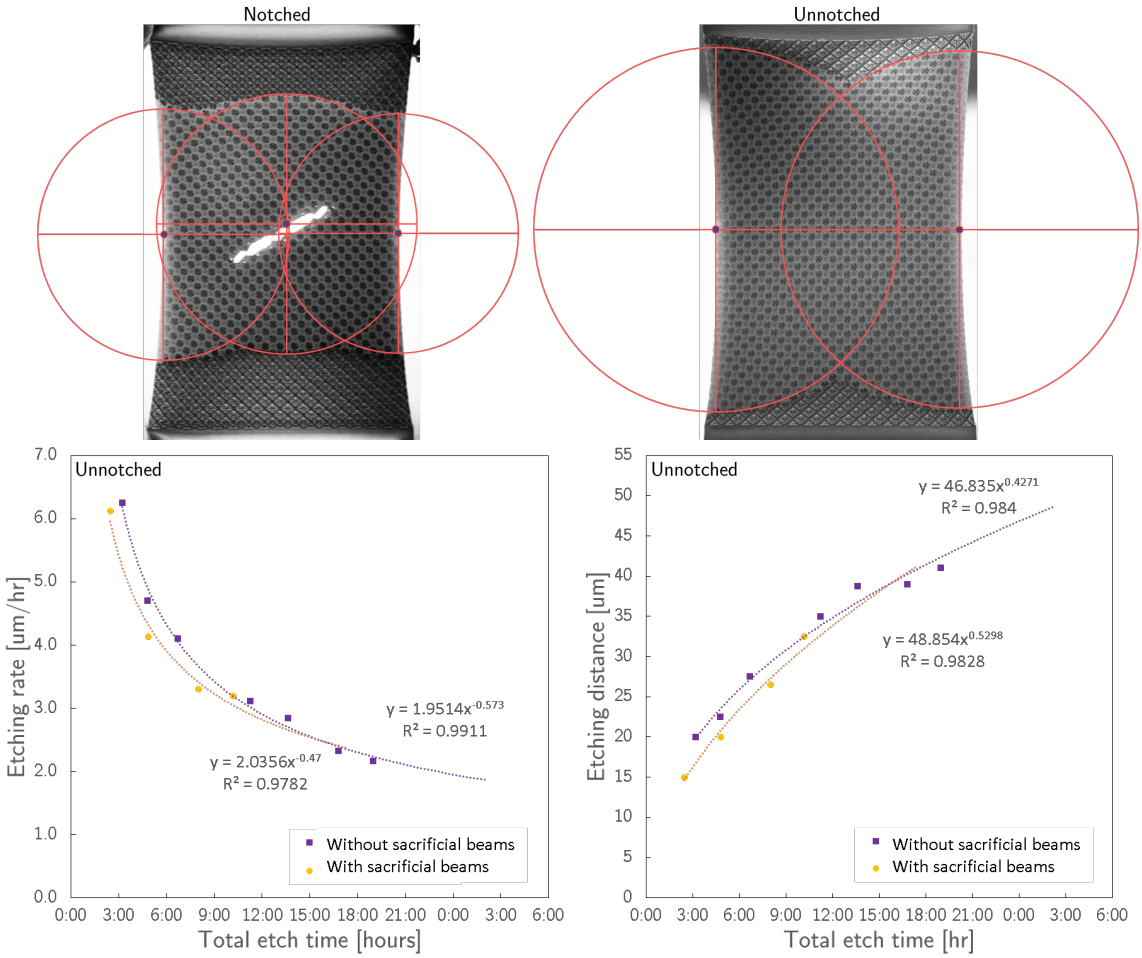

Figure 2.7: Samples were etched in O_2 plasma barrel asher and monitored to determine the etching rate and the total amount of time required to etch away the gauge section only without affecting the integrity of the support structures.

dimensions of the tubes based on SEM images (see Fig. 2.2 and Fig. 2.3). Using these dimensions, the volume of the polymer unit cell contained in the unit cell was calculated using the SolidWorks model. The volume fraction was found by dividing the volume of the material contained in the unit cell by the volume encompassing the unit cell, which is equivalent to the relative density of the structure. A single unit cell was considered in this calculation since the volume of the structure and the bulk both scale by the number of units cells that form the lattice.

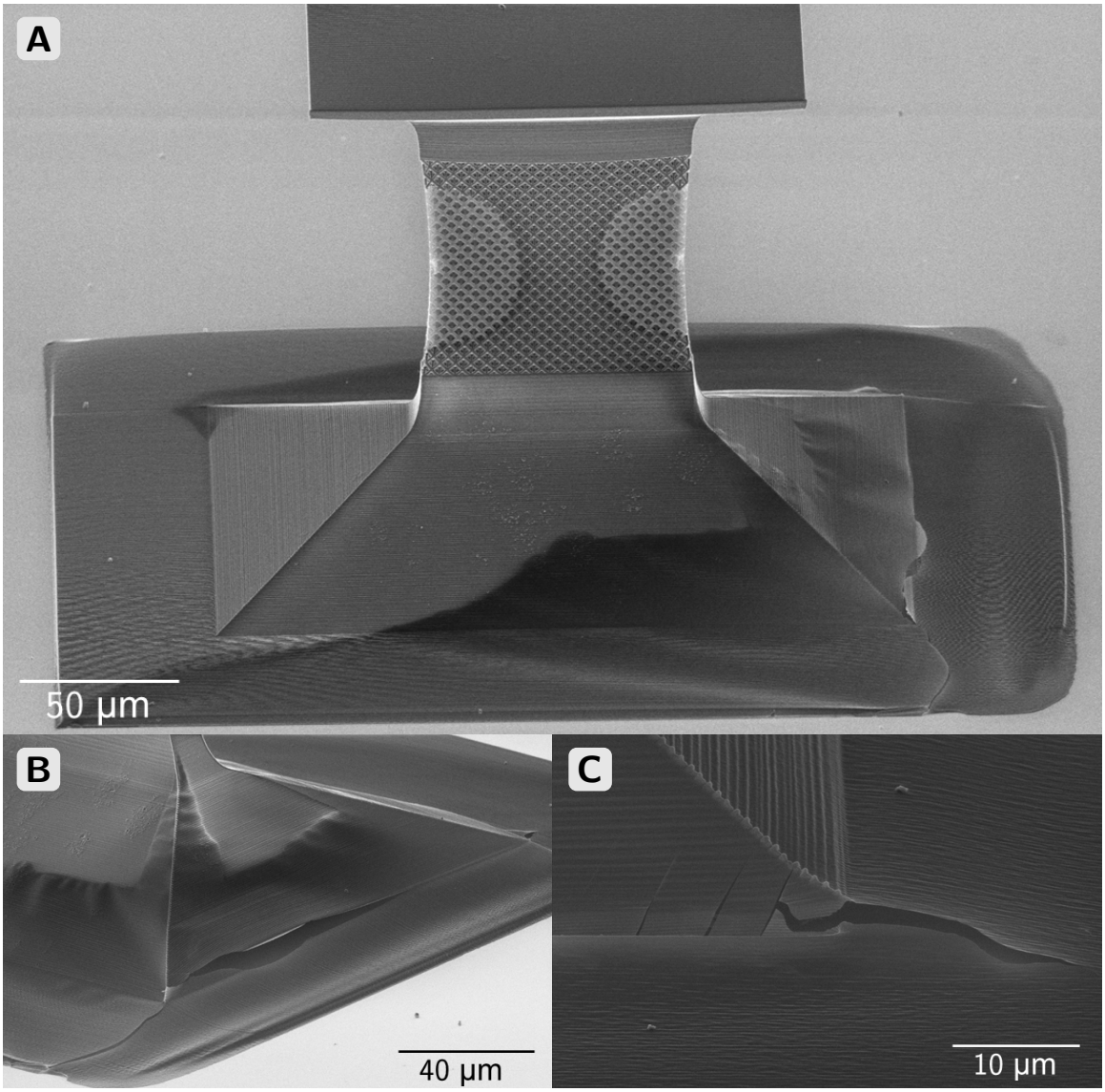

Figure 2.8: Most samples did not survive the O_2 plasma etching due to undesirable etching away from the gauge section. (A) For example, etching will simultaneously start at the gauge section and at the bottom support where defects were found. Since the etching rate is higher for the support compared to the tortuous paths of the gauge section, then the support will be completely hollowed out before the gauge section is ready for the tension experiment. (B-C) Cracks usually formed at the interface between the bottom support and the substrate, which propagated due to the shrinkage of the polymeric core and stress concentrations in the alumina thin film. The final tensile specimens were designed to alleviate stresses on the thin film and prevent the formation of cracks after the resin development and etching processes.

Chapter 3

Experimental Methods

3.1 Introduction

Uniaxial tension experiments were conducted in an in-situ nanomechanical instrument to simultaneously collect load-displacement data and to observe the deformation process and global and local failure. The axial displacement measured by the instrument was corrected to account for the additional compliance of the nanoindenter-sample system by quantifying and subtracting the extension outside the gauge section from the total measured extension and accounting for the contributions of supporting structures and tension grips to the displacement.

3.2 In-situ Nanomechanical Experiments

Tension experiments were conducted in an in-situ nanomechanical instrument (InSEM, Nanomechanics Inc.) to observe global and local failure behavior. Samples were subjected to an applied tensile load by engaging with a custom-made tension grip. The tension grip was machined on the head of a $0.8mm$ stainless steel screw by electrical discharge machining; see Fig. 3.1. *Video S1* and *Video S2* show the in-situ mechanical data and its corresponding real-time video of the deformation of an unnotched and notched specimen.

Once the sample settles and self-align into the wedged tension grip, most of the pre-existing slight misalignment within this experimental setup is rectified; that is, minimal lateral movement is seen in videos and the load-displacement data contains short non-linear regions at the initial stage of loading. All experiments were conducted at a quasi-static strain rate of $10^{-3}s^{-1}$ and were carried out to failure. Fig 3.2 shows a representative raw data depicting constant strain rate loading after the initial settling events.

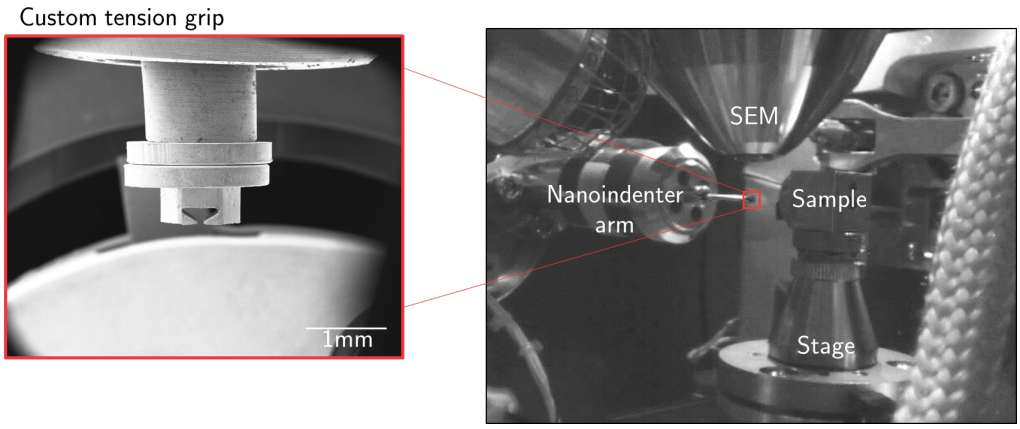

Figure 3.1: Custom tension grip used to test nano-architected tensile samples. The tension grip was machined on the head of a $0.8mm$ stainless steel screw by electrical discharge machining.

3.3 Data Analysis Methods

To correctly measure the uniaxial tensile properties of a material, special techniques must be adopted in order to avoid damaging samples and compromising the area of interest. However, the additional material that must be used to grip, support, or adhere the sample, will lie in the loading path and influence the recorded strain measurements. The contributions from these sources must be accounted for to accurately report the strains of the area of interest. The extension from outside the gauge section must be determined and subtracted from the total measured extension. The total measurement of the stiffness for the nanomechanical experiments can be viewed as the effective stiffness of springs in series, as illustrated in Fig. 3.3A and quantified as

$$\frac{1}{K_{eff}} = \frac{1}{K} + \frac{1}{K_s} \tag{3.1}$$

where K_{eff} is the effective stiffness recorded by the nanomechanical instrument, K is the stiffness of the gauge section, and K_s is the stiffness outside of the gauge section, as shown in Fig. 3.3B. Since compliance is the inverse of stiffness, Eq. 3.1 can be written as

$$C_{eff} = C + C_s \tag{3.2}$$

Additional experiments on samples without the gauge section were performed to determine C_s. Samples were fabricated without the hollow gauge section, as shown in Fig. 3.3C. Two layers of alumina-polymer core-shell composite octet unit cells make up the central section of these samples to resemble the few composite unit cells in samples with complete hollow gauge sections. The average

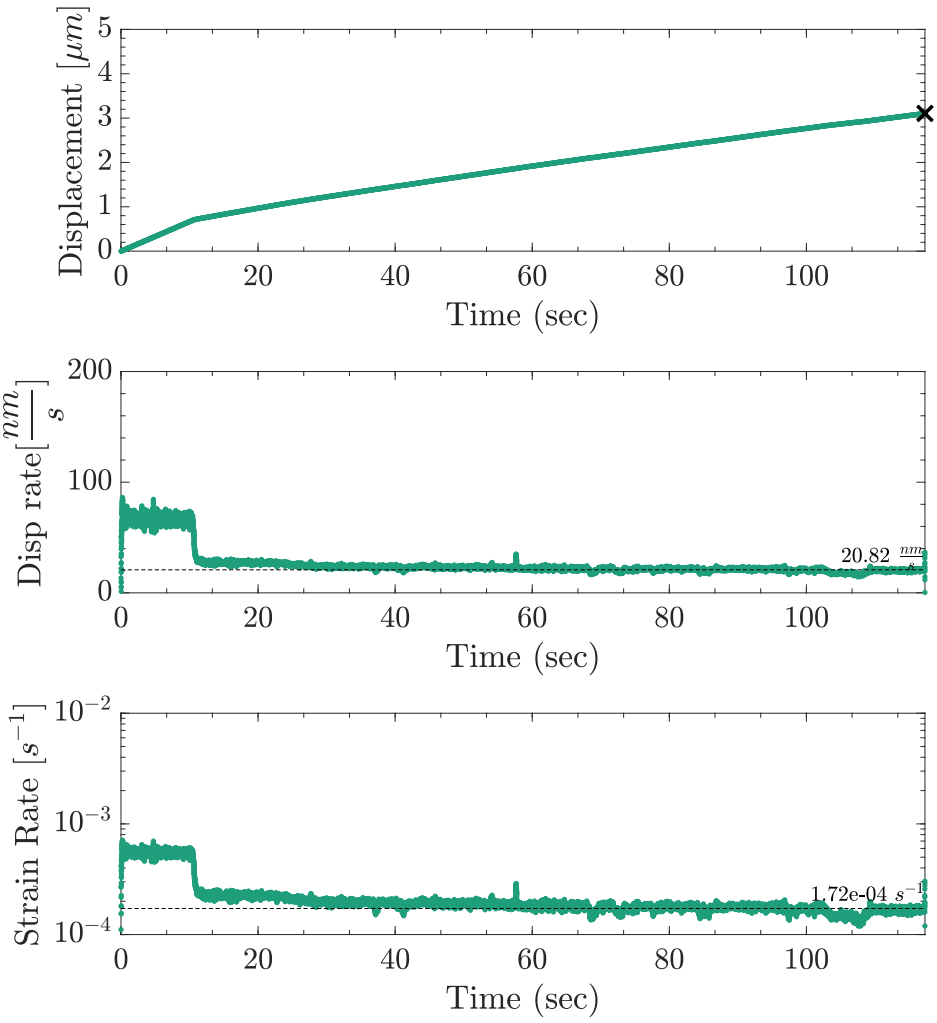

Figure 3.2: Representative displacement data for an unnotched sample and corresponding displacement and strain rates as a function of time. After initial settling events, all samples are loaded under constant strain rate conditions.

compliance of multiple samples was determined and subtracted from the displacement and subsequent strain calculations for each unnotched and notched sample. The corrected displacements were then normalized by the gauge section length to determine engineering strains. The corresponding loads for all samples were converted to stresses, defined as $\sigma = P/A$; P is the measured load and A is the total cross-sectional area perpendicular to the load.

Displacements and strains of the gauge section could also be calculated using the observed length change with the real-time deformation video recorded by the scanning electron microscope. However, since the window frame of the video must account for the entire gauge section ($\sim 120\mu m$ in length)

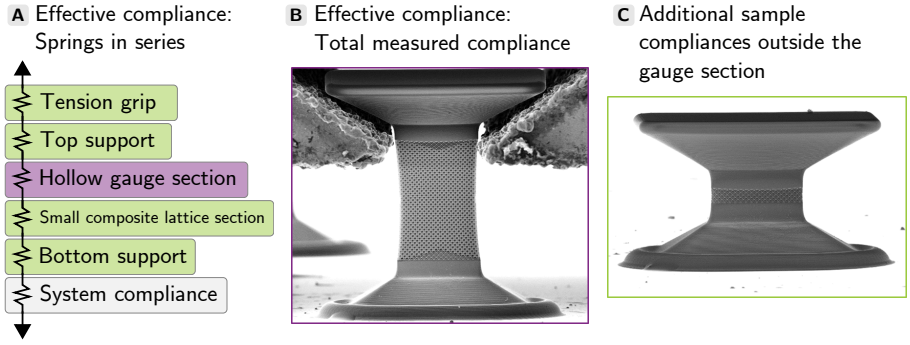

Figure 3.3: Displacement and strain for the hollow gauge section only can be obtained by subtracting the contribution of the additional compliance from the effective compliance recorded by the nanomechanical instrument.

and total strain at failure of $0.01 - 0.03$ ($\sim 1 - 3\mu m$), the maximum length change is confined to less than 5 pixels. This low amplitude of displacements and the characteristic grainy appearance of micrographs (as a result of random fluctuations of electrons in the electron beam) render the video-assisted technique unsuitable for accurate strain measurements. Fig. 3.4 illustrate a comparison between the compliance-corrected data and the video-corrected data. Displacements corrected with the real-time video resulted in stiffer samples by more than a factor of 2 compared the compliance-corrected data, which yielded stiffnesses close to the values reported for similar hollow-tube octet nanolattices tested in compression [30]. The compliance method was employed to accurately measure the displacements and strains of the gauge section, and to systematically account for the additional compliance by the sample geometry and nanomechanical system.

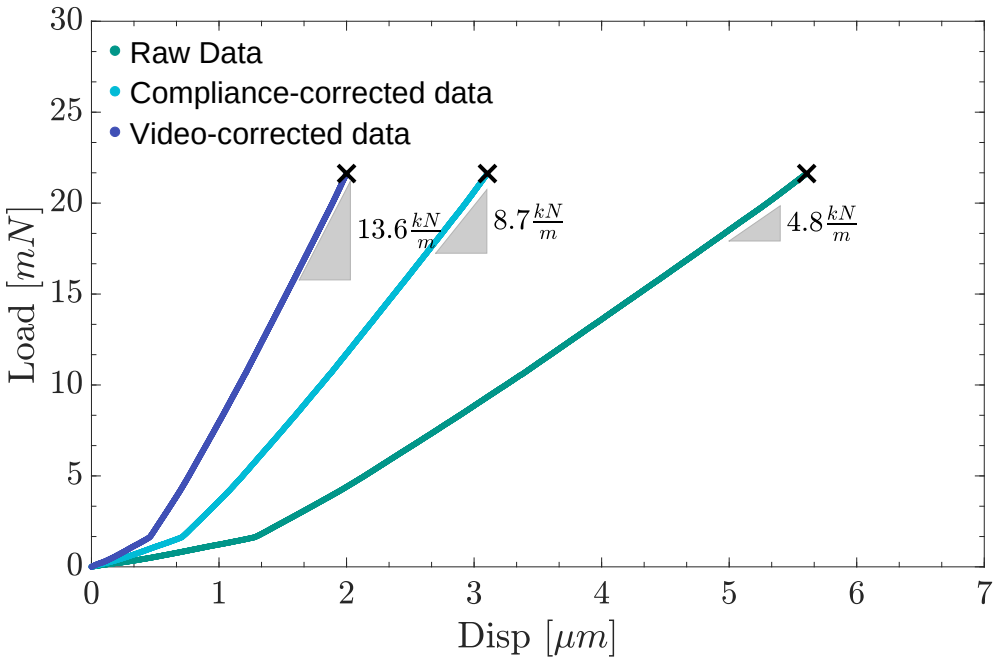

Figure 3.4: Comparison between raw data, compliance-corrected data, and video-assisted corrected data.

Chapter 4

Tensile Response of Nanolattices

The stress-strain data for all unnotched center-notched tensile specimens is shown in Fig. 4.1. For clarity, only one representative curve is colored and all others are grayed out. The data reveals that after the initial self-alignment into the tensile grips (shown by the non-linear behavior within 1% strain of incipient loading), all specimens displayed linear elastic loading up to failure regardless of the presence of a notch (Video S1). The point of tensile failure strength is defined as the maximum tensile stress prior to failure and is denoted by 'x' in Fig. 4.1. The distribution of local nodal strengths leads to scatter in the observed tensile failure strengths. We calculated the Young's modulus from a linear fit of the stress-strain data after 50% of the maximum strain for all samples. We used bootstrap statistical analysis to calculate the mean and standard error of the Young's modulus for each notch orientation, which is shown by the dashed line to the right of the data. We found the Young's modulus of unnotched specimens to be $1.30 \pm 0.04 GPa$ in agreement with experimental studies of similar nanolattices under compression [30].

The elastic behavior of these nanolattices was reaffirmed by performing cyclic tensile experiments. Cyclic experiments consisted of 10 loading segments to $\sim 0.90\%$ of the average load at failure for all unnotched samples, followed by an unloading segment last the original position of the tension grip (Fig. 4.2). The load-displacement data shows stable hysteretic cycling behavior for all cycles. After each consecutive cycle, the sample recovered to the original height on unloading with minimal degradation; all subsequent cycles showed nearly complete recovery to this initial deformed position. The nanomechanical instrument could be the main reason for the hysteresis due to the displacement spring in the transducer, which has a notable effect over high loads and low displacement ranges. The hysteresis in each cycle may also be attributed to friction between the tension grip and the tensile sample, but its contribution is most likely minimal.

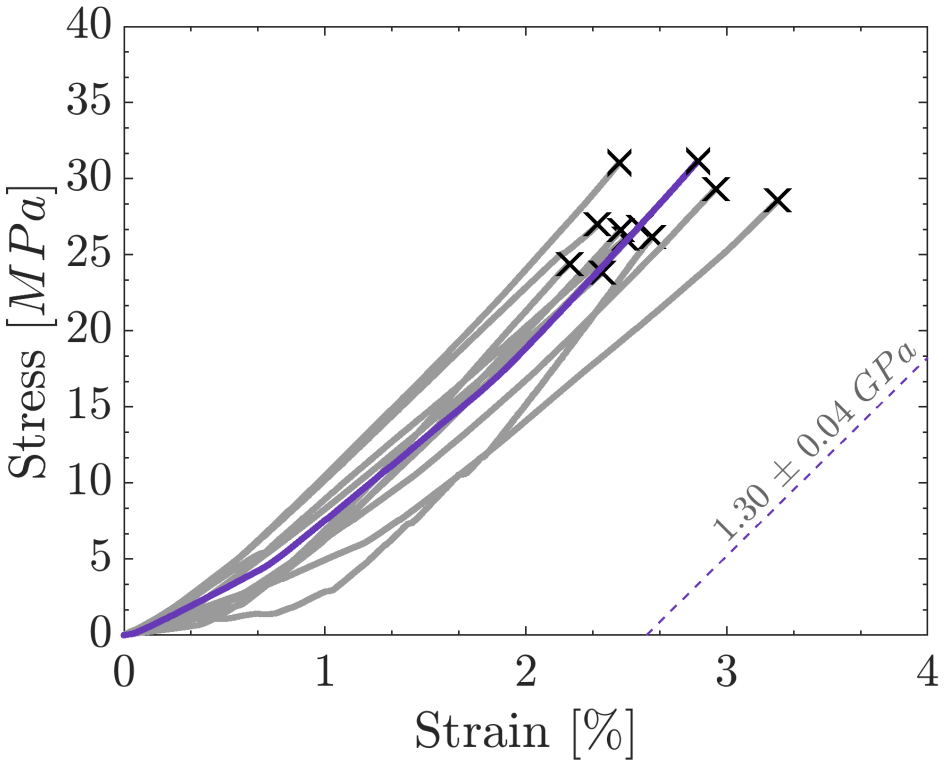

Figure 4.1: Stress-strain response of unnotched samples. The Young's modulus is averaged over all samples is also plotted and shown as a dashed line. For visual simplicity, one representative curve has been highlighted (purple).

4.1 Specific Tensile Strength of Hollow Octet Nanolattices

The experimentally measured tensile strengths of $27.4 \pm 1.4 MPa$ exhibited by the unnotched nanolattices represent the highest tensile strength reported for architected materials to date (Fig. 4.4). At a low relative density of 6.5%, these nanolattices attain a specific tensile strengths of 146 $kPa\ kg^{-1}\ m^3$; outperforming all other existing materials with lattice architectures and bulk materials with low relative densities (Fig. 4.3). The specific tensile strength of 146 $kPa\ kg^{-1}\ m^3$ of hollow alumina nanolattices is a factor of ~ 4 higher than what has been reported for similar nano-architected materials [31, 32], which places them prominently in the untapped territory in the material properties space. The attainment of such high strengths likely stems from activating tube wall fracture as the failure mechanism, i.e. material strength-driven phenomenon, instead of buckling and bending-dominated deformation, a structural response previously seen in hierarchical lattices and composite nanolattices under tensile loads [25, 32]. Buckling in nanolattices is correlated with a significant reduction in the scaling of strength with relative density caused by the nonlinear dependence of buckling on slenderness in low-density samples [1, 58, 59]. The experimental methodology and sample design employed in these nanomechanical experiments allows for a large number of unit cells to

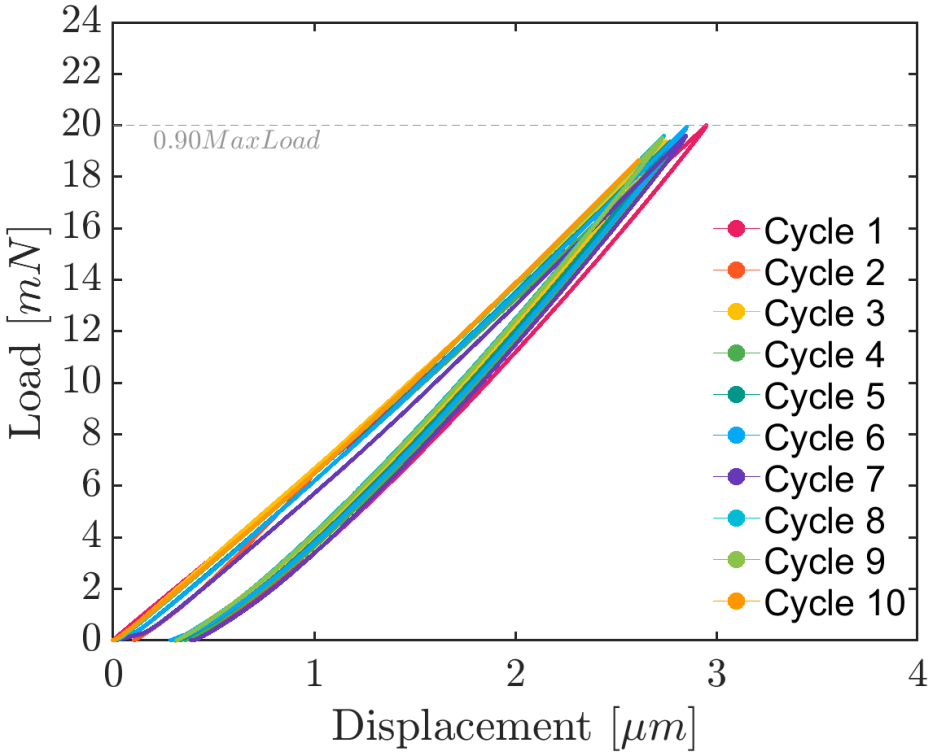

Figure 4.2: Cyclic loading of an unnotched sample. Minimal degradation of elastic properties is seen after 10 loading-unloading cycles.

span the length and width of the gauge section (27 and 17 unit cells, respectively), which enables the measurement of the effective strength of the architected gauge section rather than the strength of a structure or the strength of its constituent beams and nodes.

4.2 Weibull Statistical Analysis

The most common way to describe the strength distribution of brittle materials is the Weibull distribution [60–63]. This statistical analysis is based on the weakest-link argument, which describes failure as a catastrophic event initiated at the any flaw within a given volume. Also, it assumes a homogeneous distribution of flaws throughout the volume. Assuming a constant volume across all specmines, this empirical two-parameter relation takes the form of

$$P = \exp\left[-\left(\frac{\sigma_f}{\sigma_o}\right)^m\right] \tag{4.1}$$

$$P = 1 - P_f \tag{4.2}$$

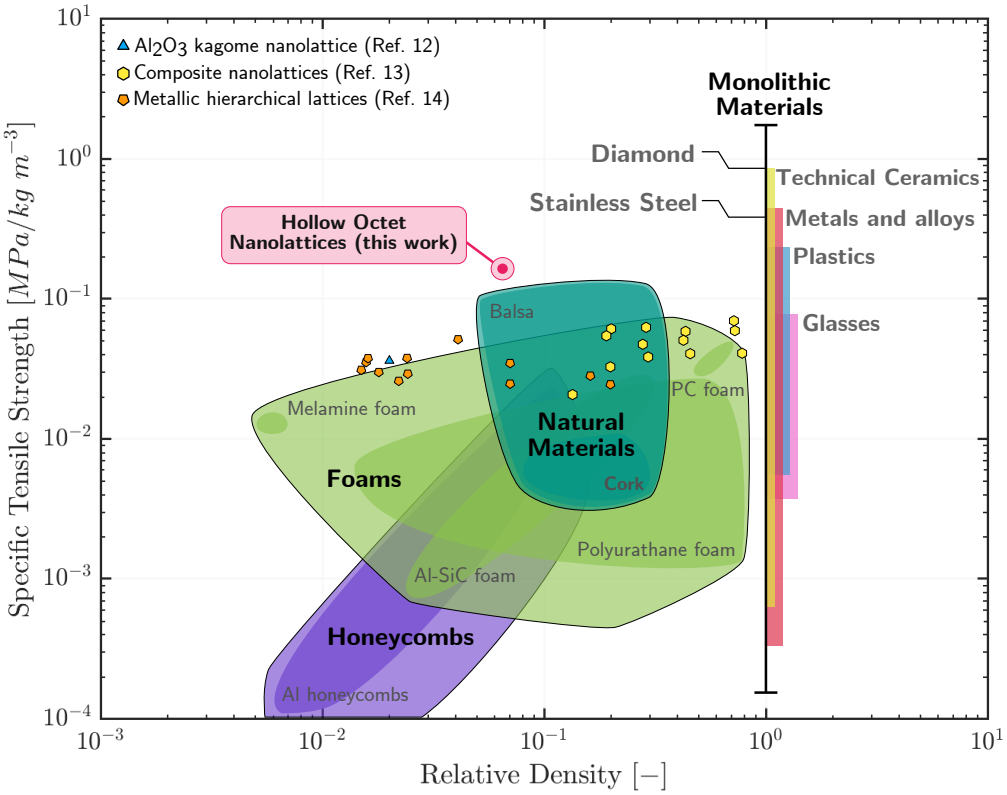

Figure 4.3: Specific tensile strength versus relative density. Architected lattices known to be tested in tension and material groups have also been plotted for comparison.

where P is the probability of survival of the whole specimen, P_f is the probability of failure for the whole specimen, σ_f is the stress at failure, and the two distribution parameters are σ_o, the stress level at which the survival probability is equal to $1/e$, and m, the Weibull modulus. These parameters can be found by solving for $\frac{1}{P}$ and taking natural logarithms twice to arrive at

$$\ln\ln\frac{1}{P} = m\ln\frac{\sigma_f}{\sigma_o} \tag{4.3}$$

$$= m\left(\ln\sigma_f - \ln\sigma_o\right) \tag{4.4}$$

The Weibull parameters are then determined by using a linear fit; whose slope is the Weibull modulus m and the intercept on the ordinate of the diagram is related to σ_o when $\ln\ln\frac{1}{P} = 0$. Then the survival probabilities for a given stress level is calculated by ranking the data points of strength values in ascending order and assigning a number beginning with 1 and ending with N. The survival probability of the i^{th} specimen can be determined using a mean rank [64, 65], that is

$$P_i = 1 - \frac{i - 1/2}{N} \tag{4.5}$$

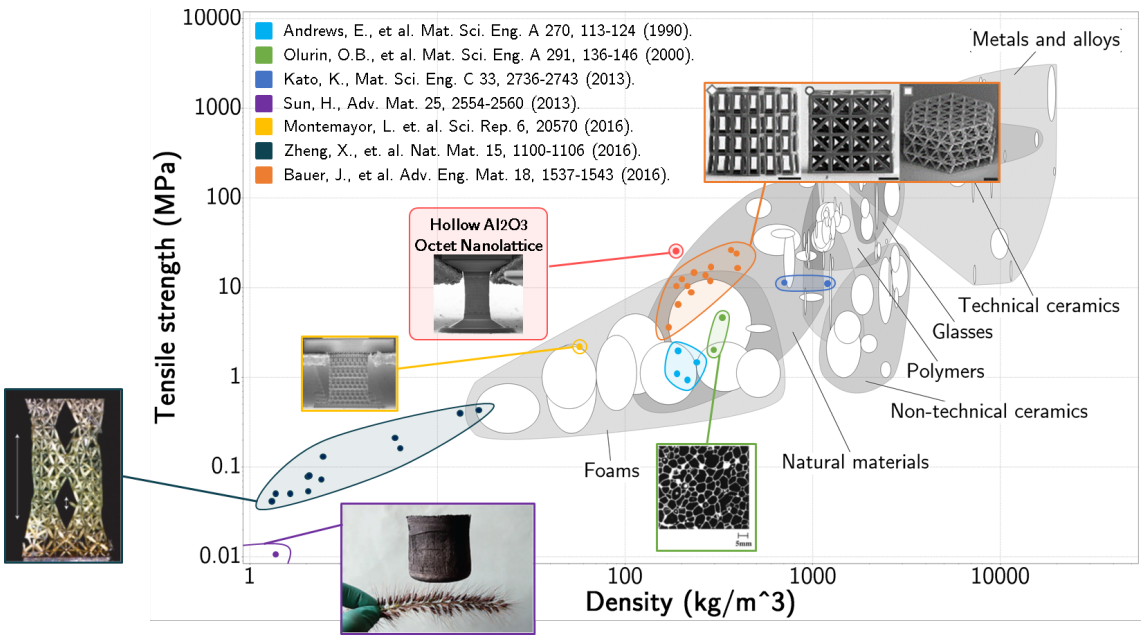

Figure 4.4: Tensile strength of material groups and architected materials known to be tested in tension.

The Weibull distribution diagram for unnotched specimens in this study is shown in Fig. 4.5. The Weibull modulus is found to be 13.21; similar values were calculated using several rank methods. This value falls within the typical range of Weibulll modulus for engineering ceramics ($m = 10 \sim 20$), including thin film alumina [61, 66, 67].

The high Weibull modulus indicate a well behaved flaw population for these tensile specimens. For an nano-architected material, the flaw population can be dictated by defects in the constituent material and geometric defects in the lattice architecture. The complex interplay between the defects across several length scales, including the thickness of the thin film, limits the material defects to less than the $50nm$. Geometric defects are usually introduced during the writing process in the form of wavy or rough structural elements, common to additive manufacturing processes, and by the shrinkage of the polymeric scaffold during the development phase. The high modulus from such a moderate set of samples suggests that a larger set can yield an even higher Weibull modulus, and therefore, a greater reliability of nanolattices to accompany the high specific tensile modulus. Nevertheless, the Weibull statistical distribution seem to be reasonable representations of the measured tensile strength of brittle nanolattices.

It is worth noting that this statistical analysis is typically used to fit tens to hundreds of data points and then extrapolated to probabilities outside the range of stresses in the experiment. The data sets for our nanomechanical experiments are rather small compared to the usual sets of macroscopic tensile and fracture experiments. Needless to say, it is understood that incrementing the total

number of data points in this study by one means devoting more than 84.5 hours (as illustrated in table 2.1); while typical macroscopic specimens can often be readily mass-produced by the ten or hundred.

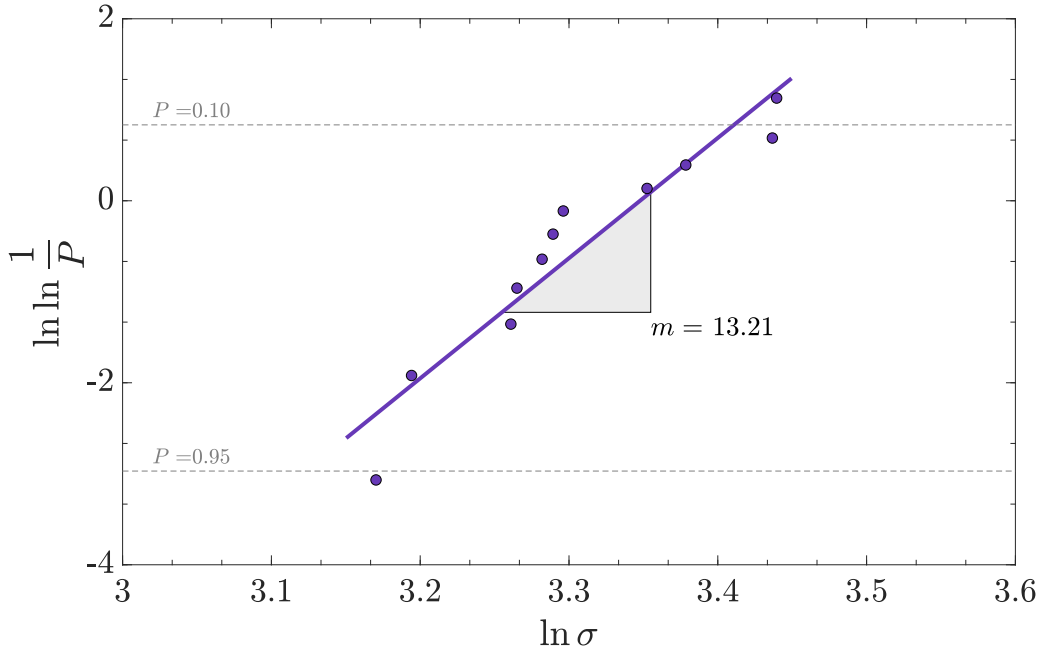

Figure 4.5: Weibull probability diagram for unnotched specimens. The Weibull modulus is denoted by the slope of the linear fit. Guidelines for a survival probability (the fraction of samples that would survive a given stress level) of 95% and 10% are also included for visual assistance.

4.3 Failure Surface Morphology

A fractographic evaluation of unnotched samples revealed the local trajectory of crack propagation of hollow octet nanolattices under tensile loads. Global failure surface is confined to planes of nodes perpendicular to the uniaxial applied load as cracks traverse from node to node across hollow tubes, as depicted in Fig. 4.6. Samples with uneven failure surfaces corresponded to low tensile strengths (Fig. 4.7). This high occurrence of ragged failure surfaces can be attributed to the inevitable misalignment of the tension grip with the sample central axis. The uneven applied force with a lateral contribution, which results in an unequal stress distribution at the gauge section. Since the strains at failure are $\sim 2.5\%$ (equivalent to $\sim 3\mu m$), a slight misalignment of the tension grip can result in a largely asymmetrical distribution of stress across the width of the samples and premature initiation of failure closer to the top boundary of the gauge section. These observations facilitated proper evaluation of data for experimental analysis.

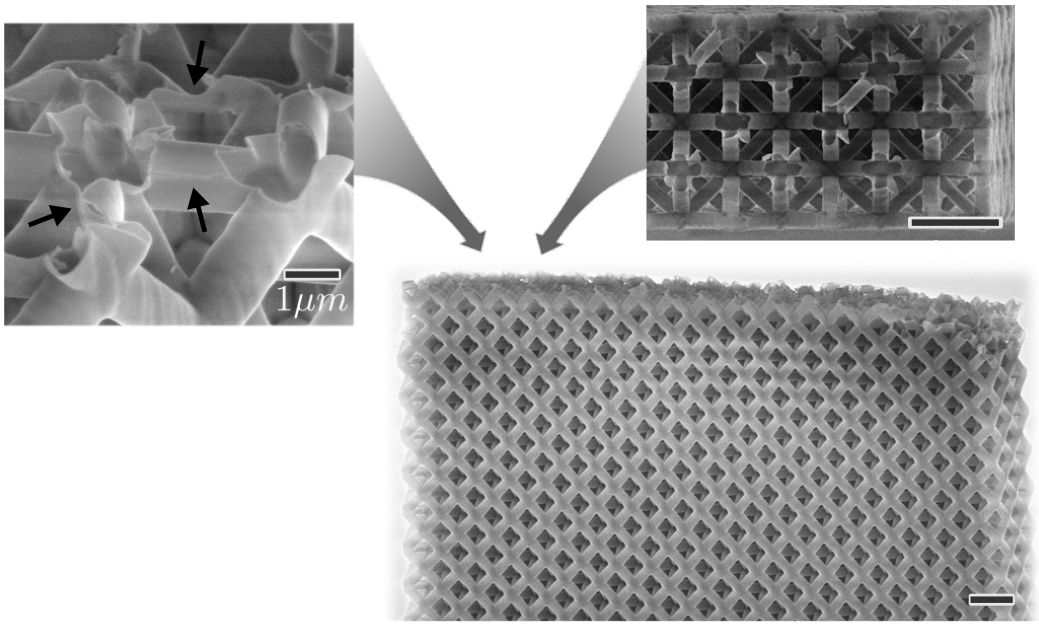

Figure 4.6: Failure surface morphology of center-notched tensile samples. SEM images show crack propagation from crevices at nodal junctions; arrows indicate path trajectories across tube wall. Scale bar denotes $5\mu m$, unless stated otherwise.

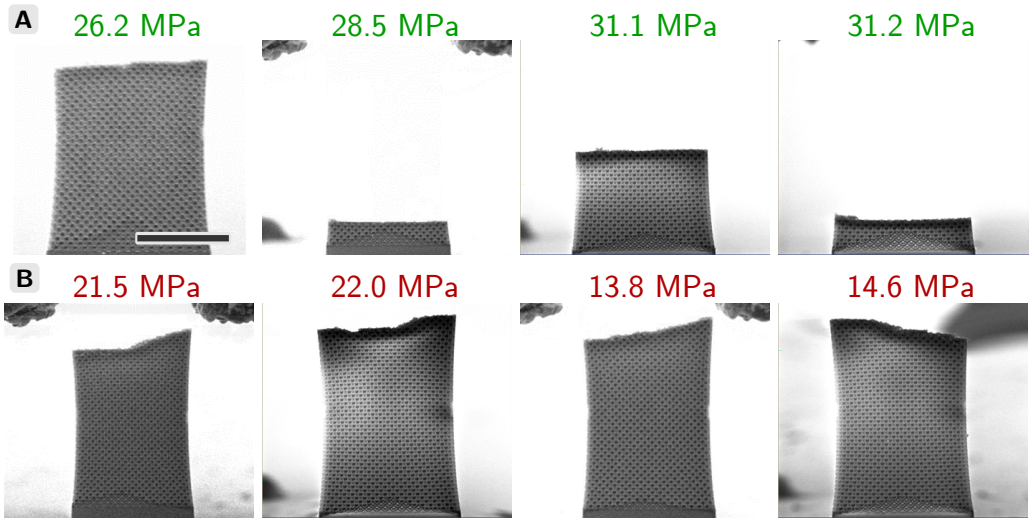

Figure 4.7: Failure surface morphology of unnotched tensile samples. SEM images of failure surface morphology and corresponding failure load. (Row A) A low percentage of fabricated samples exhibited high tensile strengths with failure localized in one plane of nodes perpendicular to the applied load. These samples make up the set of unnotched specimens used in this work. (Row B) The majority of unnotched tensile samples failed at lower strengths coupled with uneven failure surfaces and discarded from the analysis section of this work. Scale bar denotes $50\mu m$.

4.4 Failure Mechanisms

The mechanism of failure in hollow nanolattices is likely associated with crack initiation at the weakest nodal junctions stochastically within the gauge section of the unnotched nanolattices and then instantly propagating through the nodes along a "nanolattice plane" orthogonal to the loading direction. The trajectory of crack propagation depends on the stress distribution at the nodal junctions. The complex local stresses within hollow nodes lead to an uneven distribution of stress within the unit cell that induces stress concentrations at crevices, i.e. wall tube intersections, which act as elastic hinges and dominate the deformation of the unit cell. Cracks initiate at these localized zones and extend along hollow tubes into adjacent zones of high tensile stress, as shown in Fig. 4.6. Meza, et al. described the compressive deformation of similar alumina nanolattices to occur via three main failure mechanisms: (1) fracture of the tube walls, (2) Euler buckling, or (3) shell buckling of individual tubes [1]. In an octet architecture, the hollow tubes that are parallel to the x-axis in Fig. 2.3B could buckle in response to global tension being applied to the specimen. The dominance of a failure mode is dictated by the tube geometry, which is described by two characteristic length ratios: wall thickness-to-radius ratio t/a and tube radius-to-length a/L. For the tensile specimens in this thesis, t/a is 0.1029 and a/L is 0.1469 (see Fig. 2.2E for dimensions). These ratios fall below the critical ratios for Euler or shell buckling, which indicates that the failure of nanolattices in this work occurs solely by tube-wall fracture. In-situ nanomechanical experiments suggest the dominant failure mechanism to be via tube wall fracture followed by crack branching; i.e., cracks branch and propagate in multiple directions from node to node across hollow tubes, as seen in Fig. 4.6. Damage away from the initial failure location, e.g. in the form of cracks at nodal junctions, could occur but such dynamic events are not able to be captured by the frame rate of the nanomechanical instrument.

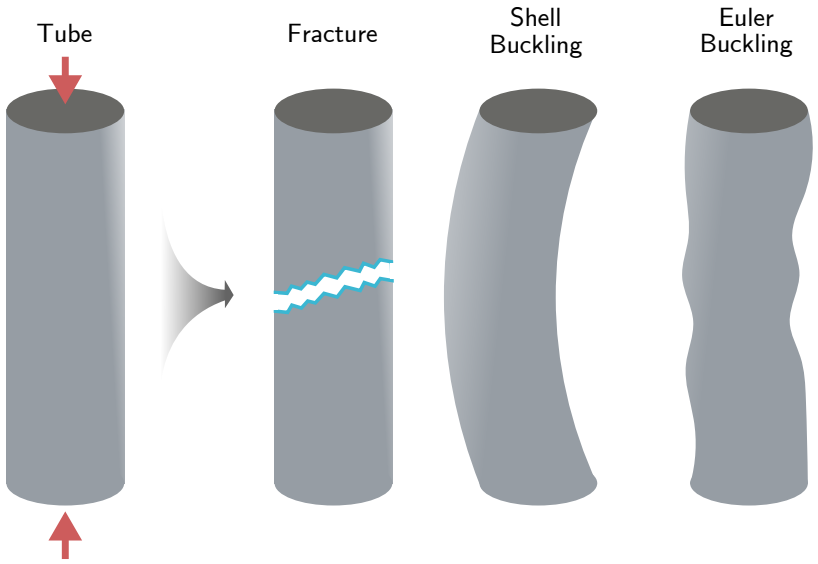

Figure 4.8: Failure mechanisms of hollow-tube nanolattices can be simplified to the energetic competition between fracture of the tube walls and buckling instabilities, as described in ref. [1].

Chapter 5

Tensile Response of Flaw-Containing Nanolattices

5.1 Introduction

Understanding how a material behaves in the presence of flaws is integral to determining its fracture response. Naturally occurring defects like pores, voids, and notches within a solid are generally subjected to a complex stress state determined by their shape and orientation relative to the applied loads. In trying to design fracture-safe materials, a defect's geometry and orientation must be considered to fully characterize the possible mixed-mode states and to quantify a material's resistance to fracture initiation. Typically, such fracture experiments are performed on samples with pre-defined flaws. Center-notched tension specimens are commonly used for characterizing tensile properties and fracture behavior of thin films, plates, and sheet materials [68,69]; this geometry allows notches to be oriented along directions that closely resemble the mixed-mode loading of naturally occurring defects. The experimental results from notched tensile specimens will be presented in this chapter and analyzed in the following chapter.

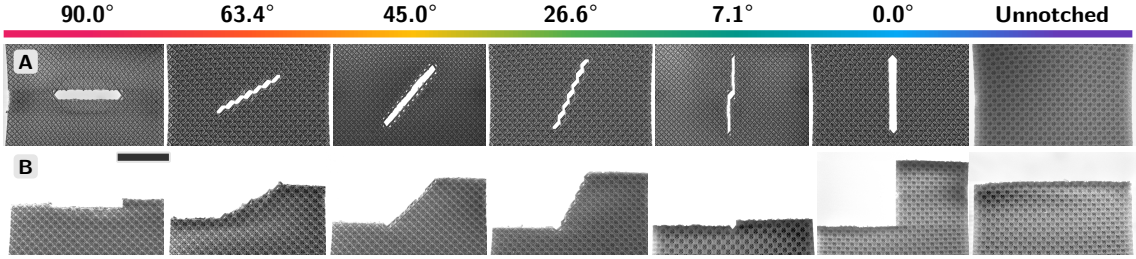

Figure 5.1: Failure surface morphology for notched and unnotched specimens (scale bar: $25\mu m$).

5.2 Path of Crack Propagation

Post-failure SEM images (Fig. 5.1) reveal that the notched hollow-tube octet nanolattices always failed at the notch roots, and that brittle failure occurred along a plane of nodes orthogonal to the loading direction, regardless of the notch orientation. The unnotched nanolattices also failed along a single nodal plane within the gauge section. Fig. 5.2 shows zoomed-in SEM images of the fracture surface of a notched sample and suggests that cracks initiate at a node within the notch root and propagates outwards towards the boundary of the specimens.

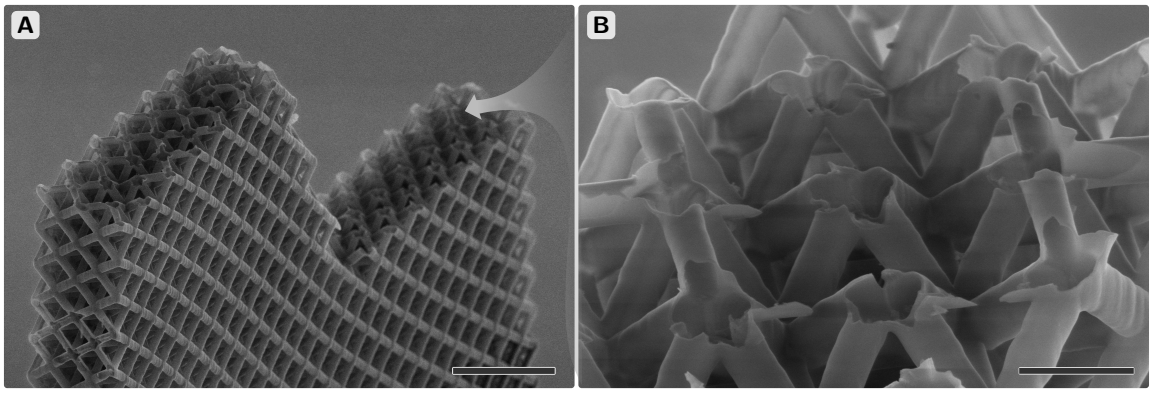

Figure 5.2: Global and local failure surface morphology. Scanning electron micrographs of (A) notched sample after failure (scale bar: $10\mu m$) and (B) local crack propagation trajectory on nodal junctions and through hollow tubes (scale bar: $2\mu m$).

5.3 Onset of Failure

Fig. 5.1 contains SEM images of all specimens before and after failure as a progression of notch orientations and the the corresponding stress-strain data is plotted in Fig. 5.3. The data reveals that after the initial self-alignment into the tensile grips, all specimens displayed linear elastic loading up to failure regardless of the presence of a notch (Movie S1-S2). For each plot, the point of tensile failure strength is defined as the maximum tensile stress prior to failure and is denoted by 'x', and plotted separately in Fig 5.4. For clarity, the failure strengths for all samples are also plotted and a single representative stress-strain curve for each notch orientation. The distribution of local nodal strengths leads to scatter in the observed tensile failure strengths. Young's modulus was calculated from a linear fit of the stress-strain data after 50% of the maximum strain for all samples. We used bootstrap statistical analysis to calculate the mean and standard error of the Young's modulus for each notch orientation, which is shown by the dashed line to the right of the data. We found the Young's modulus of the unnotched specimens to be $1.30 \pm 0.06GPa$, in agreement with experimental studies of similar nanolattices under compression [30], and that of the notched specimens to decrease from $1.76GPa$ to $0.9GPa$ as the notch orientation increased from 0 (parallel)

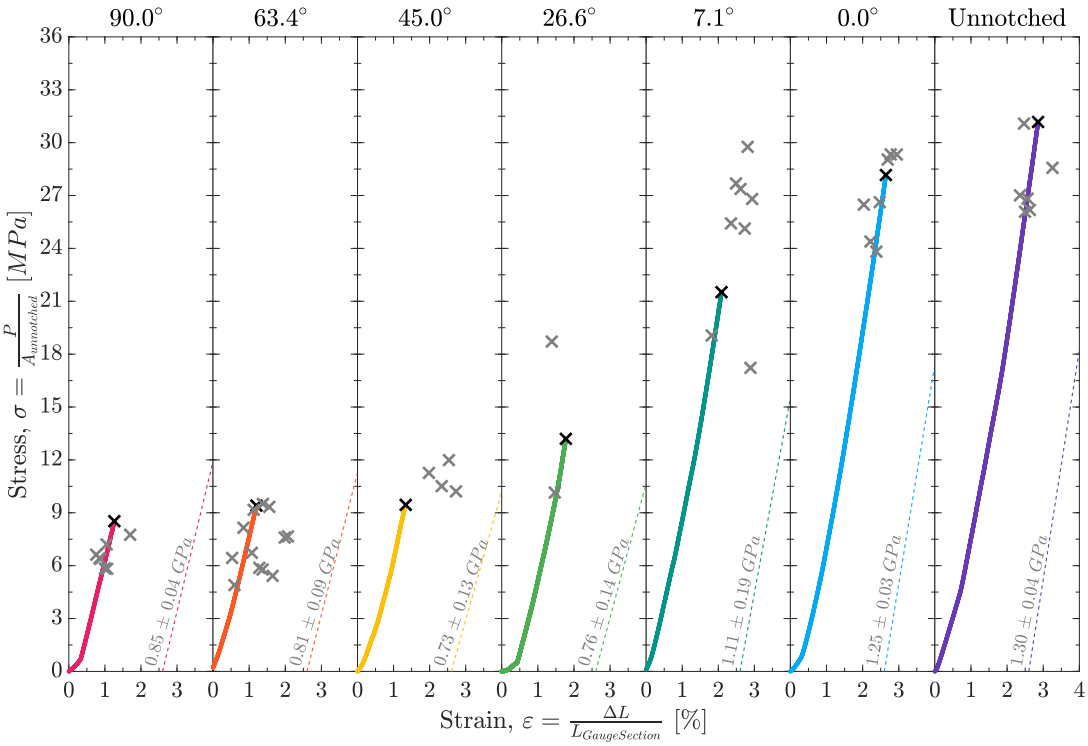

Figure 5.3: Representative stress-strain data for notched and unnotched specimens. All samples show linear-elastic behavior up to catastrophic failure. The mean Young's moduli (dotted line) for each case is also plotted. The point at failure is denoted with an 'x' for all samples.

to 90 degrees (orthogonal).

5.4 Weibull Statistical Analysis

Similarly to the statistical analysis from the previous chapter, the strength distribution of notched specimens can be described by a Weibull distribution. Fig. 5.5 shows the Weibull diagram for notched and unnotched cases. Fig. 5.6 shows the probability density function for all specimens and the Weibull modulus as a function of notch orientation. For comparison the results for the unnotched case has also been included. The distribution of tensile strength is consistent across all notched samples with a mean modulus of ~ 10, expect for the data set for 63.4°-notched specimens, which shows a bimodal population. As seen in Fig. 5.6A, the distribution of stresses indidcate a well-behaved flaw population for notched tensile specimens.

The scatter in stresses for the notched cases is similar to that observed in macroscopic tensile and fracture experiments for engineering ceramics [61–63, 70]; and, also similar to the unnotched case, as expected since the thin film deposition technique and fabrication process were the same. These statistical analysis suggest that the fabrication process is not affecting the measurements.

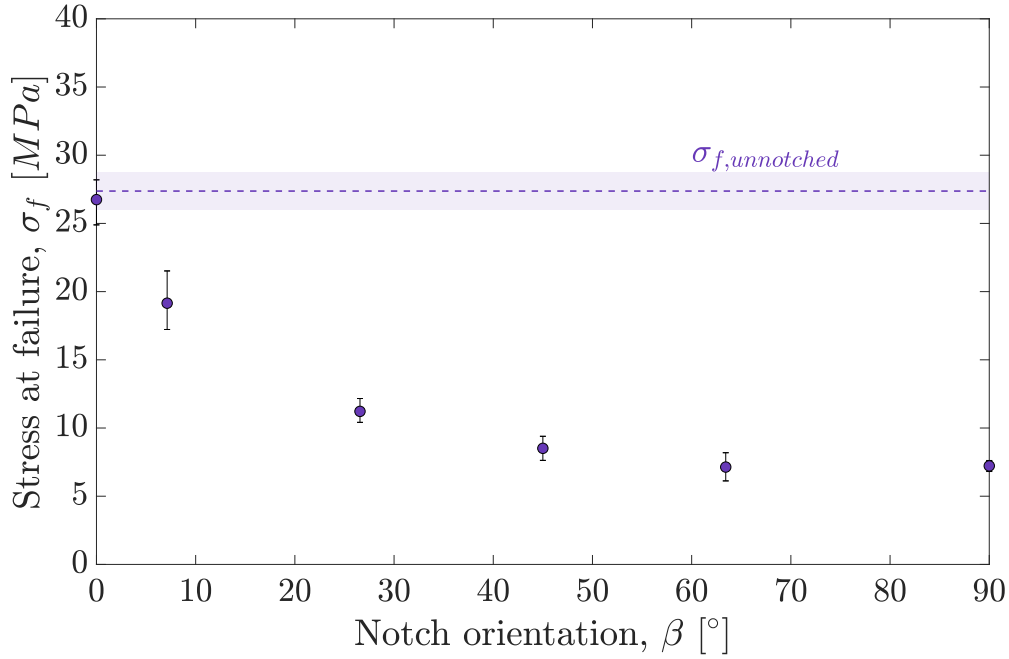

Figure 5.4: Stress at failure for all notched samples as a function of notch orientation. The failure strength for the unnotched samples is also plotted as a band corresponding to a 95% confidence interval centered at the mean strength of all unnotched samples.

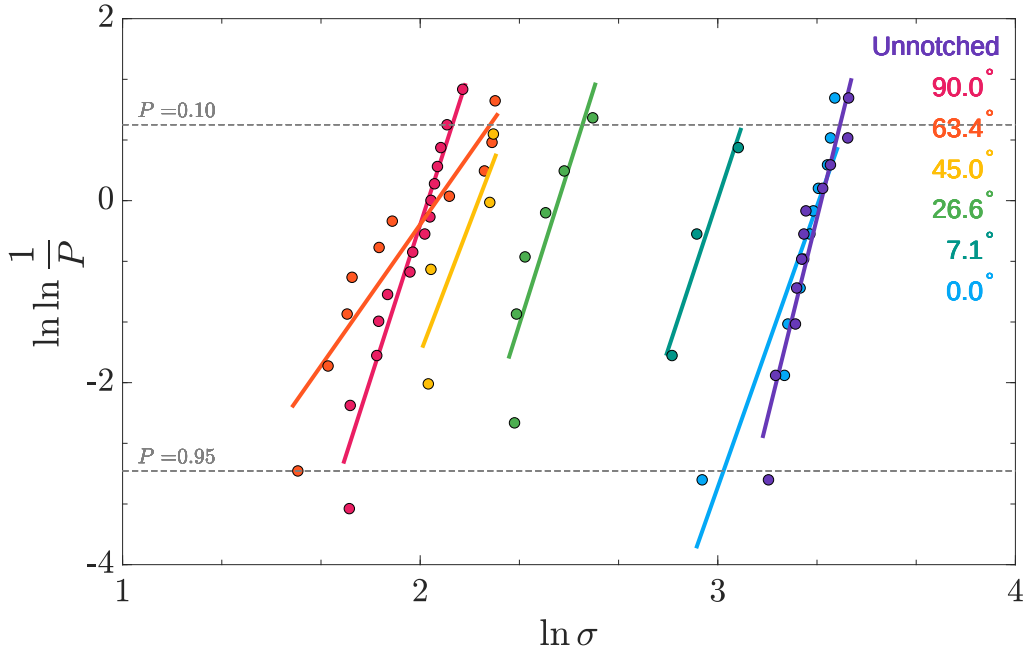

Figure 5.5: Weibull probability diagram for unnotched and notched specimens. The Weibull modulus (denoted by the slope of each linear fit) is consistent for all notched cases and similar to the unnotched case. Guidelines for a survival probability of 95% and 10% are also included.

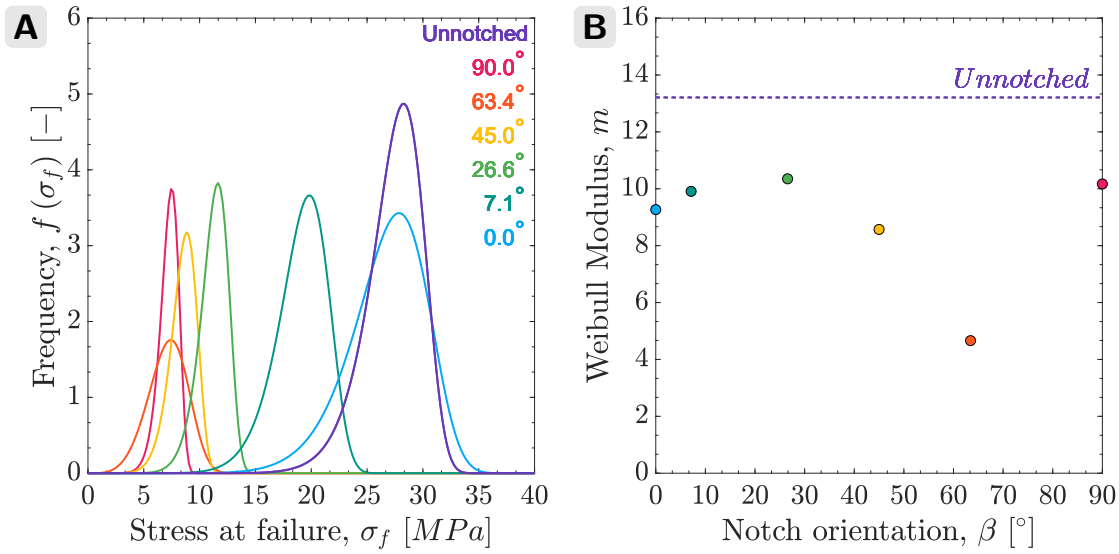

Figure 5.6: Weibull distribution for unnotched and notched tensile specimens. (A) The probability density function for all unnotched and notched cases, and (B) the corresponding Weibull modulus, which is the shape factor of the distribution; that is, as m decreases, the distribution widens.

Chapter 6

Continuum Approach to Center-Notched Tension Specimens

6.1 Motivation

Within continuum mechanics theories, crack propagation can be predicted by defining the critical conditions for crack initiation and incipient crack deflection. A prevalent continuum-based theory, linear elastic fracture mechanics (LEFM), is commonly used to describe fracture of brittle materials and inherently assumes that the microscopic failure events at the crack tip are substantially smaller than the relevant global dimensions of the continuum solid. For most monolithic materials, the size of the plastic zone, i.e. the region where the material has undergone inelastic deformation ahead of the crack tip, can be estimated to be $r_p \propto K_{Ic}^2/\sigma_y^2$, where K_{Ic} is the fracture toughness and σ_y is the yield strength of the material [68, 71]. In brittle or quasi-brittle materials, the dimensions of the plastic zone at the crack tip are comparable to the fracture process zone where all the energy absorption processes occur, on the order of less than 1 μm for engineering ceramics, and is usually deemed negligible with respect to the characteristic lengths of macroscopic specimens. Under these small-scale yielding conditions, LEFM is useful in characterizing the initiation of fracture in brittle materials [68,71]. For LEFM failure criteria to uniquely define stress conditions at the onset of failure, the failure events have to be localized in small areas with radius r_c compared to the characteristic flaw length ($2a$). For these continuum-based criteria to be applicable to architected materials, the flaw itself and the characteristic lattice length (l) must be smaller than the global lattice dimensions (W), i.e. $r_c << l, a << W$. [43]; see Fig. 2.3B,E for corresponding labels.

6.2 Linear Elastic Fracture Mechanics

LEFMs failure criteria that estimates critical conditions at failure are commonly based either on the energy approach, which measures the material's resistance to crack growth and is usually

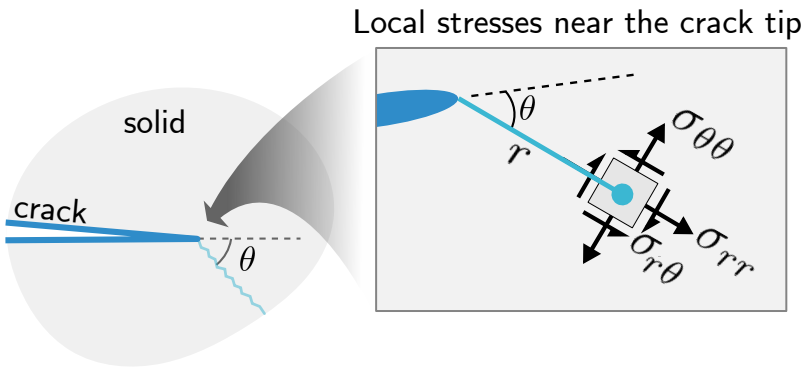

Figure 6.1: Evaluation of local stresses near the crack tip.

parametrized by the energy dissipated during fracture per crack extension, G, or on a critical stress state approach that parametrizes the stress field near the crack tip with a stress intensity factor, K. These two approaches are derived from different physical interpretations are fully equivalent within linear elasticity, where G can be expressed in terms of K as $G = K^2/E'$; where E' is the Young's modulus E under plane stress or $E/(1-\nu^2)$ under plane strain conditions. Stress-based failure criteria that predict crack initiation and the direction of crack propagation have been extensively discussed in literature [71]. Within the scope of LEFM and assuming in-plane mixed-mode loading with dominant mode I and mode II failure, a failure criteria can be expressed as $f(K_I, K_{II}) = 0$, where K_I and K_{II} are the stress intensity factors for mode I and mode II, respectively. Fracture is described by the relative contribution of each mode, which dictates the onset of crack propagation at an inclination to the tangent of the crack axis.

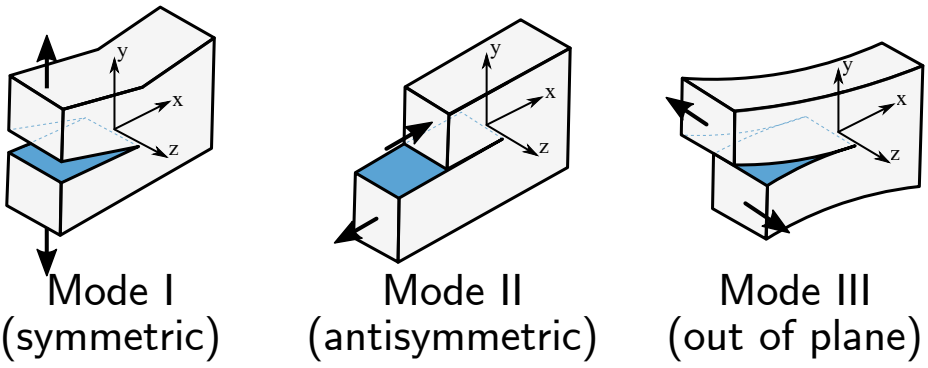

Figure 6.2: Modes of fracture. There exists three types of crack opening: Mode-I denotes symmetric crack opening, Mode-II is characterized by an antisymmetric separation of the crack surfaces, and Mode III describes the separation due to relative displacements in the direction tangent to the crack front. In this work, we consider in-plane mixed-mode loading where mode-I and mode-II are superimposed while mode-III is not present.

Classical fracture mechanics concepts have been used to predict the onset of failure and crack deflection of brittle materials [68, 69, 71, 72]. For a homogeneous, isotropic, and linear-elastic brittle material, the in-plane stresses around the tip of a crack can be described in terms of the stress

intensity factors (K_I and K_{II}). The local stresses can be written in polar coordinates as,

$$\sigma_{rr} = \frac{1}{\sqrt{2\pi r}} \cos\frac{\theta}{2}\left[K_I\left(1+\sin^2\frac{\theta}{2}\right) + K_{II}\left(\frac{3}{2}\sin\theta - 2\tan\frac{\theta}{2}\right)\right] + T\cos^2\theta + O(r^{1/2}) \tag{6.1}$$

$$\sigma_{\theta\theta} = \frac{1}{\sqrt{2\pi r}} \cos\frac{\theta}{2}\left[K_I\cos^2\frac{\theta}{2} - \frac{3}{2}K_{II}\sin\theta\right] + T\sin^2\theta + O(r^{1/2}) \tag{6.2}$$

$$\tau_{r\theta} = \frac{1}{2\sqrt{2\pi r}} \cos\frac{\theta}{2}\left[K_I\sin\theta + K_{II}(3\cos\theta - 1)\right] - T\cos\theta\sin\theta + O(r^{1/2}) \tag{6.3}$$

For a plate with a central crack of length $2a$ inclined at an angle β with respect to the direction of loading and subjected to a uniaxial far-field tensile stress σ (Fig. 6.1), the stress intensity factors are,

$$K_I = \sigma\sqrt{\pi a}\sin^2\beta \tag{6.4a}$$

$$K_{II} = \sigma\sqrt{\pi a}\cos\beta\sin\beta \tag{6.4b}$$

$$T = \sigma\sqrt{\pi a}\cos 2\beta \tag{6.4c}$$

$$\tag{6.4d}$$

$$K_{eff} = \sqrt{K_I^2 + K_{II}^2} \tag{6.4e}$$

For brittle and quasi-brittle materials, a frequently used fracture criterion is based on the assumptions that the crack propagates in the radial direction, θ_0, perpendicular to the maximum circumferential stress, $\sigma_{\theta\theta}$, and that crack propagation initiates when the near field stress $\sigma_{\theta\theta}(\theta_0)$ at a distance r_c in front of the crack tip reaches the same critical value as in pure mode I, described by K_{Ic} [73]. These two conditions can be summarized as followed:

1. The crack propagates in radial direction θ_0 perpendicular to the maximum circumferential stress $\sigma_\theta|_{max}$ (directional condition).

2. Crack propagation initiates when the near field stress $\sigma_\theta(\theta_0)$ at a distance r_c in front of the crack tip reaches the same critical value as in pure mode I (failure condition).

Therefore, the following failure and directional conditions define the onset of fracture,

$$\left.\frac{\partial\sigma_{\theta\theta}}{\partial\theta}\right|_{\theta_0} = 0 \tag{6.5}$$

$$\sigma_{\theta\theta}(\theta_0) = \frac{K_{Ic}}{\sqrt{2\pi r_c}} \tag{6.6}$$

This classical formulation is interpreted as a bipartite criterion, which contains both the critical condition for the onset of failure and a directional condition for the initial crack propagation

trajectory. Using Eq. 6.2 and Eq. 6.5, we obtain θ_0 (at a distance r_c from the crack tip),

$$\left.\frac{\partial \sigma_{\theta\theta}}{\partial \theta}\right|_{\theta_0} = \left[K_I \sin\theta_0 + K_{II}\left(3\cos\theta - 1\right)\right] - \frac{16}{3} T\sqrt{2\pi r_c}\sin\frac{\theta_0}{2}\cos\theta_0 = 0 \tag{6.7}$$

The direction of fracture initiation found from Eq. 6.7, can be used in conjunction with Eq. 6.2 and Eq. 6.7 to determine the critical stress conditions at failure,

$$(\sigma_{\theta\theta})_c = \frac{1}{\sqrt{2\pi r}}\cos\frac{\theta_0}{2}\left[K_I\cos^2\frac{\theta_0}{2} - \frac{3}{2}K_{II}\sin\theta_0\right] + T\sin^2\theta_0 + O(r^{1/2}) \tag{6.8}$$

where $(\sigma_{\theta\theta})_c$ is the critical circumferential stress at a critical distance r_c. For pure mode I fracture when K_{II}, T, and θ_0 are equal to zero, and Eq. 6.8 reduces to

$$\sqrt{2\pi r_c}(\sigma_{\theta\theta})_c = K_{Ic} \tag{6.9}$$

where K_{Ic} is the fracture toughness of the material. Therefore, the onset of fracture can be defined as

$$K_{Ic} - T\sqrt{2\pi r_c}\sin^2\theta_0 = \cos\frac{\theta_0}{2}\left[K_I\cos^2\frac{\theta_0}{2} - \frac{3}{2}K_{II}\sin\theta_0\right] \tag{6.10}$$

Eq. 6.5 and Eq. 6.10 define the onset of failure under mixed mode fracture (given a critical radius r_c, notch length a, and notch orientation β). The geometry of finite specimens has an effect on the crack tip stress fields, and so expressions for stress intensity factors must be modified by the addition of a correction factor to enable their use in practical applications [68]. That is, a geometric factor is introduced to the definition of the stress intensity factors,

$$K_c = Y\sigma_c\sqrt{\pi a} \tag{6.11}$$

In the case of center-notched tension specimens [68], the geometric factor is defined as

$$Y = \sqrt{\sec\frac{a}{W}} \tag{6.12}$$

6.2.1 Direction of Fracture Initiation

To solve for the initial deflection angle that dictates crack propagation trajectory, Eq. 6.7 is written as

$$\begin{aligned}
\left[K_I \sin\theta_0 + K_{II}\left(3\cos\theta - 1\right)\right] - \frac{16}{3} T\sqrt{2\pi r_c} \sin\frac{\theta_0}{2}\cos\theta_0 = 0 \\
\frac{K_I}{K_{eff}} + \frac{3\cos\theta - 1}{\sin\theta}\frac{K_{II}}{K_{eff}} - \frac{\frac{16}{3}T\sqrt{2\pi r_c}}{K_{eff}}\frac{\cos\theta_0 \sin\frac{\theta_0}{2}}{\sin\theta_0} = 0 \\
\frac{K_I}{K_{eff}} + a\frac{K_{II}}{K_{eff}} = b
\end{aligned} \tag{6.13}$$

where

$$a = \frac{3\cos\theta - 1}{\sin\theta} \tag{6.14a}$$

$$\begin{aligned}
b &= \frac{16}{3}\frac{T\sqrt{2\pi r_c}}{K_{eff}}\frac{\cos\theta_0 \sin\frac{\theta_0}{2}}{\sin\theta_0} \\
&= \frac{8}{3} B\alpha \frac{\cos\theta_0}{\cos\frac{\theta_0}{2}}
\end{aligned} \tag{6.14b}$$

and $B = \frac{T\sqrt{\pi a}}{K_{eff}}$ and $\alpha = \sqrt{\frac{2r_r}{a}}$. Now, by letting $z = \frac{K_{II}}{K_I}$, we can rewrite Eq. 6.13 to solve for θ_0,

$$\frac{K_I}{\sqrt{K_I^2 + K_{II}^2}} + a\frac{K_{II}}{\sqrt{K_I^2 + K_{II}^2}} = b \tag{6.15}$$

$$\frac{1}{K_I\sqrt{K_I^2 + K_{II}^2}} + a\frac{1}{K_{II}\sqrt{K_I^2 + K_{II}^2}} = b \tag{6.16}$$

$$\frac{1}{\sqrt{1+z^2}} + a\frac{1}{\sqrt{\frac{1+z^2}{z^2}}} = b \tag{6.17}$$

Rearranging Eq. 6.17,

$$(a^2 + b^2)z^2 + 2az + (1 - b^2) = 0 \tag{6.18}$$

Solving Eq. 6.18 for z,

$$z\left(= \frac{K_{II}}{K_I}\right) = \frac{-a \pm b\sqrt{a^2 - b^2 + 1}}{a^2 - b^2} \tag{6.19}$$

Only the negative solution of Eq. 6.19 is acceptable since θ_0 must be between -90 and 0. Using the definition of the mixity parameter,

$$Me = \frac{2}{\pi}\arctan\left(\frac{K_I}{K_{II}}\right) \tag{6.20}$$

Simplifying,

$$\frac{K_I}{K_{II}} = \frac{\sigma\sqrt{\pi a}\sin^2\beta}{\sigma\sqrt{\pi a}\sin\beta\cos\beta} = \tan\beta \tag{6.21}$$

Replacing Eq. 6.21 in Eq. 6.20 and equating to Eq. 6.19,

$$\begin{aligned}
\frac{2}{\pi}\arctan\left(\frac{K_I}{K_{II}}\right) &= \frac{2}{\pi}\arctan\left(\frac{a^2-b^2}{-a\pm b\sqrt{a^2-b^2+1}}\right) \\
\arctan\left(\tan\beta\right) &= \arctan\left(\frac{a^2-b^2}{-a\pm b\sqrt{a^2-b^2+1}}\right) \\
\beta &= \arctan\left(\frac{a^2-b^2}{-a\pm b\sqrt{a^2-b^2+1}}\right)
\end{aligned} \tag{6.22}$$

We can solve for θ_0 as a function of (β, B, α) using Eq. 6.22 and Eq. 6.14a-6.14b. Fig. 6.3 illustrates the variation of crack deflection angle with respect to notch orientation for an equivalent linear-elastic plate for a range of r_c values. A continuum approach to crack propagation in monolithic brittle materials predicts a gradual transition from a combined stress state to pure Mode I propagation, accompanied by an initial crack deflection.

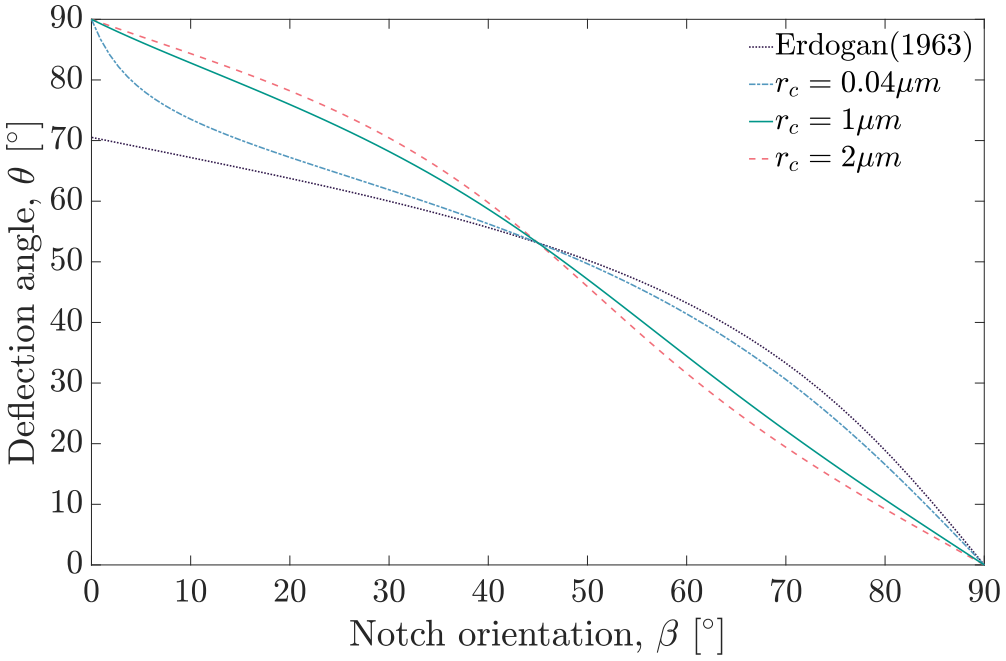

Figure 6.3: LEFM stress-based analytical predictions for crack deflection angle for a center-cracked linear-elastic continuum plate. The deflection angle defines the direction of fracture initiation as a function of notch orientation.

6.2.2 Onset of Failure

A complete solution of a crack propagation problem includes the determination of the onset of failure in addition to the crack path deflection. The dominant fracture mechanism establishes both the onset of crack growth and the crack deflection angle based on the notch orientation and the appropriate characteristic distance. To solve for the stress at the onset of failure, Eq. 6.8 is substituted in Eq. 6.10,

$$\begin{aligned} K_{Ic} = Y\sqrt{2\pi r_c}(\sigma_{\theta\theta})_c &= \cos\frac{\theta_0}{2}\left[K_I\cos^2\frac{\theta_0}{2} - \frac{3}{2}K_{II}\sin\theta_0\right] + T\sqrt{2\pi r_c}\sin^2\theta_0 \\ &= K_I\cos^3\frac{\theta_0}{2} - \frac{3}{2}K_{II}\sin\theta_0\cos\frac{\theta_0}{2} + T\sqrt{2\pi r_c}\sin^2\theta_0 \end{aligned} \tag{6.23}$$

Assuming onset of failure, where σ_f is the critical remote applied stress, the stress intensity factors are

$$K_I = K_{If} = \sigma_f\sqrt{\pi a}\sin^2\beta \tag{6.24a}$$

$$K_{II} = K_{IIf} = \sigma_f\sqrt{\pi a}\cos\beta\sin\beta \tag{6.24b}$$

$$T = T = \sigma_f\sqrt{\pi a}\cos 2\beta \tag{6.24c}$$

The stress intensity factors can be substituted in Eq. 6.24a-6.24c in Eq. 6.23, to obtain the stress at failure as a function the notch orientation and the deflection angle,

$$\begin{aligned} Y\sqrt{2\pi r_c}(\sigma_{\theta\theta})_c &= K_I\cos^3\frac{\theta_0}{2} - \frac{3}{2}K_{II}\sin\theta_0\cos\frac{\theta_0}{2} + T\sqrt{2\pi r_c}\sin^2\theta_0 \\ &= (\sigma_f\sqrt{\pi a}\sin^2\beta)\cos^3\frac{\theta_0}{2} - \frac{3}{2}(\sigma_f\sqrt{\pi a}\cos\beta\sin\beta)\sin\theta_0\cos\frac{\theta_0}{2} \\ &+ (\sigma_f\sqrt{\pi a}\cos 2\beta)\sqrt{2\pi r_c}\sin^2\theta_0 \\ &\vdots \\ (\sigma_{\theta\theta})_c &= \frac{\sigma_f}{Y}\left(\frac{X}{\alpha} - \frac{Q}{\alpha} + Z\right) \\ \frac{\sigma_f}{(\sigma_{\theta\theta})_c} &= \frac{Y}{\left(\frac{X}{\alpha} - \frac{Q}{\alpha} + Z\right)} \end{aligned} \tag{6.25}$$

where

$$\begin{aligned} X &= \sin^2\beta\cos^3\frac{\theta_0}{2} \\ Q &= \frac{3}{2}\cos\beta\sin\beta\sin\theta_0\cos\frac{\theta_0}{2} \\ Z &= \cos 2\beta\sin^2\theta_0 \end{aligned}$$

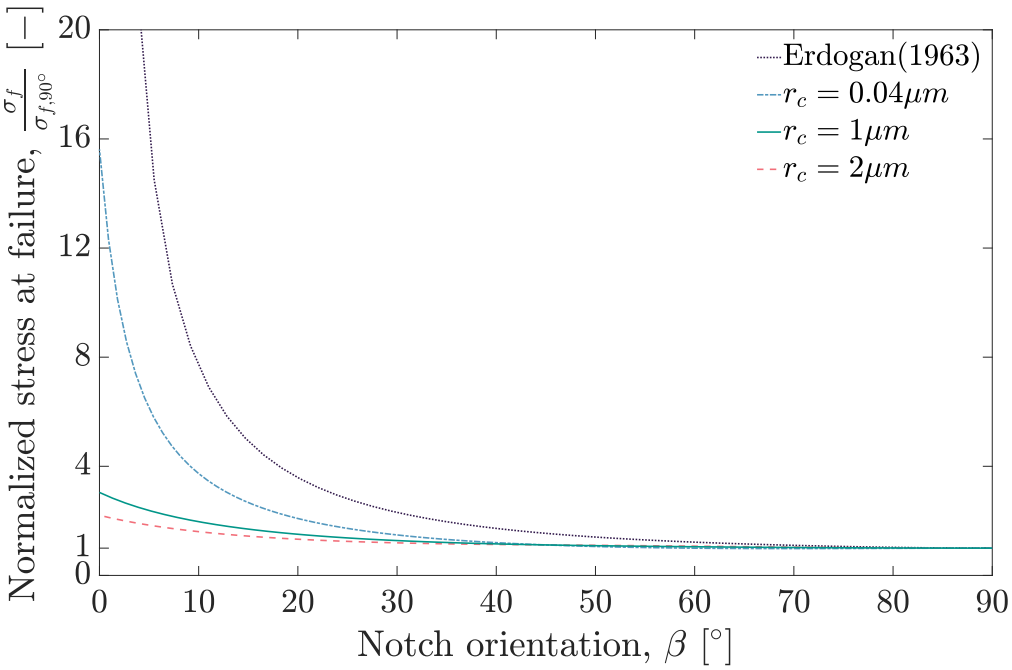

Figure 6.4: LEFM stress-based analytical predictions of stress at failure for a center-cracked linear-elastic continuum plate.

It is convenient to express fracture initiation in mixed-mode loading conditions in terms of the stress intensity factors K_I and K_{II} and converted into normalized mixed mode stress intensity factors, K_I/K_{Ic} and K_{II}/K_{Ic} as shown in Fig. 6.5. The fracture loci predicted by the maximum circumferential stress criteria by Erdogan et al. and the extended failure criteria which takes into account the effects of the T-stress are plotted for comparison.

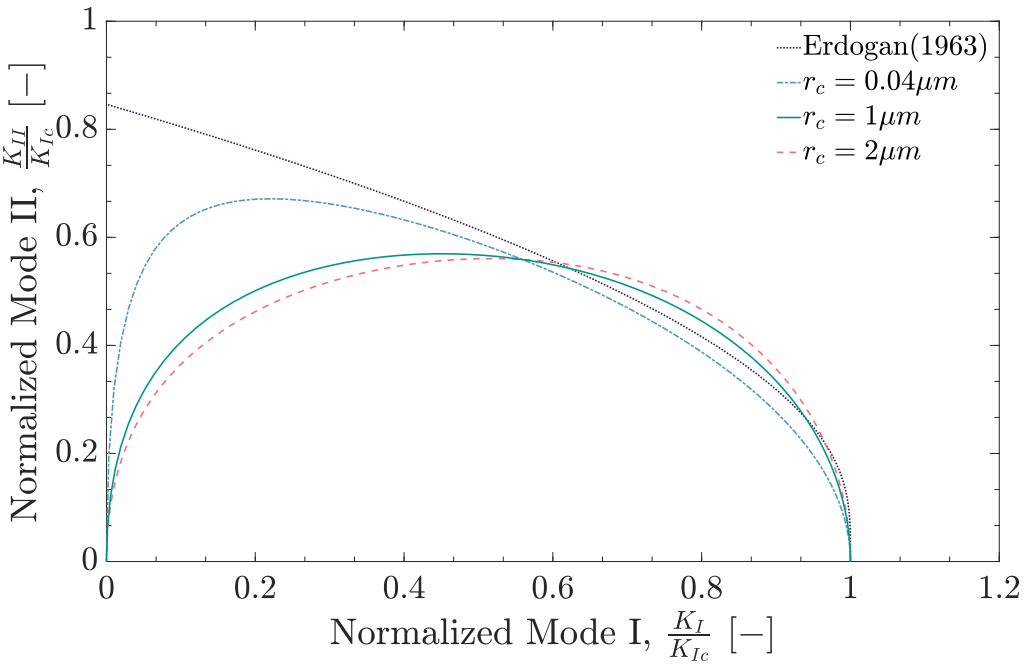

Figure 6.5: LEFM stress-based analytical predictions for mixed-mode failure of a center-cracked linear-elastic continuum plate.

Chapter 7

Continuum-Discrete Aspect of Three-Dimensional Hollow Octet Nanolattices

7.1 Introduction

Failure and fracture are two prominent engineering concepts in the history of mankind; society has been utilizing these concepts to design new structural materials and to build failure-safe structures [74, 75]. Understanding materials' resistance to fracture has allowed us to outperform natural structural materials by engineering novel materials with enhanced properties, like fiber-reinforced composites and bulk metallic glasses. Continuum-based computational models have enabled accurate predictions of mechanical properties of objects of all dimensions and to build structures that are mechanically resilient even under extreme mechanical environments, like the Eiffel tower, the International Space Station, and offshore oil platforms. Failure analysis of such materials and structures has become a customary and mandatory practice where classical beam theories are commonly used to model failure of beam-based structures, i.e. truss-like networks, and conventional continuum-based mechanics is used to describe failure of materials [71, 76].

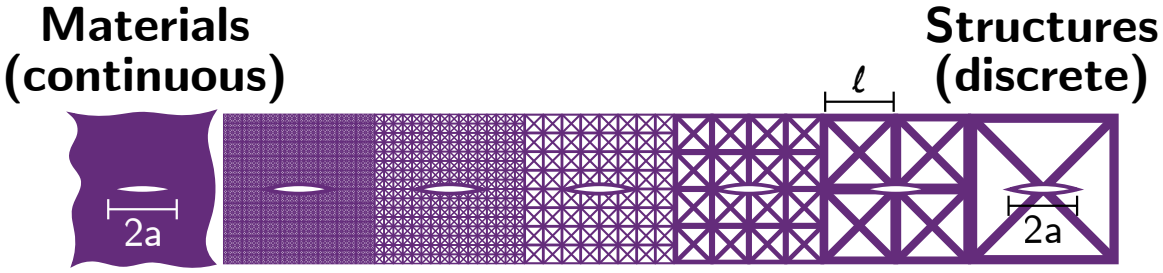

Figure 7.1: As the characteristic features of three-dimensional architected materials are reduced to the microscale, a question arises of whether they are better described as discrete structures or continuum-like materials.

The applicability of continuum-based approaches to describe failure and deformation of architected materials with discrete structural features at small scales, i.e. nano- and micro-lattices [2,77], is unclear. When the characteristic length of discrete architectural features, e.g. beams or tubes, is comparable to macroscopic sample dimensions, the solid is classified as a structure, and its mechanical response can be adequately interpreted using beam theory. As this characteristic length decreases, the mechanical properties of many architected materials can be described using cellular solids theory [36]. When the defining dimensions of the structure, e.g. unit cell size, beam diameter, and wall thickness, are reduced to the same length scale as that of local plastic events that initiate failure, on the order of several microns for engineering ceramics, the deformation of discrete architectural features governs global structural failure and challenges the fundamental assumptions of continuum-based mechanics models. This poses the question whether a cellular solid whose dimensions are on the order of nanometers and micrometers can be identified as a continuum solid with respect to failure, which would enable the use of existing analytical tools to describe structural failure [68,71]. Such a structural metamaterial is characterized by a plastic zone whose size is smaller than the individual features that comprise it, and a characteristic unit cell length that is significantly smaller than the global macroscopic dimensions of the sample.

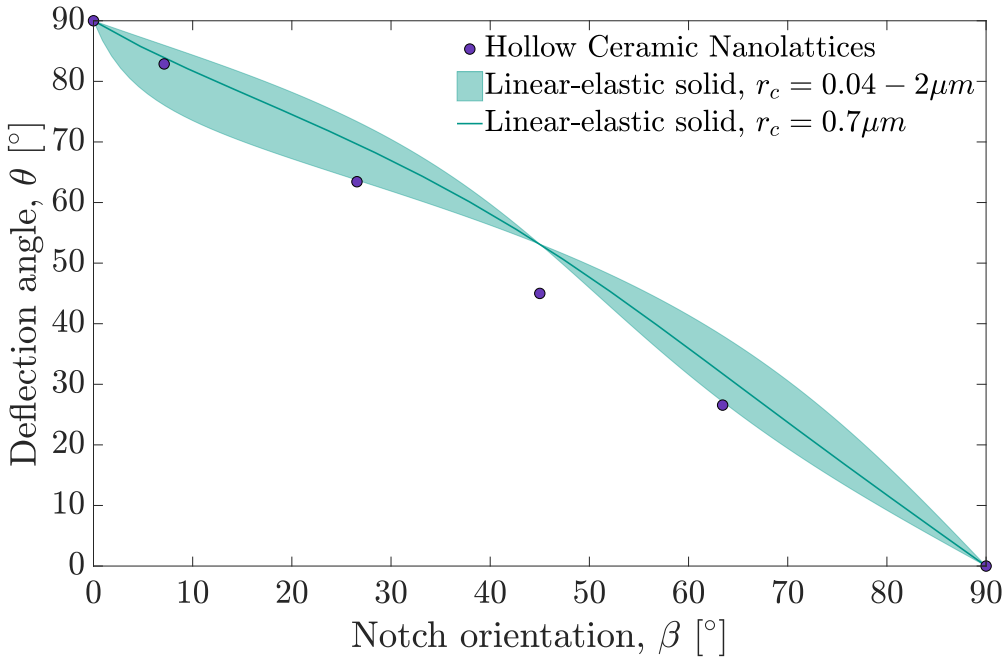

Figure 7.2: Crack deflection angle for hollow-tube octet nanolattices and analytical predictions for an equivalent center-cracked linear-elastic continuum plate. The error bars for the experimental data denote one standard deviation. The continuum-based predictions consist of a shaded area defined by a characteristic distance r_c of $0.04\mu m$ and $2\mu m$, respectively.

7.2 Path of Crack Propagation

Fig. 7.2 illustrates the variation of crack deflection angle with respect to notch orientation for the nanolattices (data points) and that for an equivalent linear-elastic plate (solid line and shaded area). The observed crack path directions in the nanolattices always extend from the notch roots along the axis of the tubes towards the adjacent nodes along a nodal plane that is orthogonal to the loading direction. This failure mechanism stems from the structural effects inherent to lattice architectures: they provide a path of least resistance along the nodal planes, defined by the connectivity of the architecture. Experimental and computational findings for similar nanolattices reveal that the notch roots initially provide the highest stress concentrations [31], where the crack nucleates; and nearly immediately stop serving as the strongest stress concentrators once the crack starts to propagate because the mechanism shifts towards nodal fracture, similar to that in the unnotched nanolattices. The driving failure mechanism of nodal fracture marks the difference in crack path trajectory predictions for continuum solids and for architected materials. For the latter, the local stresses developed in the individual tubes lead to the overall deformation along the tubes' central axis and subsequent crack deflection. In hollow nanolattices, failure is initiated by fracture at the $50nm$ thick tube walls, which is a material-based mechanism. After the initial failure, the pre-defined lattice connectivity drives subsequent rupture such that the fractured surface is oriented orthogonally to the loading direction regardless of the notch orientation, which is in contrast to monolithic solids.

7.3 Onset of Failure

The nanolattices in this work were notched to emulate conditions for conventional fracture experiments in monolithic brittle materials. The octet architecture in this work is categorized as a stretching-dominated cellular solid, whose failure is dictated by the local concentrations of tensile, compressive, and shear stresses within the beams in a unit cell [30, 36]. The effect of these local stresses is even more pronounced in hollow tube-based architectures because tube walls must bear and distribute the global applied load [30, 31, 78, 79]. This suggests that using a stress-based failure criteria is most appropriate to compare the initiation of fracture of an equivalent linear-elastic solid to that of the $50nm$-thick alumina nanolattices [71, 73]. To evaluate whether classical fracture theories, i.e. LEFM, describe a similar failure to that of nano-architected materials, we evaluated the response of an ideally-brittle continuum similar to the architected gauge section of the notched specimens, that is, an equivalent monolithic plate loaded under plane stress conditions and geometrically similar to the center-notched specimens in this work (Fig. 2.3A,B). The onset of failure is predicted by the failure condition previously stated in Eq. 6.6. For clarity, the critical stress at

failure is restated here as

$$\sigma_f\sqrt{2\pi r_c} = \cos\frac{\theta_0}{2}\left[K_I\cos^2\frac{\theta_0}{2} - \frac{3}{2}K_{II}\sin\theta_0\right] + T\sqrt{2\pi r_c}\sin^2\theta_0 + O(r^{1/2}) \tag{7.1}$$

where the magnitude of the first term in the sum is defined by the stress intensity factors (K_I and K_{II}), and the second term represents the stress that contributes to mode I crack opening and accounts for the inherent stress biaxiality in geometries with finite dimensions [75]; commonly known as the T-stress. This biaxiality characterizes the stresses perpendicular to the applied tensile load, which are prominent in center-notched specimens with finite widths. The second term is relevant for mixed-mode loading, under which its magnitude becomes comparable to that of the first singular term. This formulation, as well as other linear elastic fracture criteria, is associated with a material characteristic feature, r_c, that is often identified as the distance that separates the length scale of microscopic damage processes and that of incipient crack growth at the global scale. It is reasonable to assume the critical distance in hollow alumina nanolattices to be less than $1\mu m$, which represents the width of a nodal junction and the thickness of the wall tubes (Fig. 5.2) and is comparable to the characteristic distance and plastic zone size of other engineering ceramics, like alumina and silicon carbide [75, 80, 81].

Fig. 7.3 shows the measured tensile strength of the nanolattices and a range for the possible values for an equivalent linear-elastic solid whose characteristic distance is between $0.04-2\mu m$, which includes estimates of the plastic zone size and characteristic distance for engineering ceramics, and the dimensions of the tube wall thickness and the width of a nodal junction in the nanolattices. The theoretical predictions accurately capture the decrease of tensile strength with decreasing notch orientation, consistent with experiments.

7.4 Tensile-Shear Stress Criterion

These findings imply that knowing the architecture, i.e. lattice connectivity, enables one to define the directional condition that accurately predicts the crack propagation angle and onset of failure as a function of notch orientation. A failure criterion for hollow-tube octet lattices can be formulated where the crack is assumed to be near the notch root at a nodal junction and propagate through the tube walls closely aligned with the plane orthogonal to the applied load. The complex stress at the nodal junctions can be attributed to a combination of tensile and shear stresses. A fracture criterion for linear-elastic failure that takes into account local tensile and shear contributions and assumes a preferred crack deflection angle can be formulated based on the following two assumptions:

1. The crack propagates in a radial direction θ_0 perpendicular to the remote tensile load (directional condition).

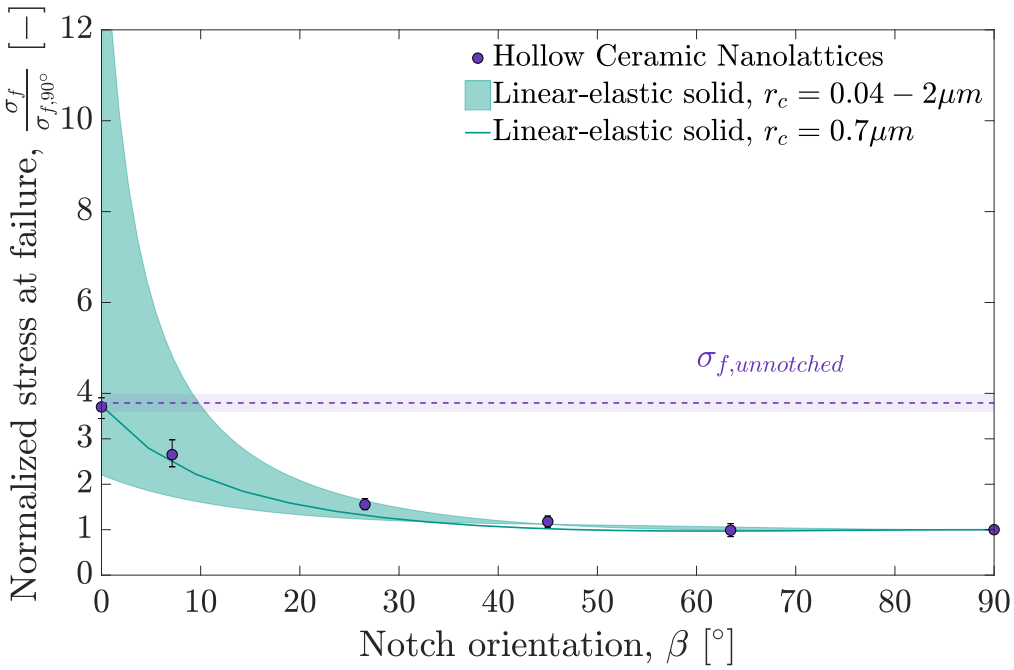

Figure 7.3: Normalized tensile strength for hollow-tube octet nanolattices and analytical predictions for an equivalent center-cracked linear-elastic continuum plate. Variation of normalized critical stress with crack orientation of nanolattices, where error bars denote one standard deviation. Predictions for a plate according to stress-based continuum criteria and net-section strength criterion are also plotted, where the top and bottom boundaries of the shaded area are defined by a characteristic distance r_c of $0.04\mu m$ and $2\mu m$, respectively. The stress at failure for unnotched specimens is plotted as a band centered at the bootstrapped mean and bounded by a 95% confidence interval.

2. Crack propagation initiates when the near field stress $\sigma_f(\theta_0)$, which is defined as a contribution of the tensile $\sigma_{\theta\theta}$ and shear $\tau_{r\theta}$ stresses at a distance r_c from the crack tip, reaches the same critical value as in pure mode I fracture (failure condition).

Consequently, the following failure and directional conditions define fracture initiation, where the critical stress is a function of the local tensile and shear stresses,

$$\theta_0 = \frac{\pi}{2} - \beta \tag{7.2}$$

$$\sigma_f(\theta_0) = \frac{K_{Ic}}{\sqrt{2\pi r_c}} \tag{7.3}$$

$$\sigma_f^2 = \sigma_{\theta\theta}^2 + \lambda \tau_{r\theta}^2 \tag{7.4}$$

Using Eq. 6.2 and Eq. 6.24a-6.24c, the critical tensile stress at the onset of failure is,

$$
\begin{aligned}
(\sigma_{\theta\theta})_c &= \frac{1}{\sqrt{2\pi r_c}} \cos\frac{\theta_0}{2}\left[K_I \cos^2\frac{\theta_0}{2} - \frac{3}{2}K_{II}\sin\theta_0\right] + T\sin^2\theta_0 + O(r^{1/2}) \\
(\sigma_{\theta\theta})_c &= \frac{\sigma_f\sqrt{\pi a}}{\sqrt{2\pi r_c}} \cos\frac{\theta_0}{2}\left[\sin^2\beta\cos^2\frac{\theta_0}{2} - \frac{3}{2}\cos\beta\sin\beta\sin\theta_0\right] + \sigma_f\cos(2\beta)\sin^2\theta_0 \\
(\sigma_{\theta\theta})_c &= \sigma_f\left[\frac{\sin^2\beta\cos^3\frac{\theta_0}{2} - \frac{3}{2}\cos\beta\sin\beta\sin\theta_0\cos\frac{\theta_0}{2}}{\alpha} + \cos(2\beta)\sin^2\theta_0\right] \\
(\sigma_{\theta\theta})_c &= \sigma_f A(\beta,\theta_0,\alpha)
\end{aligned} \tag{7.5}
$$

Similarly, using Eq. 6.3 and Eq. 6.24a-6.24c, the critical shear stress at the onset of failure is

$$
\begin{aligned}
\tau_{r\theta} &= \frac{1}{2\sqrt{2\pi r}} \cos\frac{\theta}{2}\left[K_I\sin\theta + K_{II}(3\cos\theta - 1)\right] - T\cos\theta\sin\theta + O(r^{1/2}) \\
(\tau_{r\theta})_c &= \frac{\sigma_f\sqrt{\pi a}}{2\sqrt{2\pi r_c}} \cos\frac{\theta_0}{2}\left[\sin^2\beta\sin\theta_0 + \cos\beta\sin\beta(3\cos\theta_0 - 1)\right] - \sigma_f\cos(2\beta)\cos\theta_0\sin\theta_0 \\
(\tau_{r\theta})_c &= \sigma_f\left[\frac{\sin^2\beta\sin\theta_0\cos\frac{\theta_0}{2} - \cos\beta\sin\beta\cos\frac{\theta_0}{2}(3\cos\theta_0 - 1)}{2\alpha} - \cos(2\beta)\cos\theta_0\sin\theta_0\right] \\
(\tau_{r\theta})_c &= \sigma_f B(\beta,\theta_0,\alpha)
\end{aligned} \tag{7.6}
$$

The critical stress normalized by the fracture toughness of the effective material can be calculated as a function of the local stress near the crack tip,

$$
\begin{aligned}
\frac{K_{Ic}}{\sqrt{2\pi r_c}} &= \sqrt{(\sigma_{\theta\theta}^2 + \lambda\tau_{r\theta}^2)\Big|_{\theta_0}} \\
\frac{K_{Ic}^2}{2\pi r_c} &= (\sigma_{\theta\theta}^2 + \lambda\tau_{r\theta}^2)\Big|_{\theta_0} \\
\frac{K_{Ic}^2}{2\pi r_c} &= (\sigma_f A)^2\big|_{\theta_0} + \lambda(\sigma_f B)^2\Big|_{\theta_0} \\
\frac{\sigma_f}{K_{Ic}} &= \left.\frac{1}{\sqrt{2\pi r_c(A + \lambda B)^2}}\right|_{\theta_0}
\end{aligned} \tag{7.7}
$$

When the weighting factor λ is assumed to be 0; the classical formulation of failure for brittle fracture is obtained as described in the previous chapter. When the weighting factor λ is 1, local tensile and shear stresses have equal contributions. A dedicated study must be carried out to properly evaluate an adequate value of λ for an architected material based on the stress contributions at the unit cell length scale.

7.5 Net Section Yielding

For center-notched specimens, failure could also emanate from yielding in the critical net section, i.e., in the ligaments. An empirical relationship to describe net section yielding for center-crack tension panels (Fig. 7.4) has been proposed by a simple residual strength analysis technique derived from experimental observations [82]. The analysis is applicable to center-cracked tension panels with the crack oriented perpendicular to the applied load and it covers the full range of crack lengths, i.e., cracks that span the entire width of the panel down to cracks that span a small percentage of the width. This net-section yielding evaluation is based on the assumptions of linear elastic fracture mechanics to derive a smooth and continuous relation between the stress at failure and the flaw size.The concept of the stress intensity factor is utilized to describe the fracture instability and to uncouple the width as an independent parameter in crack behavior analysis.

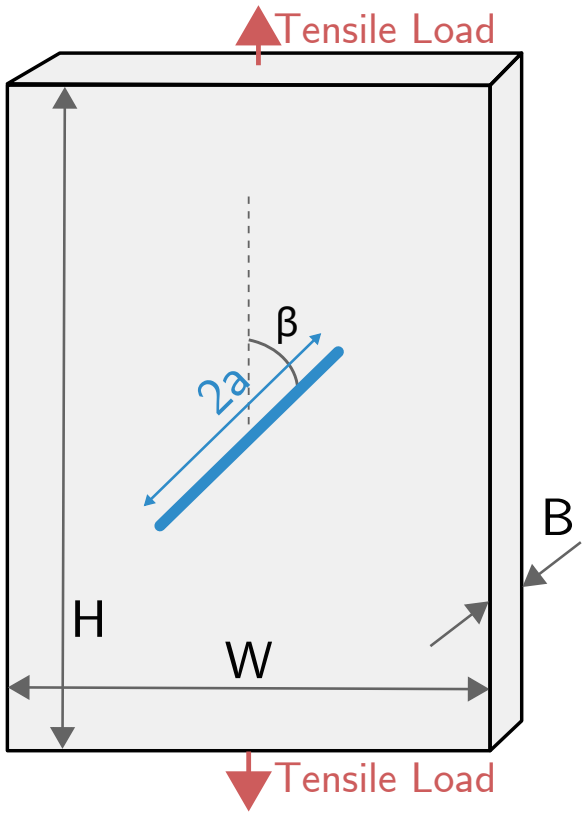

Figure 7.4: Equivalent linear-elastic center-cracked plate.

Fig. 7.5 illustrates the inverse relationship between stress and crack length for elastic fracture behavior. The idealized relationship, which is denoted as a green dotted curve, is derived from the analysis of a panel of infinite size in which a uniform stress field is remotely applied. As illustrated, the curve is parameterized by the stress intensity factor, K. For actual specimens with finite width, this relationship will change due to finite-size constraints. The stress at failure for actual specimens

is elastically limited by the tensile yield strength, and the maximum flaw length is limited by the finite width. These constraints define a net section yield limit, shown as the diagonal line on Fig. 7.5. This line passes through the width limit on the crack length axis and the tensile yield strength at the stress axis, representing a line of constant net section stress. That is, it is the loci of crack length that result in a net section stress on the ligaments of the specimen's cross section. This line also divides the crack behavior into two categories: (1) a plastic instability regime where points fall above and to the right of the net section yielding line, which represent fracture conditions with notable plasticity, and (2) an elastic instability regime where points fall below and to the left of the net section yielding limit, and represent fracture conditions of considerable elastic behavior.

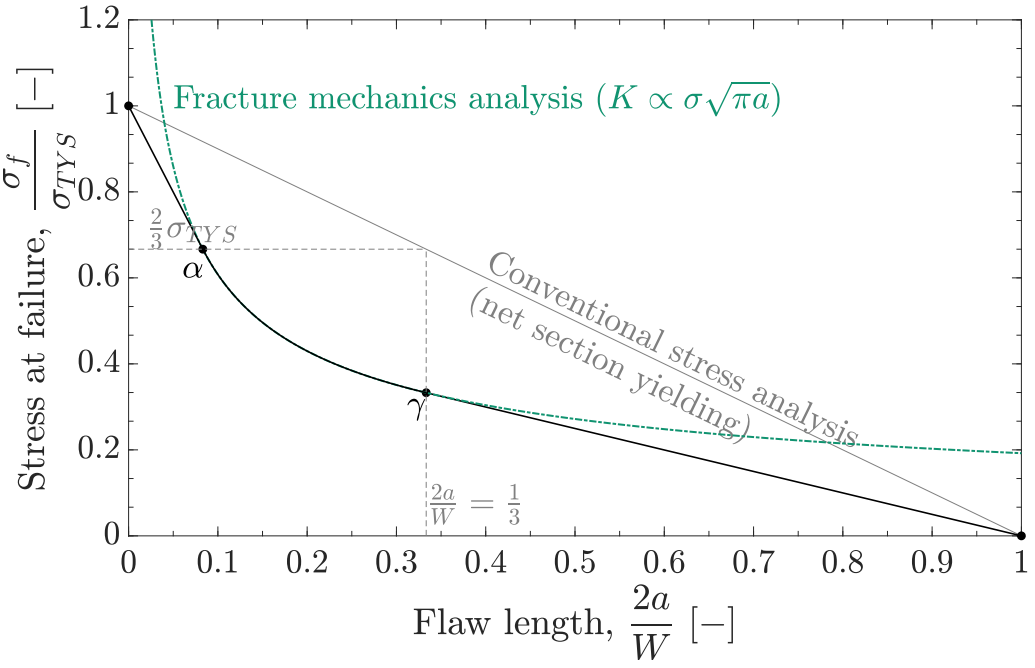

Figure 7.5: Relationship between the stress at failure and flaw length for a center-cracked plate. For an infinite sample, the stresses will follow the green dashed line where failure stresses, σ_f, depend on the flaw size, a, and parameterized by the stress intensity factor, K. If the stresses at failure are associated with yielding at the net section, then a conventional stress analysis can be used to describe the fracture stresses.

In previous work on center-cracked brittle specimens, a linear relation between stress and flaw size was observed at the extremes of the range of values for flaw length [82–86]. This suggested the use of linear tangents to accompany the idealized K curve as a method to account for finite widths; resulting in a smooth and continuous curve of fracture behavior over the full range of crack lengths. Following the method described by Feddersen [82], we can generate a similar net section strength relationship for an equivalent center-notched specimen. The curve is divided into three regions, where the K-derived curve is bounded by two linear regions.

The left-bound linear region can be calculated by knowing that the slope of the K curve at any point in a stress vs. crack length plot is

$$\frac{d\sigma}{d(2a)} = \frac{d}{d(2a)}\left(\frac{K}{\sqrt{4a}}\right) = -\frac{\sigma}{4a} \tag{7.8}$$

This slope is equal to the liner tangents at the extremes of the plot; that is from 0 to point α and from point γ to 1, as illustrated in Fig. 7.5. At point α, the matching condition is

$$\left.\frac{d\sigma}{d(2a)}\right|_{\alpha} = -\frac{\sigma_\alpha}{4a_\alpha} \tag{7.9}$$

$$= -\frac{\sigma_{TYS} - \sigma_\alpha}{2a_\alpha} \tag{7.10}$$

which reduces to

$$\sigma_\alpha = \frac{2}{3}\sigma_{TYS} \tag{7.11}$$

This condition implies that the stress denoted by point α is always at two thirds of the tensile yield strength $sigma_{ultiamte}$. At the other extreme, we have the slope condition at point γ

$$\left.\frac{d\sigma}{d(2a)}\right|_{\gamma} = -\frac{\sigma_\gamma}{4a_\gamma} \tag{7.12}$$

$$= -\frac{\sigma_\gamma}{W - 2a_\gamma} \tag{7.13}$$

which reduces to

$$2a_\gamma = \frac{W}{3} \tag{7.14}$$

This condition represents the linear region for high notch lengths, which indicate that point γ always occurs at one third of the panel width. These two tangent conditions represent the slopes outside the middle region parameterized by K. These conditions are translated into the following screening criterion [82],

These conditions are used to analyze the data and predict fracture behavior in center-cracked tension panels. Given a data point (that is, flaw size and corresponding stress at failure) from an experiment where the notch is aligned perpendicular to the applied tensile load, the complete stress-flaw can be constructed and a K value can be calculated. Therefore fracture behavior can be predicted by evaluating the residual strength at the ligaments of the center-notched tension specimens, which is elastically constrained by the tensile yield strength of the material and geometrically restricted by the finite width of the gauge section.

Table 7.1: Screening criterion to generate a net section yielding relationship between the stress at failure and flaw size.

Region	Condition	Slope
1	$\sigma \geq \frac{2}{3}\sigma_{TYS}$	linear tangent
2	$\sigma \leq \frac{2}{3}\sigma_{TYS}$ $2a \leq \frac{W}{3}$ $K = \sigma\sqrt{\pi a}$	K-derived curve
3	$2a \geq \frac{W}{3}$	linear tangent

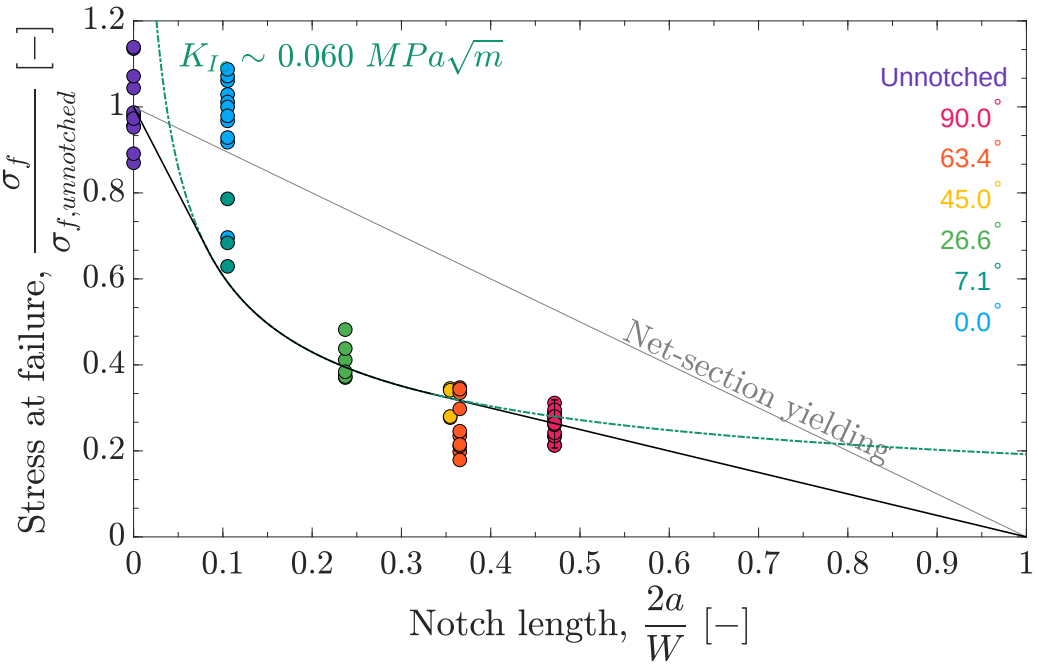

Figure 7.6: Evaluation of net-section yielding by relating the stress at failure with the flaw size. The black curve indicating a smooth, continuous relationship between the stress at failure and the notch length is generated by a K-parameterized regime in the center bounded by two linear regimes at short and long notch lengths. The curve depicted in this plot was generated by fitting a curve through the average dta points for the unnothced case and the 90°-notched specimen, which is the only notched specimen with a horizontal notch. However, by plotting the projected notch length for all other angled specimens, we see that they fall below the net section yielding limit and follow a similar scaling as predicted by the fracture mechanics analysis.

The relationship between critical stress at failure and notch length using the nanomechanical data is shown in Fig. 7.6. This plot conveys that the stresses associated with failure for an equivalent linear-elastic solid are significantly lower than those associated with critical net-section instability (that is, they fall to the left and below the net-section yielding line) and suggests that the finite specimen width might not significantly influence the measurements. It might also be reasonable to dismiss the net section yielding by plastic instability arguments because of the consistent observations

of elastic-only deformation prior to fracture, as evident from the stress-strain response (Fig. 5.3) and cyclic loading-unloading experiments (Fig. 4.2). This analysis suggests that in our experiments, we are truly measuring the influence of notch orientation on the tensile strength without significant boundary effects introduced by the finite width of the specimens; which will interfere with stress concentrations at the notch root and will adversely initiate premature fracture.

The value of K_{Ic} fitted to the experimental data, as shown in Fig. 7.6 fall within the range for fracture toughness of material groups with similar densities and seems to follow the predictions using scaling laws derived from cellular solid theories. However, a dedicated study must be performed to properly define a fracture toughness for three-dimensional architected materials and truly capture the complex hierarchical nature of lattice architectures and their vast combination of geometric parameters and failure mechanisms (as discussed in the following chapter).

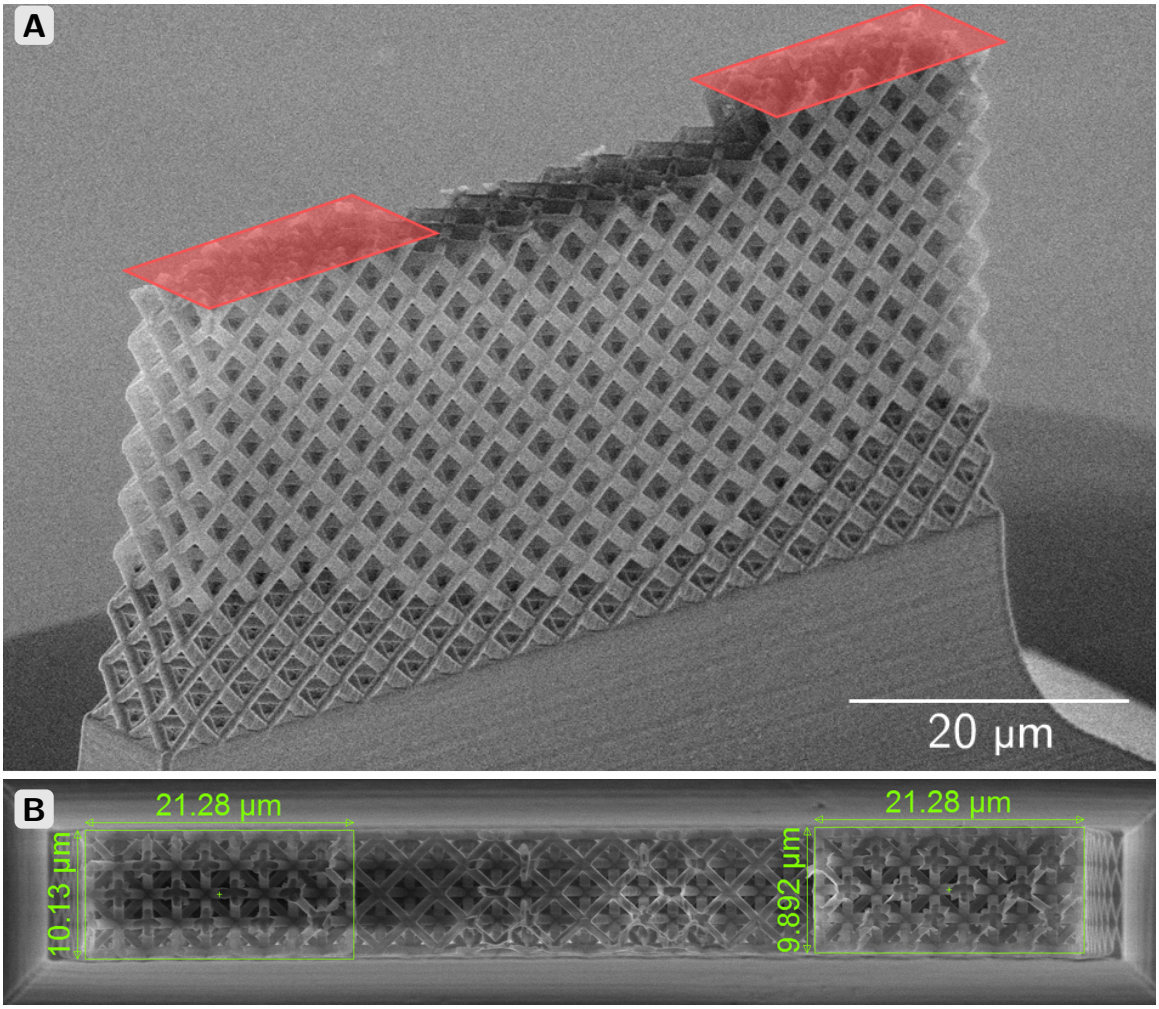

Figure 7.7: The net cross-sectional area of a notched sample is defined as the gross area of the ligaments to the side of the notched and perpendicular to the applied tensile load. (A) SEM image illustrating the net cross-sectional area of a 90°-notched specimen, which is denoted by the highlighted red areas. (B) SEM image of the top view of the cross-sectional area.

A net section strength criteria can also be formulated by describing the stress at failure of notched specimens as a function of the tensile strength of the material and the net cross-sectional area,

$$\sigma_f(\beta) = \sigma_{f,unnotched} \frac{A_{net}(\beta)}{A_{total}} \tag{7.15}$$

where $\sigma_{f,unnotched}$ is the stress at failure for the unnotched case, $A_{net,\beta}$ is the net cross-sectional area as a function of notch orientation β, and A_{total} is the total cross-sectional area, as depicted by Fig. 7.7. Due to the finite length of the unit cells, the cross-sectional area can remain constant for a range of notch orientations. That is, the cluster of structural elements that intersect an infinitesimal crack might remain the same with a change in notch orientation. See Fig. 2.4 for a visual representation of the cluster of elements that are removed to create a notch. This yields a net section strength criteria that is piece-wise linear, as depicted by Fig. 7.8. As the length of the unit cell decreases, this curve becomes smooth and continuous; as expected for a monolithic solid. The stress at failure from the nanomechanical experiments and that predicted by a net section strength criterion is shown in Fig. 7.8. The experimentally measured fracture stresses are significantly less than the stresses associated with net section yielding and do not predict the fracture strengths as well as a fracture mechanics analysis, as seen from previous sections. This conventional stress analysis of residual strengths is not suitable for estimating the fracture strength of notched specimens and suggests that the stresses at failure measured from the nanomechanical experiments depict fracture stresses as function of notch orientation without a significant influence from the finite width of the specimens.

7.6 Stiffness analysis

The stiffness of a linear-elastic solid plate under the same geometric constraints as the samples in this study can be predicted as a function of notch orientation. Assuming linear elasticity, the compliance of a cracked plate under tension is related to the strain energy release rate G by

$$G = \frac{P^2}{2B} \frac{\partial C}{\partial a} \tag{7.16}$$

where P is the applied tensile load, B is the width of the sample, C is compliance, and a is half the crack length. Under plane stress, the strain energy release rate is proportional to the square of the in-plane stress intensity factors K_I and K_{II} as the crack orientation varies,

$$G = \frac{K_I^2 + K_{II}^2}{E} \tag{7.17}$$

Using Eq. 6.4a and Eq. 6.4b as the definition of K_I and K_{II}, Eq. 7.16 can be solved for the compliance of a linear-elastic cracked solid as a function of material properties and sample dimensions,

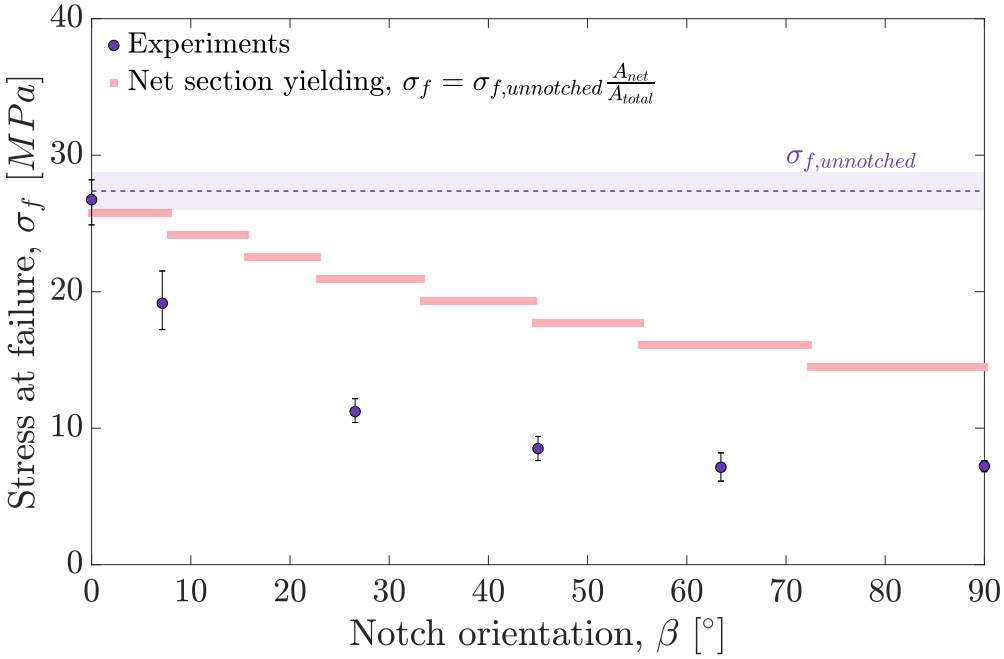

Figure 7.8: A net section strength criteria can be used to evaluate the strength of the ligaments of notched specimens. This criteria describes the stress at failure for notched specimens as a fraction of the tensile strength of the material (that is, the measured stress at failure for the unnotched case) and dictated by the net cross-sectional area. The piece-wise linear fashion of the curve is a result of the discrete nature of the architected material. As the length of the unit cell decreases, this curve becomes smooth and continuous; as expected for a monolithic solid.

which is found to be

$$C = \frac{H}{EBW}\left[1 + 2\pi\frac{W}{H}\left(\frac{a}{W}\right)^2 \cos^2\beta\right] \tag{7.18}$$

This calculation is compared to the experimental stiffness data in this study, shown in Fig. 7.9. The average material properties and global dimensions used for this calculation is listed in Table 7.2.

Table 7.2: Effective material properties and geometric constants used for computing the stiffness of an equivalent linear elastic plate as a function of notch orientation

Parameter	Value
Unit cell length, L	5 μm
Gauge section depth, B	(2 x L) μm
Gauge section width, W	(17 x L) μm
Gauge section height, H	(27 x L) μm
Crack length, a	19.45 μm
Young's Modulus, E	1.30 GPa

Using this approach, it appears that the specimens with the highest failure strength follow the expected trend in stiffness of the equivalent continuum plate as a function of notch orientation.

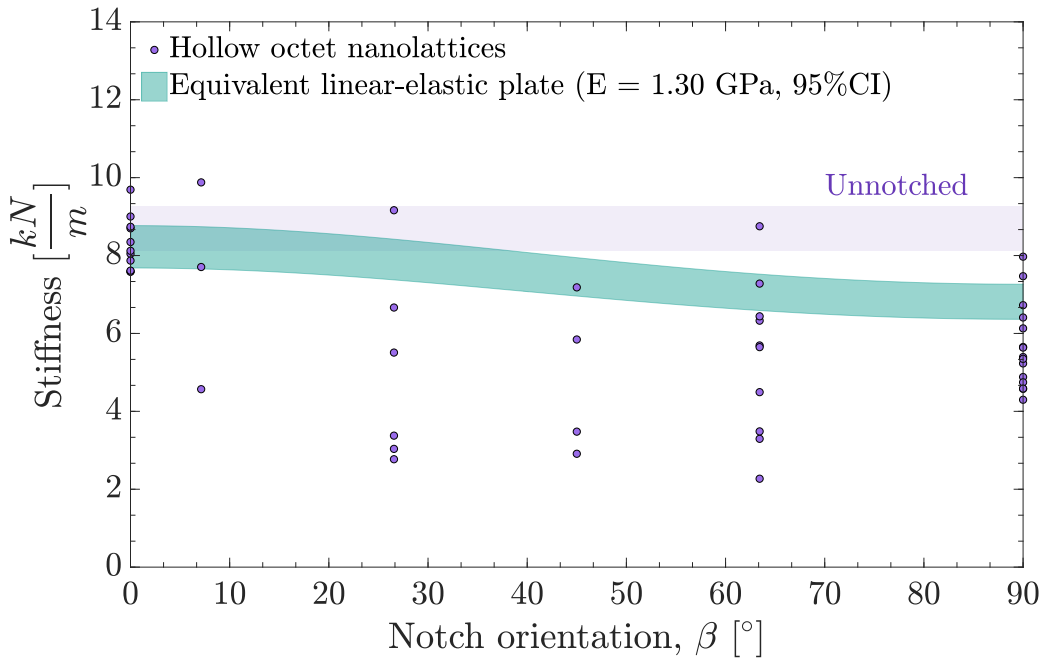

Figure 7.9: Stiffness for hollow octet nanolattices tested in this study and that of an equivalent linear-elastic solid as a function of notch orientation. The stiffness for the unnotched samples are also plotted as a band corresponding to a 95% confidence interval centered at the mean stiffness for all unnotched samples.

The failure strength of samples exhibiting low stiffness is misleading as minor misalignment of the experimental setup can induce non-uniform deformation and inhomogeneous loading. Common to tensile experiments of brittle materials, the sources and magnitude of scatter in strains among geometrically indistinguishable specimens are attributed to experimental misalignment that contribute to an initial low stiffness region and premature failure.

7.7 Failure Envelope

The failure criteria can ve visuallre represented by using Eq. 6.4a through Eq. 6.4d to convert the stress intensity factors into normalized mixed mode stress insentisity factors, K_I/K_{Ic} and K_{II}/K_{Ic}, as shown in Fig. 7.10. These curve represent the fracture loci of combinations of stress intensity factors that indicate the initiation of failure. The experimental results within the curves described by a liner elastic fracture mechanics. Fig. 7.10 shows that for high notch orientations, fracture occurs at low stress intensity factors near zero, where the T-stress is dominant. Contribution from the T-stress can be better illustrated by plotting the effective stress intensity factor K_{eff} normalized by K_{Ic} against the T-stress normalized by the fracture stress σ_c, as shown in Fig. 7.11. For high values of notch orientation, the effective stress intensity factor is low and the T-stress is positive;

and for low values of notch orientation, the effective stress intensity factor is high and the T-stress is positive. Fracture is more dictated by the T-stress for low low notch orientations [71–73]. For moderate notch orientations ($\beta \sim 60°$), the T-stress is negligible and fracture is dominated by the singular term in the series expansion. When $T/\sigma_c = 1$, the notch is oriented parallel to the applied load and failure is dictated by the weakest point in the gauge section, similar to the unnotched case. In this orientation, there is negligible crack opening so the effective stress intensity factor is zero and failure is dominated by the non-singular term of the series expansion.

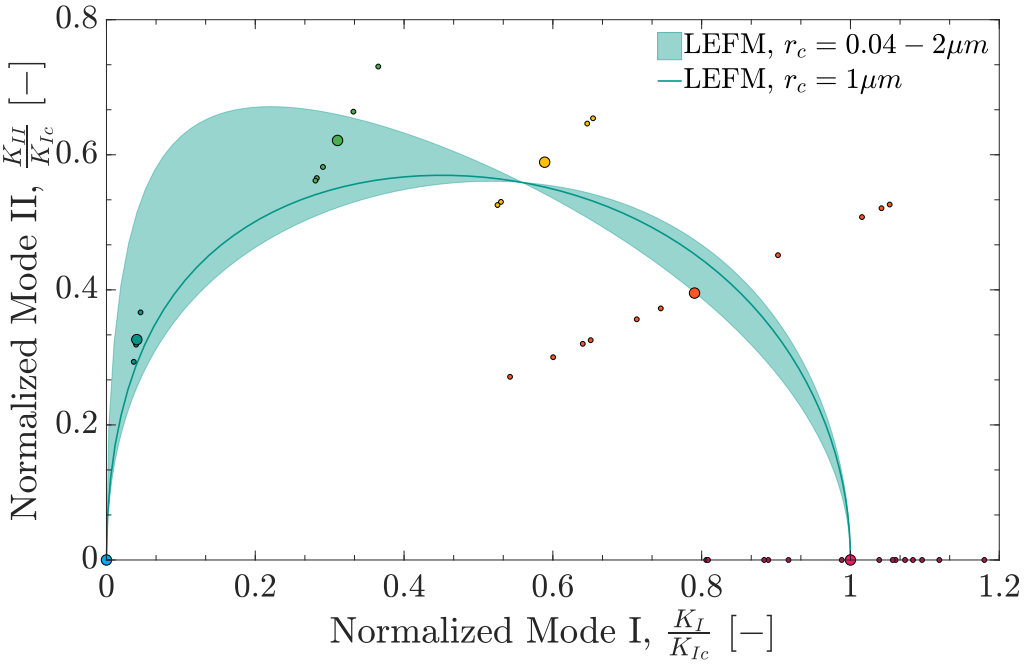

Figure 7.10: Mixed-mode fracture loci for hollow octet nanolattices and for an equivalent center-notched linear-elastic continuum solid.

7.8 Finite Element Modeling

In collaboration with Yong-Wei Zhang (Institute of High Performance Computing, A*STAR, Singapore) and Huang Wei (Northwestern Polytechnical University, Xian, China), numerical simulations were performed to measure the response of nanolattices under tensile loads. Three-dimensional finite element models for the as-designed hollow-tube octet nano-architected gauge sections with and without a through-thickness center notch were created using HyperWorks-constructed sample geometries and are shown in Fig. 7.12. All simulations were performed using the finite element program ABAQUS/Explicit where three-dimensional 4-node quadrilateral shell elements with reduced-integration were employed. A linear-elastic constitutive relation and a brittle damage model were adopted to describe the mechanical response of alumina ceramic. Displacement-controlled boundary

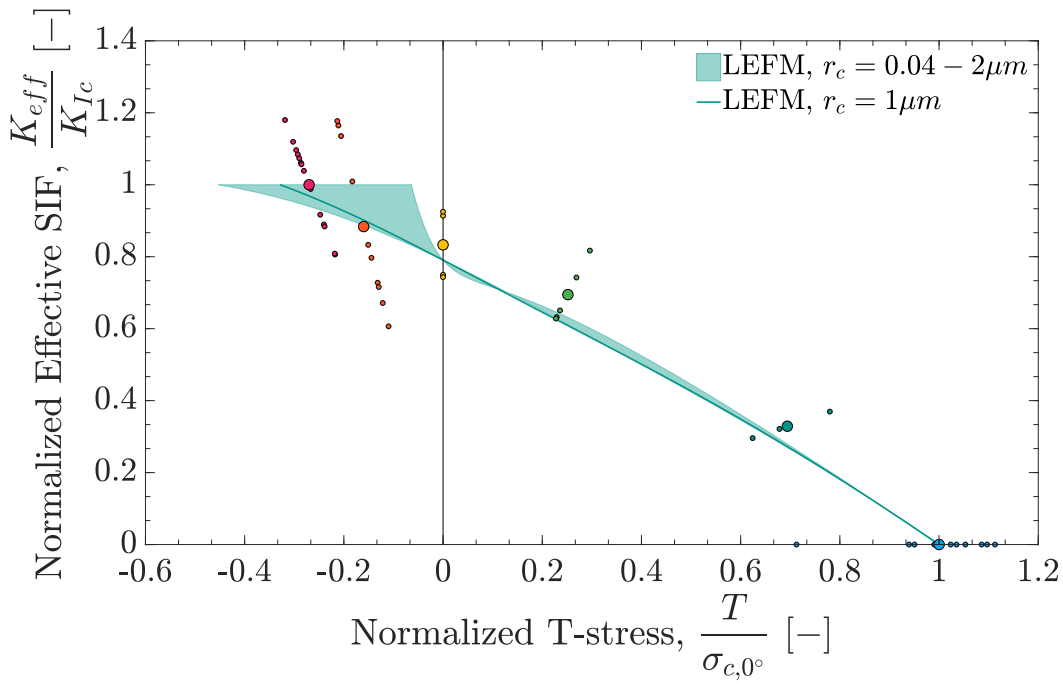

Figure 7.11: Contributions of the T-stress in mixed-mode loading for a center-notched linear-elastic continuum solid and hollow octet nanolattices.

conditions were applied to the finite element model to closely resemble the experimental setup, all the degrees of freedom at the bottom surface of the FE model were fixed, the degrees of freedom of all the nodes on the top surface along the X and Z direction were constrained, and the uniaxial tensile loading was implemented by prescribing displacement applied to the top surface along the Y direction. Explicit dynamics procedure was adopted to simulate the quasi-static uniaxial tension of the notched and unnotched nanolattice samples. During the tensile loading process, the energy balance of the whole system was constantly monitored and enforced with its kinetic energy being less than 1% of the internal energy. The effect of the kinetic energy of the system was negligible compared to its internal energy and external work. A post-processing module (ABAQUS /Viewer) was used to view the analysis results, e.g. reaction forces of nodes, stresses, and strains.

The numerical results from finite element simulations of notched and unnotched samples under uniaxial tensile loading are shown in Fig. 7.13, which are plotted analogously to the experimental results shown in Fig. 5.3. Analogous to Fig. 5.1, the simulated central sections of all samples before and after tensile loading are shown, and each of the seven plots displays a single representative stress-strain data set (solid line) and tensile failure strengths denoted by x. All the samples exhibited an elastic deformation up to instantaneous failure regardless of the existence of a through-thickness notch. The Young's modulus was calculated by fitting the stress-strain data in the strain range between 0 and 2% for each notch orientation, which is plotted by a dashed line.

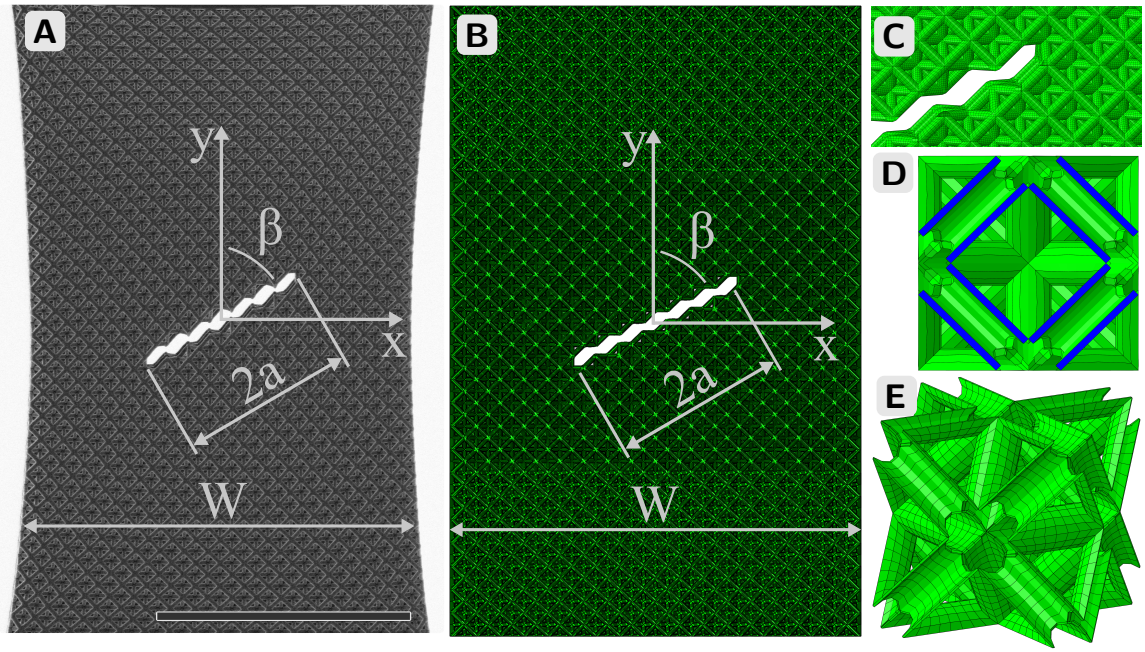

Figure 7.12: Finite element models resembling as-fabricated center-notched tensile geometries. (A-C) SEM image and corresponding finite element model. (D-E) Octet unit cells are composed of shell elements.

Finite element simulations show that the Young's modulus of unnotched nanolattices was the highest among all samples at $1.73GPa$, and that of the notched nanolattices decreased from $1.68GPa$ to $1.31GPa$ as the notch orientation varied from 0 to 90 degrees with respect to the loading direction. The unnotched nanolattices also attained the highest tensile strength of $39.34MPa$ among all the samples; tensile strengths of notched nanolattices decreased monotonically from $31.101MPa$ in vertically notched sample to $8.197MPa$ in orthogonally notched sample, as plotted in Fig. 7.14. The numerical results appear to be in good agreement with the experimental results.

Nano-mechanical experiments showed that for the tensile failure of notched hollow-tube octet architected nanolattices always initiated at the notch roots and instantaneously evolved into brittle fracture along a lattice plane of nodal junctions orthogonal to the loading direction. Similar results were also obtained from FE simulations as shown in Fig. 7.15E,F. In addition, FE simulations also support the experimental observations by revealing that the largest local stress concentrations occurred at nodal junctions near the notch root, and for unnotched nanolattices, the highest stress concentrations occurred at the nodal junctions near the edges (Fig. 7.15C, D). Fig. 7.15C shows the simulated stress distribution for the orthogonally notched sample, which reveals the evolved von Mises stress landscape shortly before failure at a globally applied uniaxial stress of $8.014MPa$, with regions of high stress concentrations of $5.098GPa$ located at the nodal junctions closest to the notch roots. These locations serve as the weakest links within the hollow-tube network and eventually as

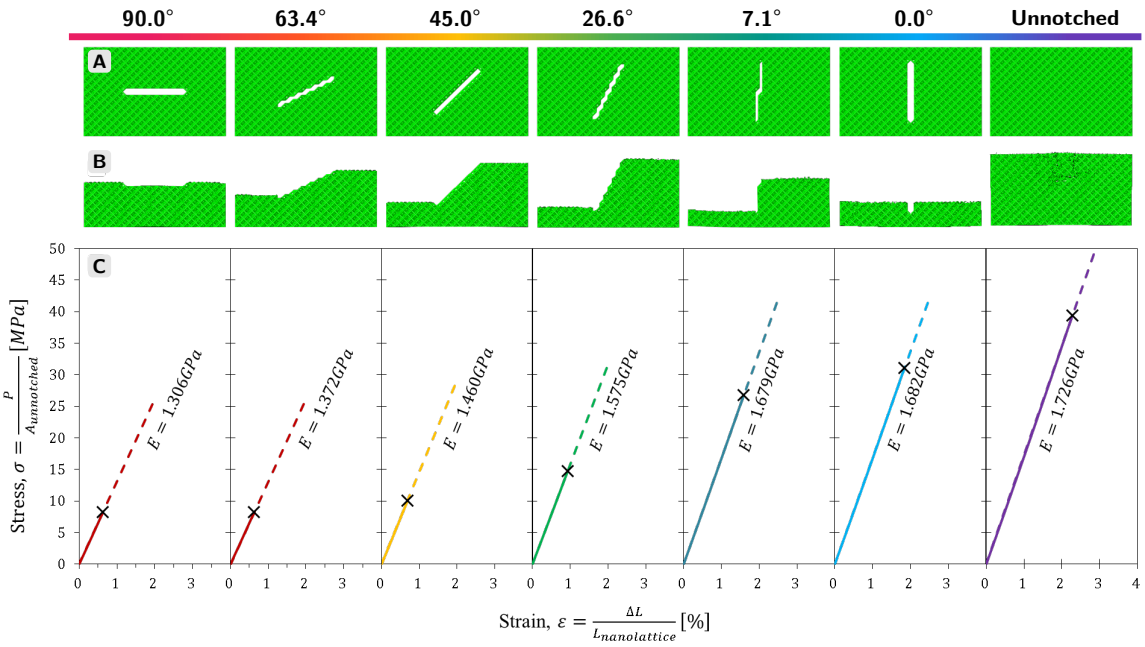

Figure 7.13: Fracture surface morphology and stress-strain response for notched and unnotched nanolattices from finite element simulations. (Rows A, B) Finite element models of octet nanolattices for each notch orientation before and after tensile failure. (Row C) Stress-strain response (solid line) for notched and unnotched nanolattice samples under uniaxial tensile loading were plotted. The point of catastrophic failure is denoted by an 'x' for all samples and the Young's modulus for each notch orientation is plotted by a dashed line.

sites of failure initiation. The magnitude of local stresses at the nodal junctions at the edges of the unnotched nanolattices is a factor of 1.05 higher than those away from the edges, and thus failure is likely to initiate at these stress-concentrated zones. The path of crack propagation in nanolattices depends on the stress distribution at the nodal junctions. The complex local stresses within hollow tube nodes lead to a non-uniform distribution of stresses within the octet unit cell that induce stress concentrations at crevices, i.e. tube intersections, which act as elastic hinges during the tensile loading and dominate the deformation of the unit cell. Failure then extends along the path of high tensile stress concentrations (Fig. 7.15).

These numerical results along with the experimental analysis imply that failure of the hollow octet nanolattices occurs solely by means of tube wall fracture, in the absence of buckling, and the fact that failure propagation trajectory is always orthogonal to the loading direction implies that Mode I fracture plays a dominant role in brittle fracture of these hollow nanolattices. Failure surface morphology and stress-strain response obtained from experiments and finite element simulations closely resemble one another and demonstrate that initial failure always occurred at the nodal junctions with the highest local stress concentrations – at the notch roots in the flaw-containing samples and at the gauge section edges in the unnotched ones – by tearing of the $50nm$-thick alumina nodal junction walls. After this incipient tube wall tearing, global fracture occurred via

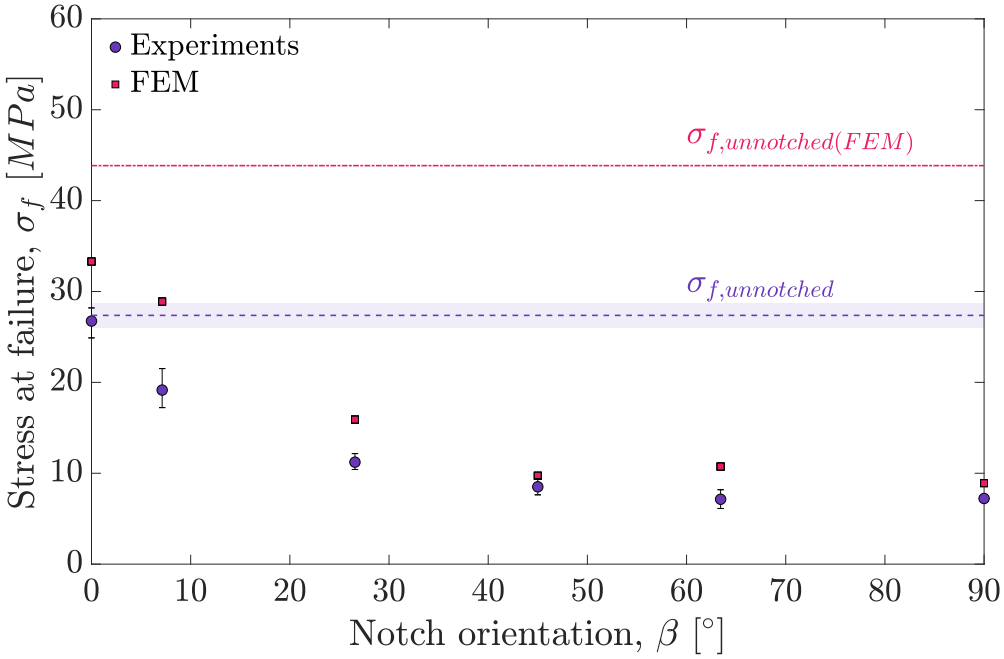

Figure 7.14: Experimental and finite element simulation results for tensile strength of notched and unnothced nanolattices as a function of notch orientation.

brittle fracture of all nodal junctions within parallel lattice planes that emanate from the initially highest stress concentrations that are oriented orthogonally to the applied load, forming fracture planes.

Finite element simulations also enabled the evaluation of crack propagation path as a function of notch geometry and loading conditions. Fig. 7.16 contains FE-generated images of the nanolattice gauge sections with all six notch orientations, with crack propagation contours generated by FE simulations at different strains. The crack deflection plot (Fig. 7.13) and these profiles demonstrate that cracks always extend from the notch roots along the axis of the hollow beams towards the adjacent nodes, and follow a nodal lattice plane that is orthogonal to the loading direction. This failure mechanism stems from the lattice architecture: it provides a percolating surface of least resistance along the nearest-neighbor nodes, which depends on its connectivity. This failure mechanism of nodal-driven fracture is materials- rather than structure-based and marks a key distinction in crack propagation through continuum solids versus architected materials. After the initial failure, the pre-defined lattice connectivity drives subsequent rupture such that the fractured surface is oriented orthogonally to the loading direction regardless of the notch orientation. Simulations indicate that cracks emanate from the notch roots. Our numerical simulations revealed that the critical strain of $\varepsilon = 2.256\%$ was the highest for the unnotched sample and decreased monotonically from$\varepsilon = 1.844\%$ to $\varepsilon = 0.627\%$ for the notched samples as the center notch orientation varied from 0 to 90 degrees

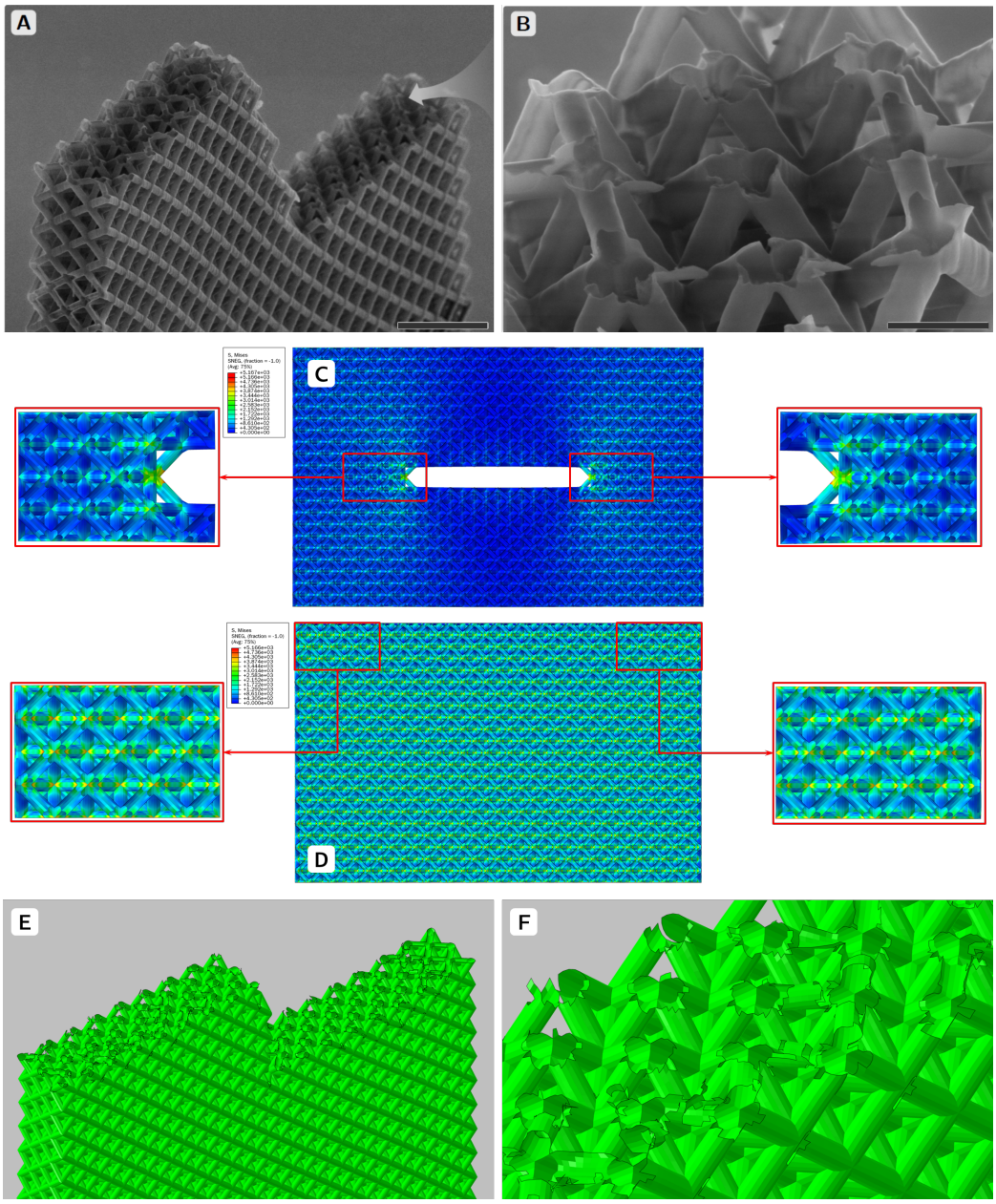

Figure 7.15: Fractographic examination of tensile samples and corresponding finite element simulations. (A) SEM image of a notched sample after tensile failure with arrows pointing at the initial notch. Failure occurred at all nodes along two parallel lattice planes that were adjacent to the notch ends, orthogonal to the loading direction (scale bar: $10\mu m$). (B) Zoomed-in SEM image of fractured nodal junctions and neighboring hollow tubes within those failure planes (scale bar: $2\mu m$). (C) FE-generated contour plots of von Mises stress distributions in the specimen notched at 90 degree with respect to applied tension. Red boxes denote the most stressed nodal junctions, with a maximum stress of 5.167 GPa, where brittle fracture initiated. (D) FE-generated contour plots of von Mises stress distributions in the unnotched nanolattices. (E and F) FE-generated fracture surface morphology of notched nanolattices displayed in the same orientation and relative magnification as SEM images in (A,B).

with respect to the loading direction. Once cracks start to propagate, the maximum stress concentration shifts to the nodes along the nodal plane orthogonal to the loading direction. Since the nodal junctions are the weakest links of the nanolattice structures, the nodal junction failure along the nodal plane orthogonal to the loading direction become inevitable. This mechanism also drives fracture in the unnotched nanolattices. The above analysis supports the experimental observations and suggests that crack propagation deflection is a direct consequence of the discrete nature of architected materials. Finite element analysis revealed the detailed information on the stress distribution in hollow-tube octet lattices, where the crack initiated at a node near the notch root and propagated through the nodes aligned with the plane orthogonal to the applied load.

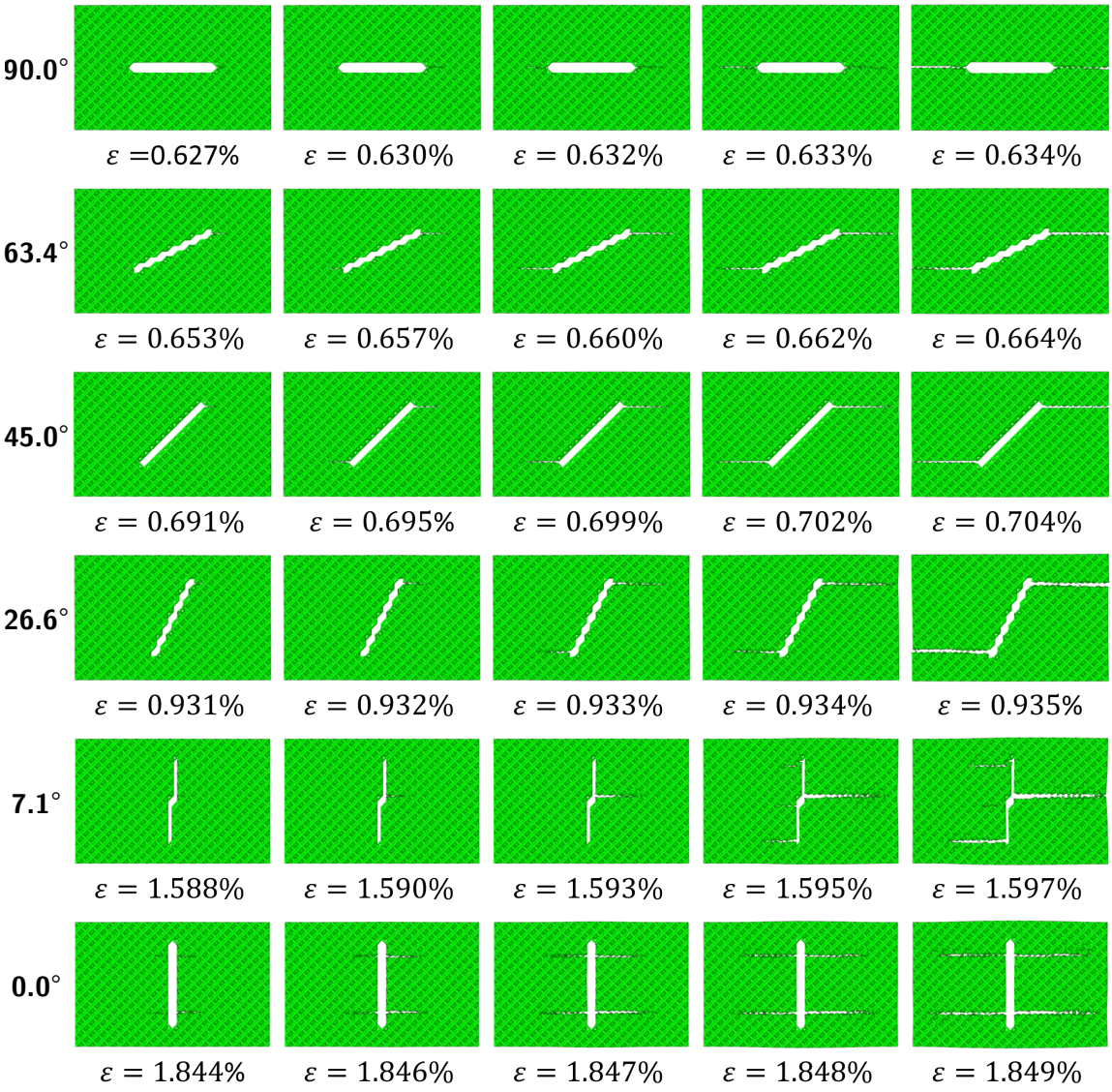

Figure 7.16: Failure propagation paths as a progressing of applied strain of all notched nanolattices subjected to uniaxial tensile loading.

Chapter 8

Conclusions

As the characteristic features of three-dimensional architected materials are reduced to microscale, a question arises of whether they are better described as discrete structures or continuum-like materials. This work reveals that such architected materials, i.e. hollow ceramic nanolattices, have discrete-continuum duality, i.e. they can be treated like continuum materials in the context of flaw sensitivity and failure regardless of the presence, nature, or orientation of the flaws while the discrete lattice architecture enables predictability and control of failure trajectory. Tensile specimens were fabricated and in-situ uniaxial tension experiments on nano-architected 50nm-thick hollow alumina nanolattices were conducted, with some containing pre-fabricated center through-notches oriented at different angles with respect to the loading direction. Nanomechanical experiments revealed that all samples loaded elastically until catastrophic brittle failure along a plane of nodes that is orthogonal to the loading direction. The unnotched samples failed at $27.4MPa$ and the notched ones had a strong dependence of failure strength on notch orientation, decreasing from $26.8MPa$ to the lowest strength of $7.2MPa$ in the samples whose notch was oriented at 90 degrees with respect to the loading direction. The specific tensile strength of 146 $kPa\ kg^{-1}\ m^3$ of the 6.5% dense hollow alumina nanolattices is a factor of ~ 4 higher than what has been previously reported for all architected and bulk materials with similar densities. Treating the geometry of center-notched samples to an equivalent monolithic plate with the same notch, linear elastic fracture mechanics can accurately predict failure stresses and crack trajectory with prior knowledge of the lattice connectivity. The analysis presented in this work demonstrates the characterization of fracture initiation of architected materials based on conventional fracture mechanics for linear elastic materials. These findings reveal that architected materials whose geometries lie within a similar parameter space can be treated like continuum materials in the context of flaw sensitivity and failure regardless of the presence, nature, or orientation of the flaws it might contain. This work demonstrates that prior knowledge of the lattice architecture leads to full control of crack path trajectories in architected materials and has significant implications for designing advanced new materials whose prescribed architecture may allow for engineering the possible crack trajectories upon in-use mechanical loading.

8.1 Open Questions

Over the course of this study, several questions were raised that are outside the scope of this thesis. These questions warrant further investigation. In monolithic materials, satisfying linear fracture mechanics conditions enables measuring a valid fracture toughness (K_{Ic}), which is regarded as a sample geometry-independent material property. LEFM requirements are based on the assumption that the plastic zone at the crack tip is small compared to all relevant length scales associated with the stress field parametrized by K [71]. Fracture toughness measurements are usually carried out according to standardized tests (e.g., ASTM E399, ASTM E1820) developed to determine the point value of plain strain fracture toughness. Fig. 8.1A illustrates a single-edge bending sample that is geometrically similar to the ASTM standards. Microscopic samples, with dimensions on the order of several microns, have been shown to adhere to LEFM assumptions [81], especially in materials with small plastic zone sizes like ceramics, but the non-standard fabrication and testing instruments make it difficult to satisfy the separation of scales required by standardized tests. Fig. 8.1B illustrates the notion of fabricating a three-dimensional specimen whose unit cell length, l, is small compared to the flaw size, $2a$, and the global dimensions of the sample, W. Virtually no fracture experiments that reveal credible fracture toughness on samples smaller than the standard sample dimensions have been reported.

Measuring fracture toughness of architected materials, especially of nano- and micro-architected materials like the ones in this work, introduces further challenges that emanate from additional lattice parameters that influence their fracture resistance; e.g., relative density, beam slenderness ratio, nodal connectivity, and a tube wall thickness [36]. A dedicated study that quantifies the influence of each of these parameters on toughness must be conducted before the notion of fracture toughness for architected materials can be defined (see, for example Refs. 24,26). Fracture toughness has yet to be reliably defined for architected materials because of the multi-scale nature of this problem; with separation of scales that includes local atomic processes, complex local mechanical deformation ahead of the notch root—in the individual beams, junctions, and hollow tubes — is particularly challenging and requires extensive computational development (Fig. 8.1C). Sophisticated models and simulations are necessary to gain insights into fracture toughness of architected materials and to assess whether a discrete-to-continuum transition exists where fracture of three-dimensional architected lattices transitions from a structural analysis of truss-like networks to be fully described by LEFM, as shown by this work.

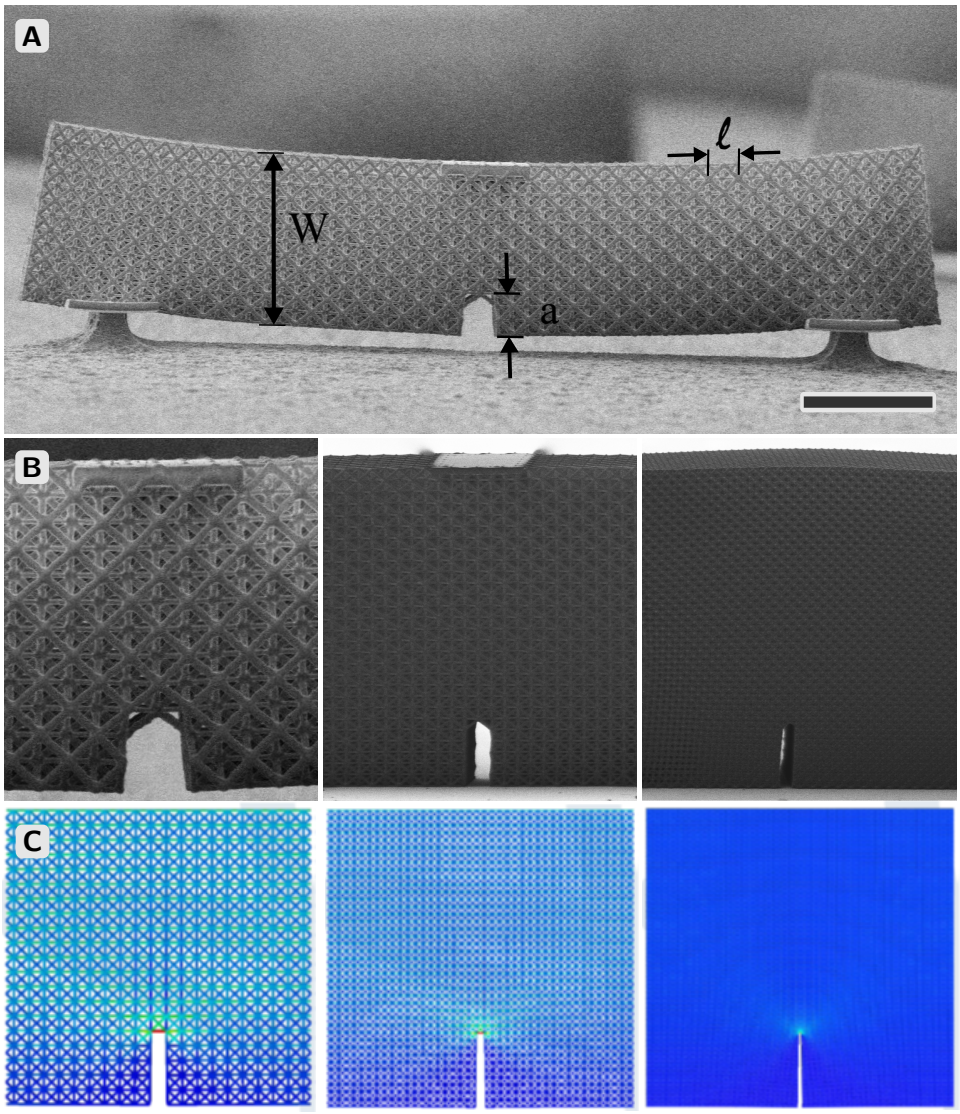

Figure 8.1: Fracture toughness of architected materials. (A-B) SEM image of a single edge notch bending specimen illustrating the notion of fabricating a three-dimensional specimen whose characteristic features at the unit cell length (l) are small compared to the flaw size (a) and the global dimensions of the sample (W). (Row C) Images of FE efforts to characterize the complex stress state of three-dimensional architected materials across multiple length scales. FEA images courtesy of Yong Wei Zhang and Hunag Wei.

Appendix A

Supplemental Videos

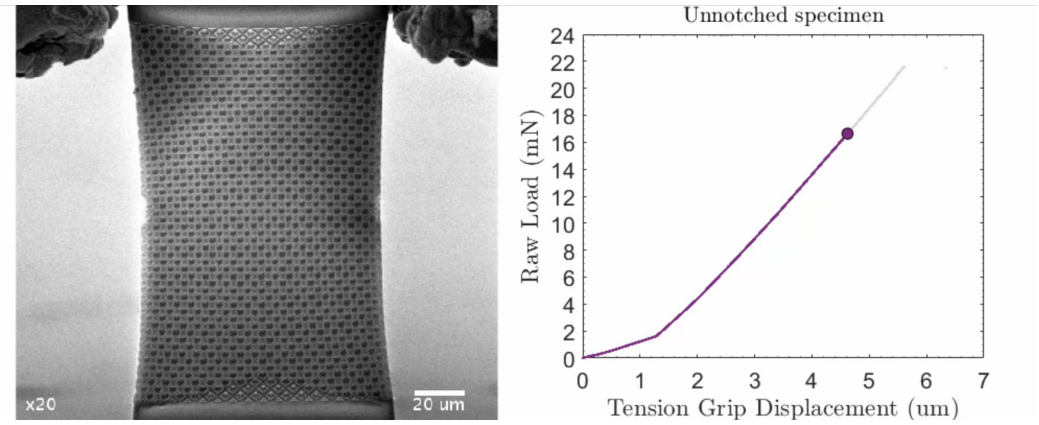

VIDEO S1: In-situ nanomechanical experiment of unnotched sample with corresponding load-displacement data.

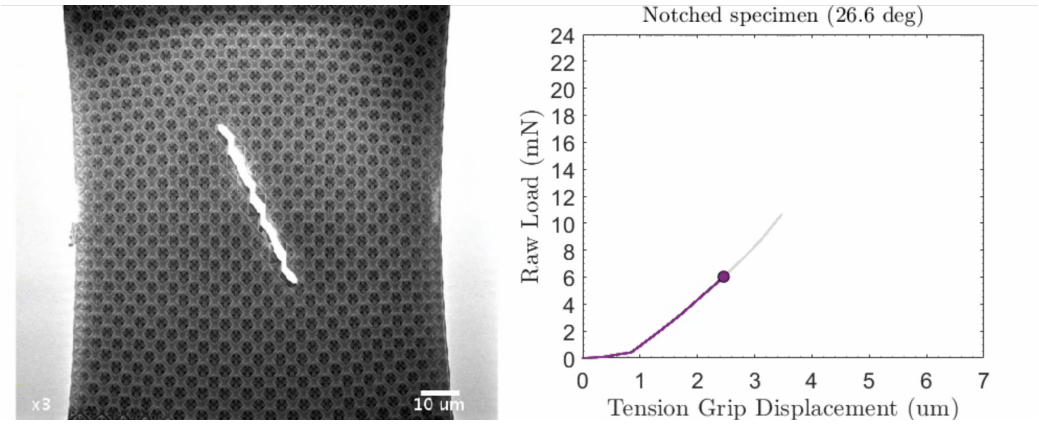

VIDEO S2: In-situ nanomechanical experiment of notched sample with corresponding load-displacement data.

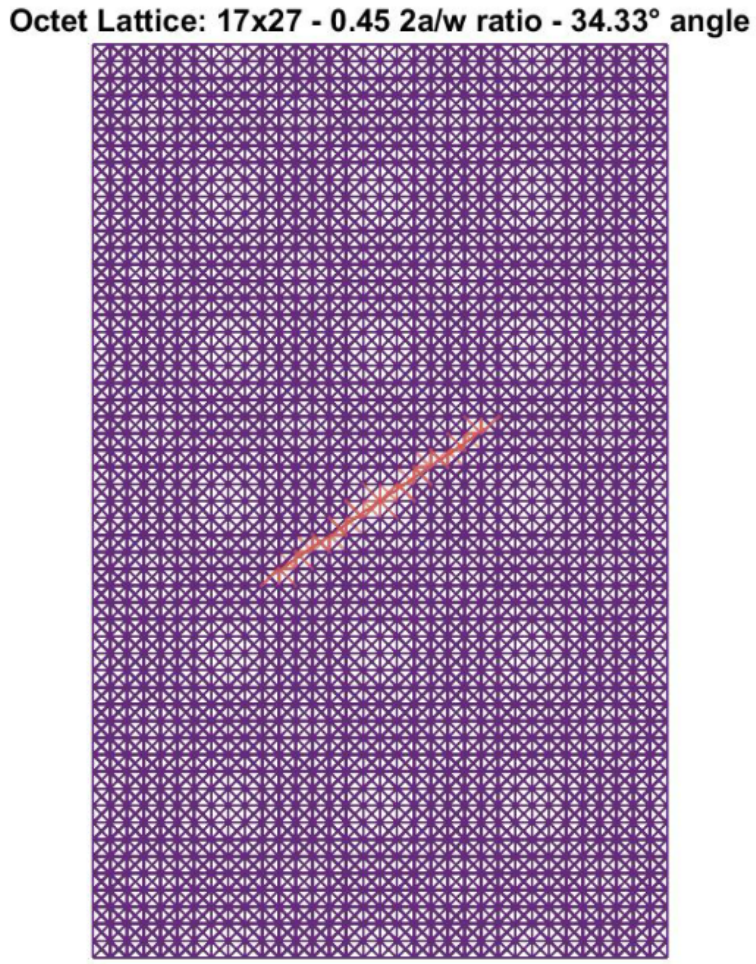

VIDEO S3: Visualization of MATLAB script capable of generating a lattice geometry with a center notch of varying orientation.

Appendix B

Experimental Data

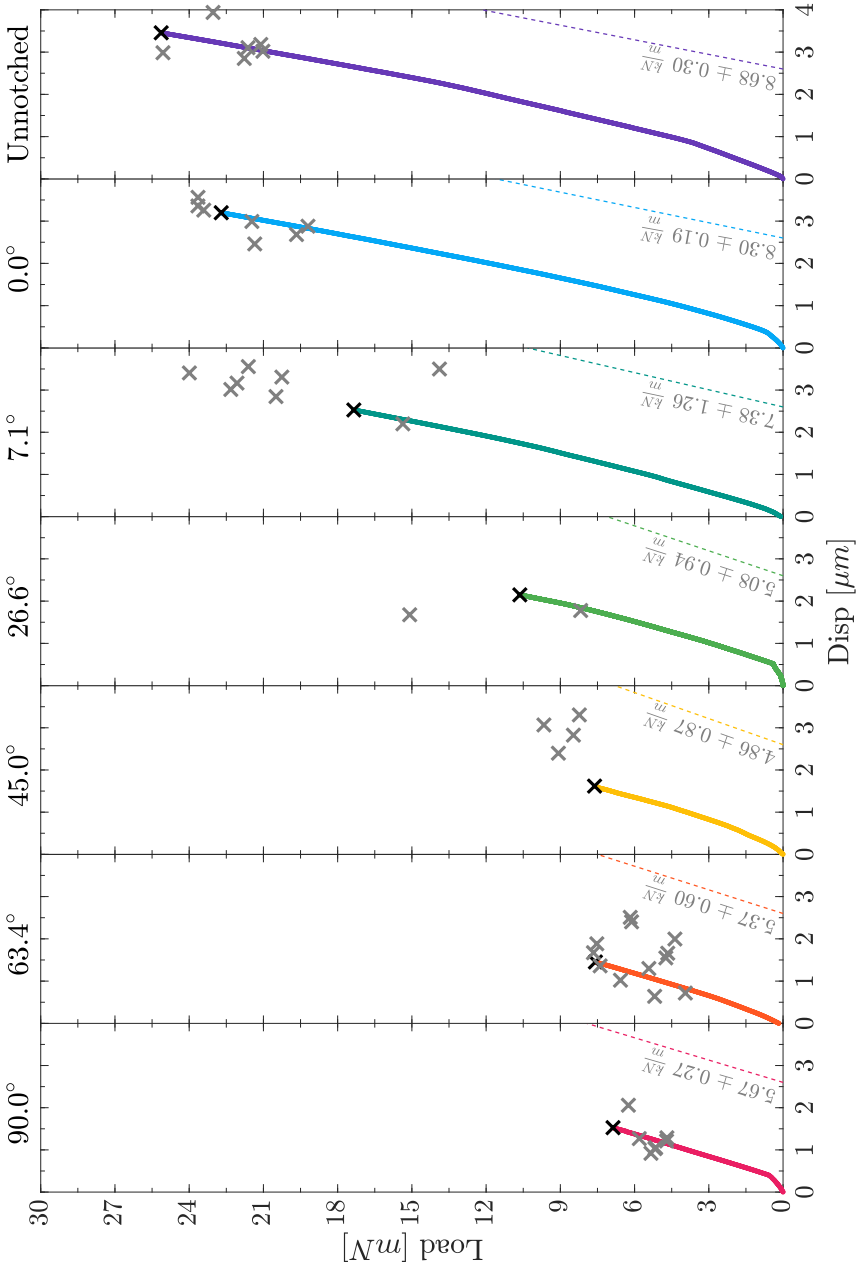

Figure B.1: Representative load-displacement data for notched and unnotched specimens. all tested samples show linear-elastic behavior up to catastrophic failure. The mean stiffness (dotted line) for each case is also plotted. The point at failure is denoted with an 'x' for all tested samples.

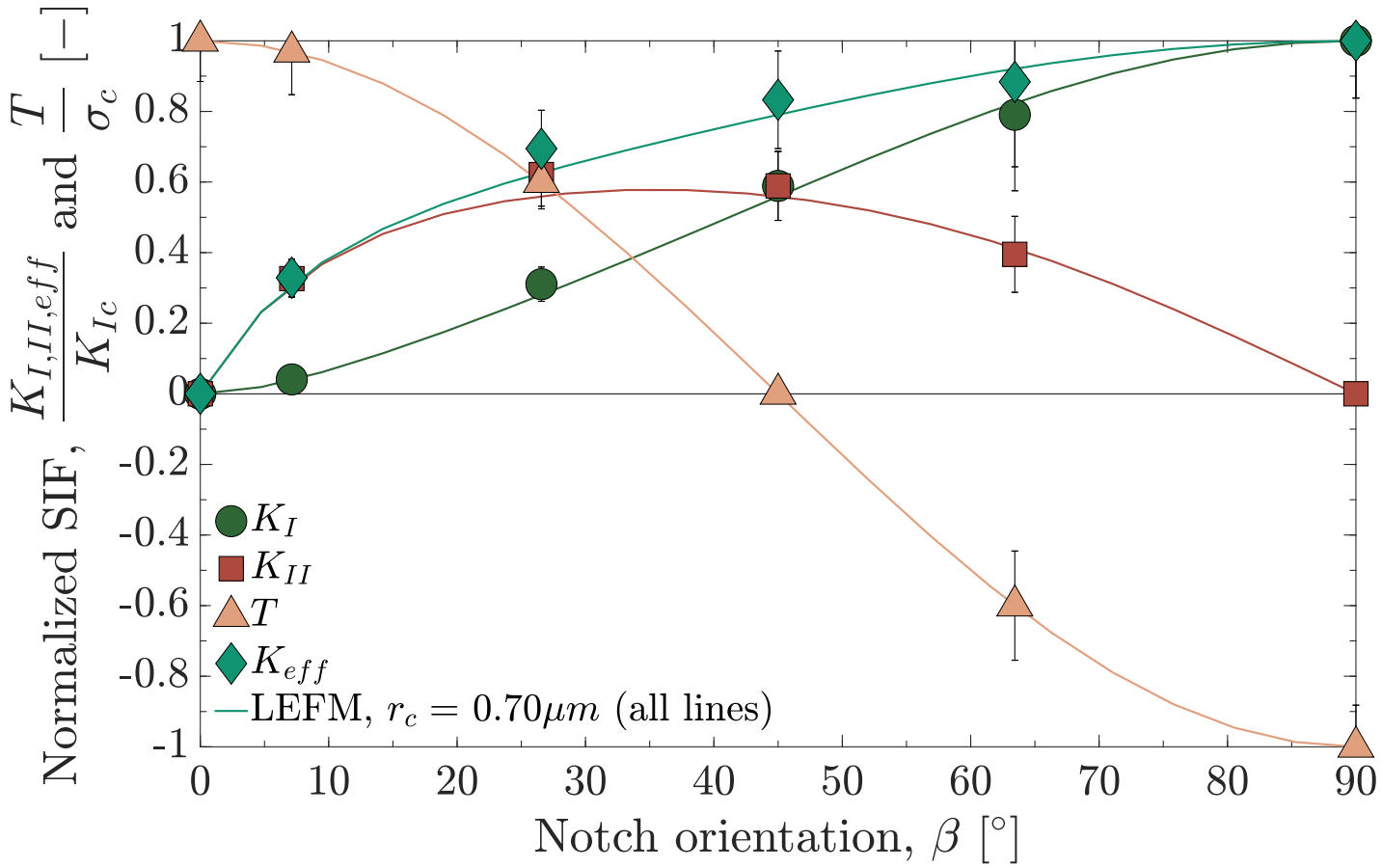

Figure B.2: Normalized K_I, K_II, K_eff, and $T-$stress data. Contributions of the fracture mode is plotted as a function of notch orientation for a homogeneous isotropic elastic solid predicted from linear elastic fracture mechanics (LEFM) and also those from the nanomechanical experiments.

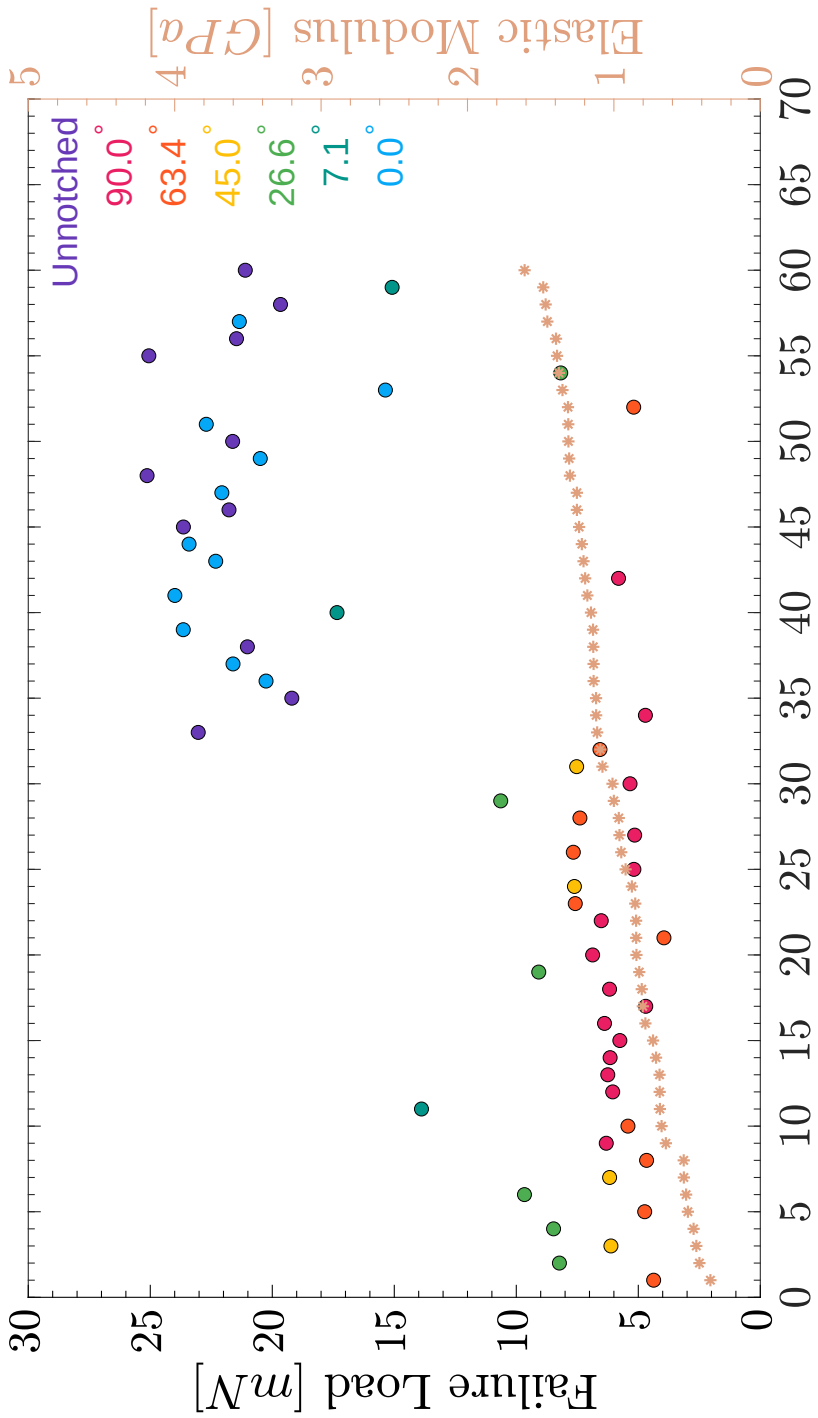

Figure B.3: Experimental data for all tested samples: Failure load and Young's modulus.

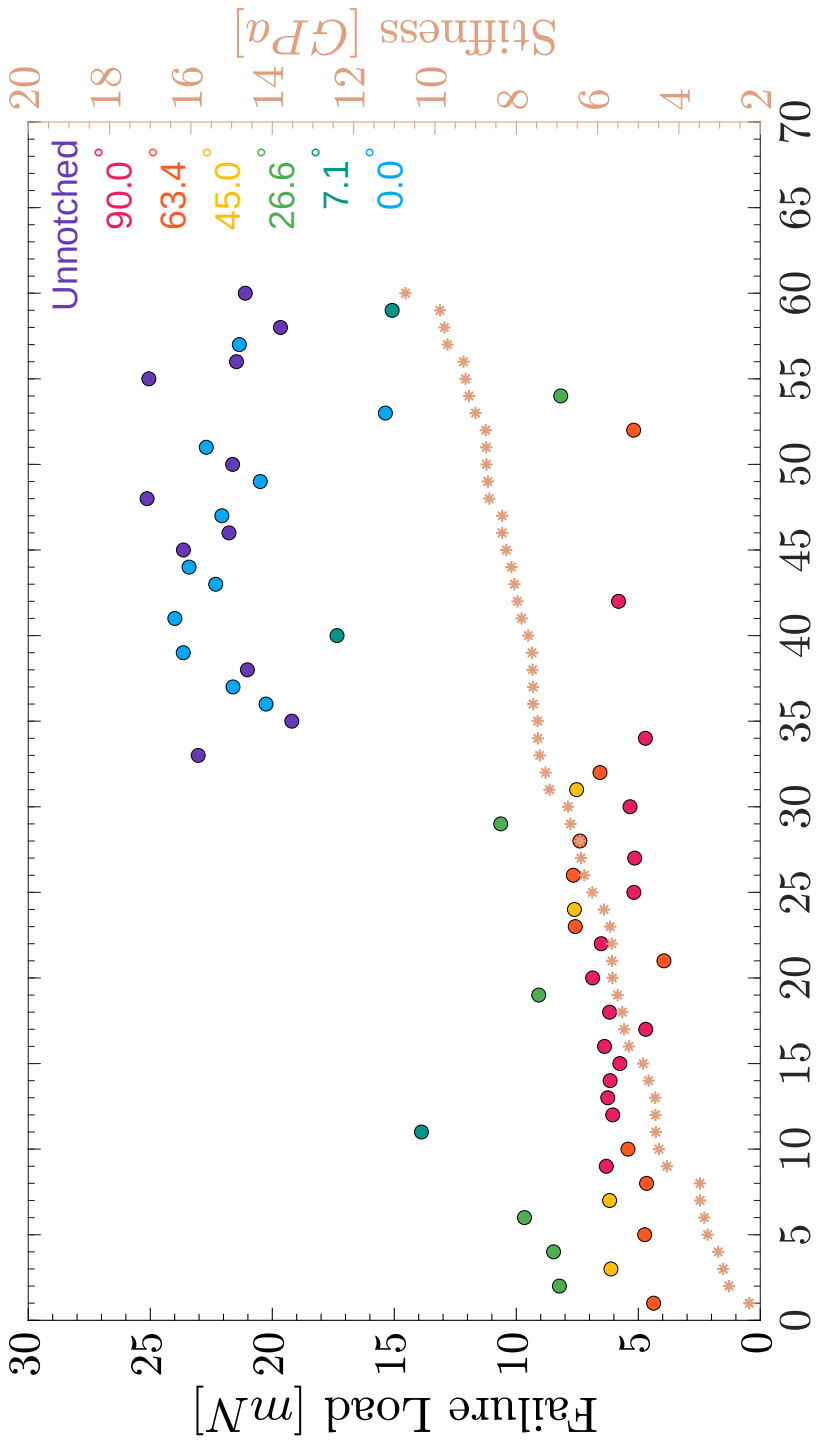

Figure B.4: Experimental data for all tested samples: Failure load and stiffness.

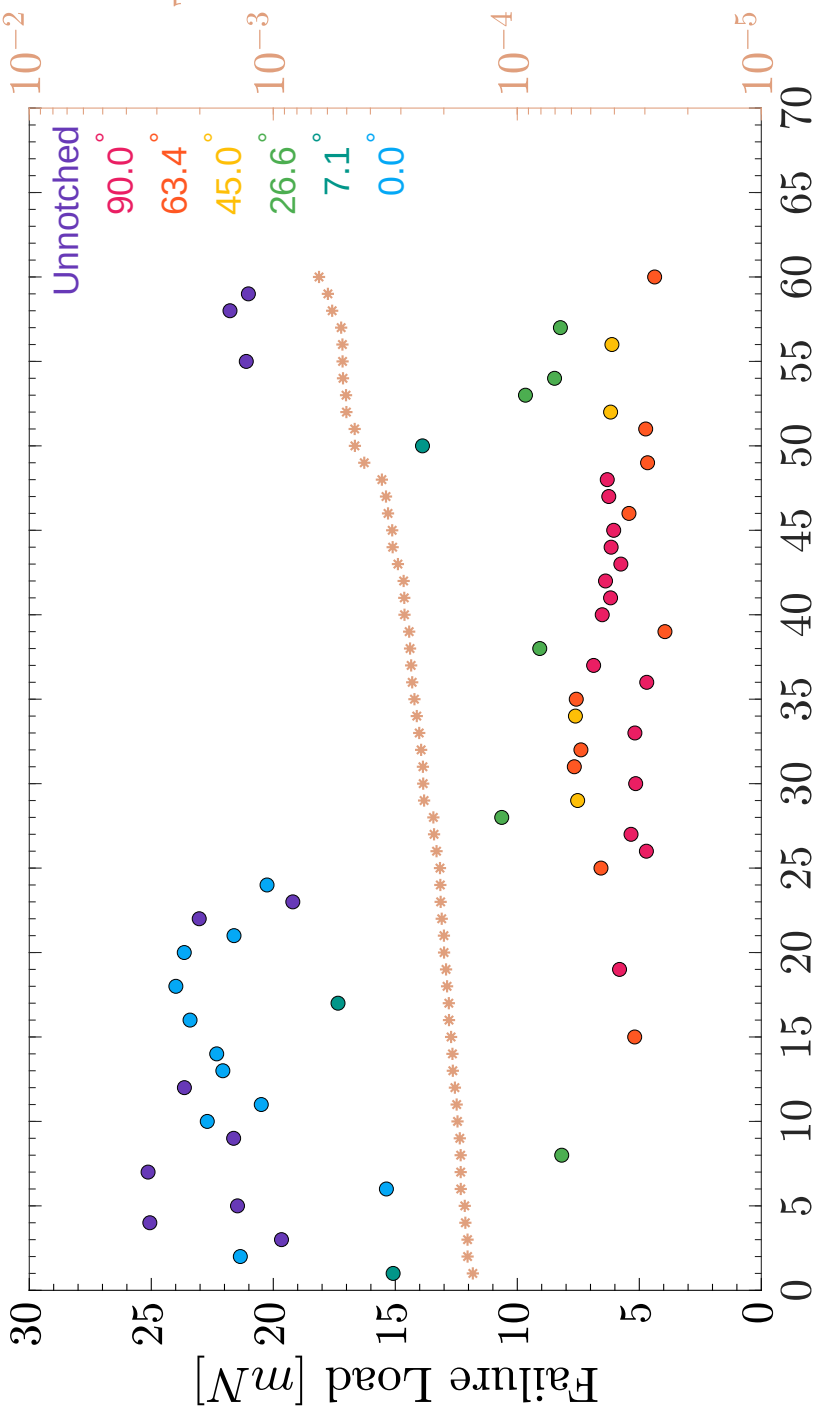

Figure B.5: Experimental data for all tested samples: Failure load and average strain rate.

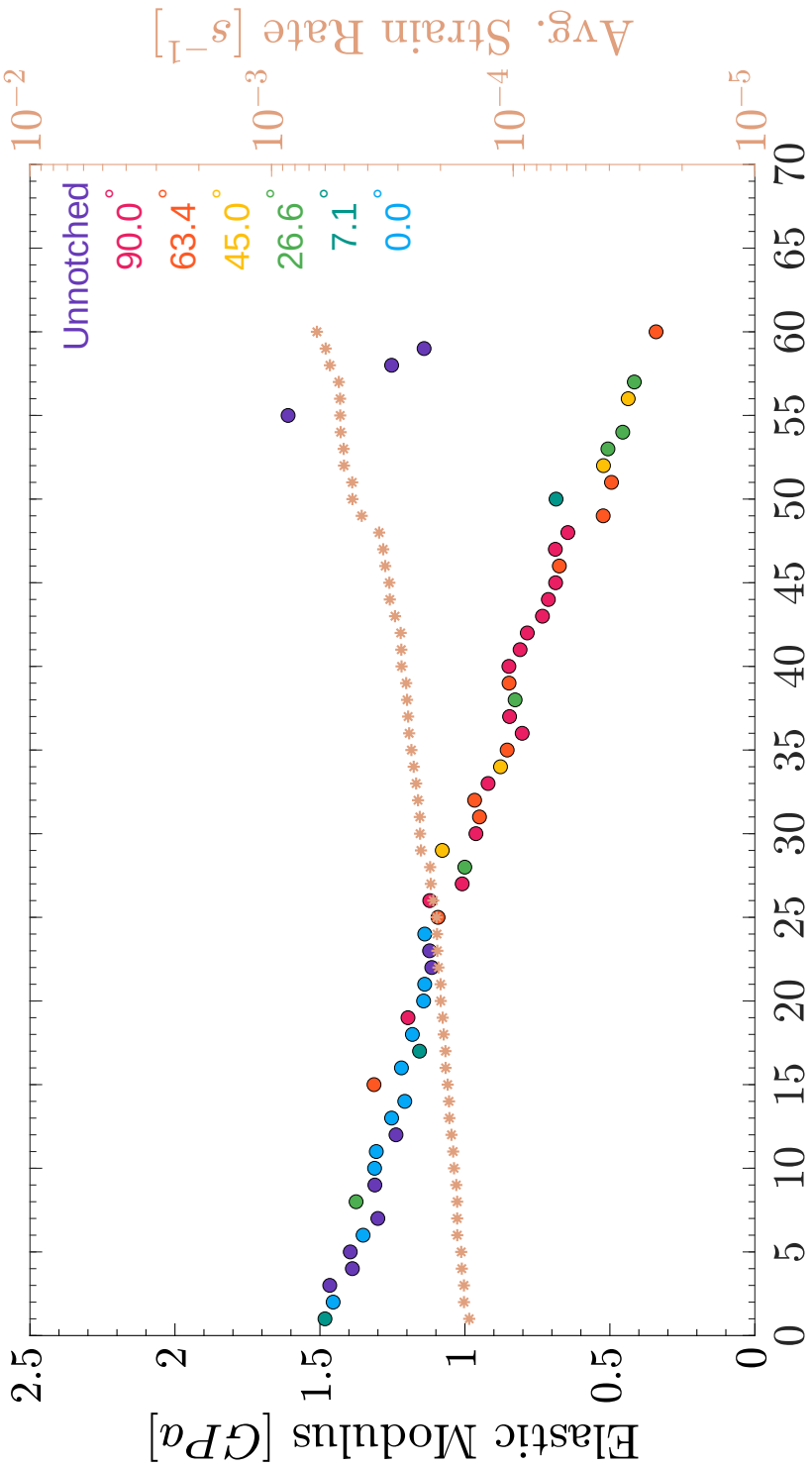

Figure B.6: Experimental data for all tested samples: Young's modulus and averaged strain rate.

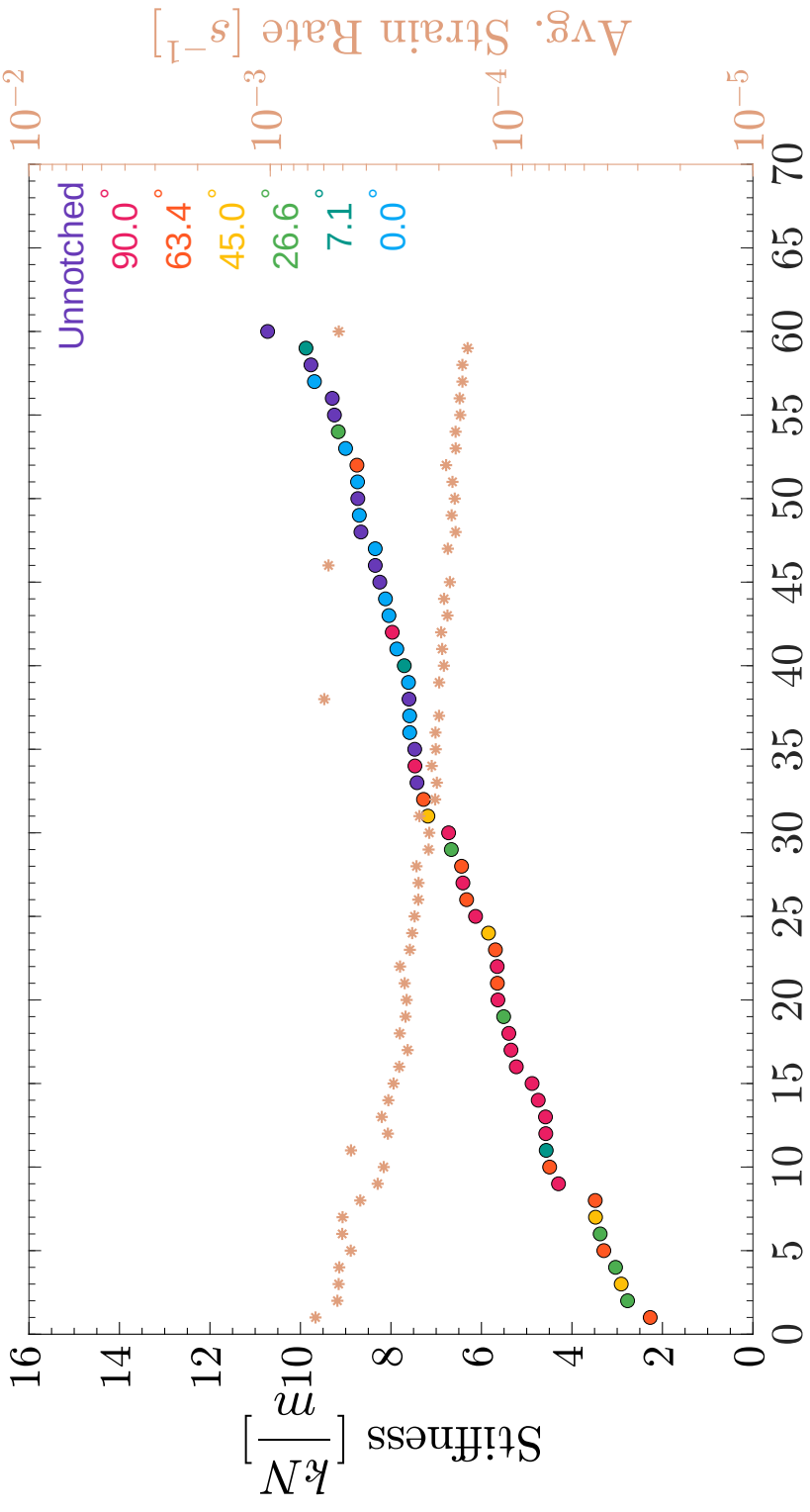

Figure B.7: Experimental data for all tested samples: stiffness and average strain rate.

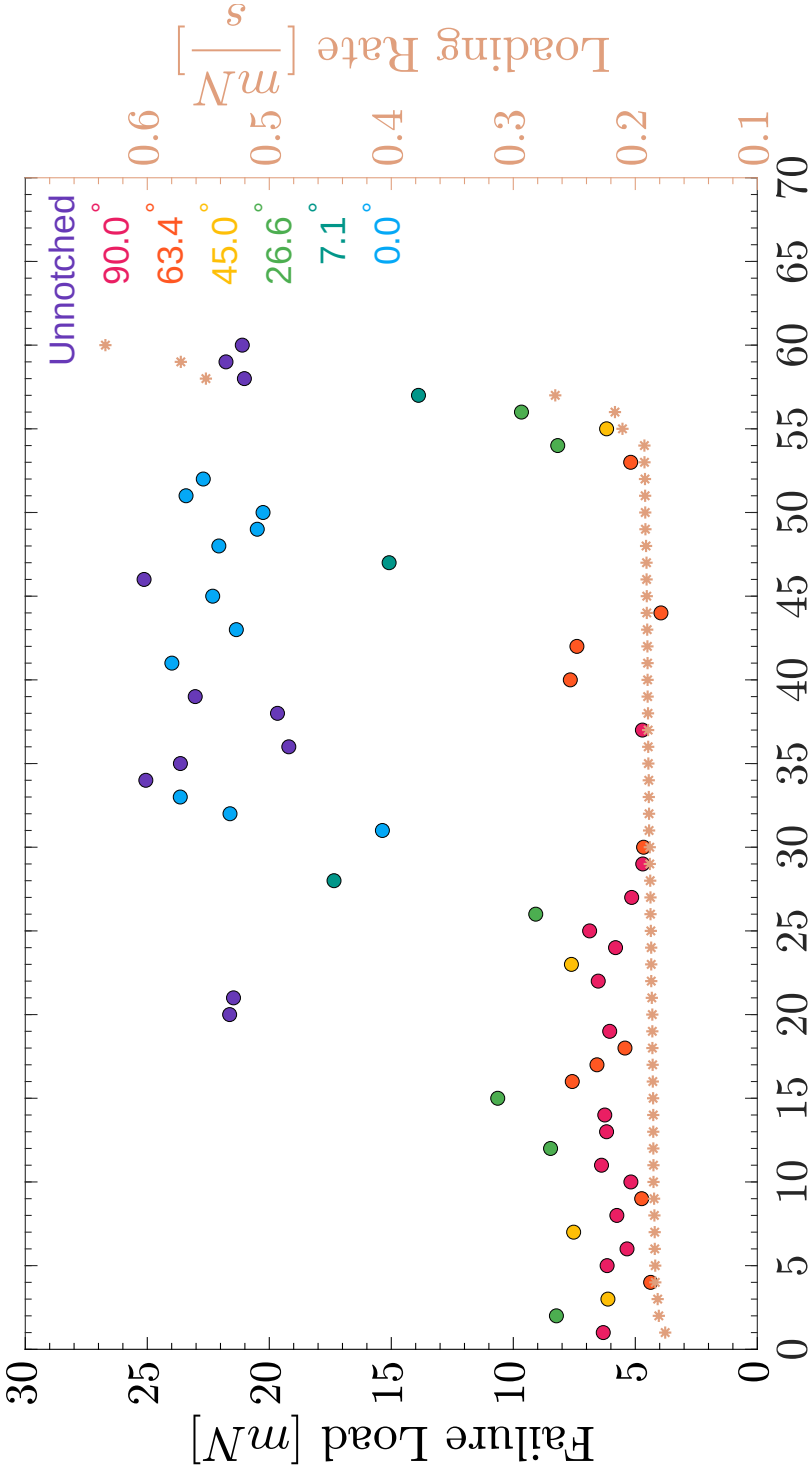

Figure B.8: Experimental data for all tested samples: Failure load and loading rate.

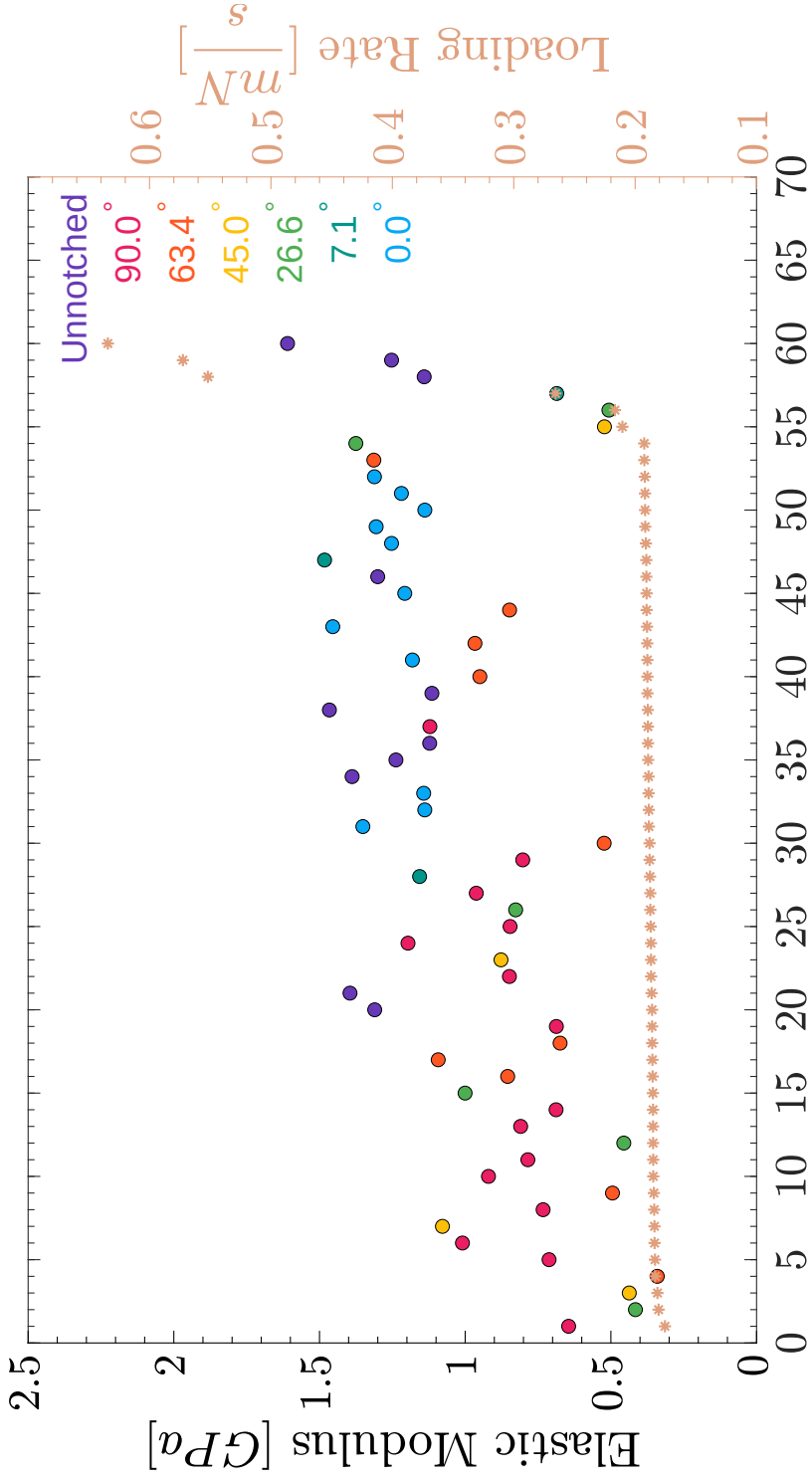

Figure B.9: Experimental data for all tested samples: Young's modulus and loading rate.

Appendix C

Details of Experimental Setup

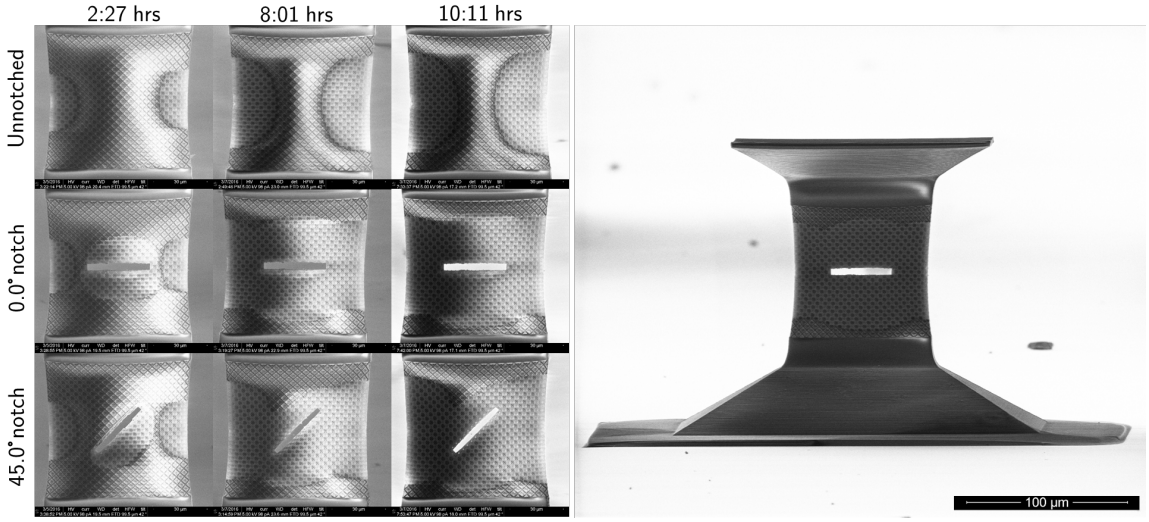

Figure C.1: Previous version of center-notched tension samples.

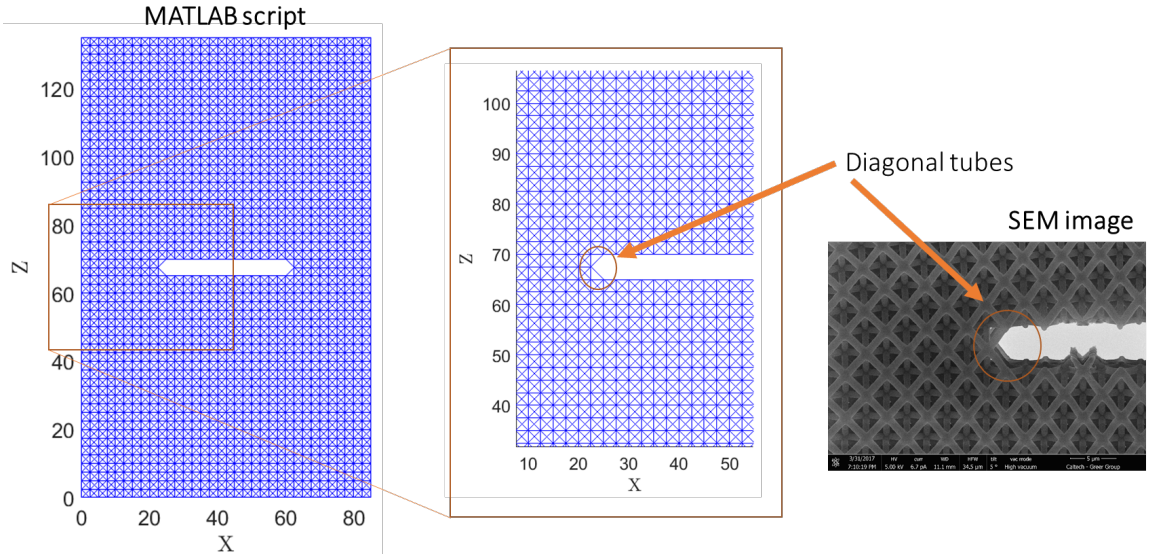

Figure C.2: MATLAB scripts allowed for geometrically-indistinguishable samples and, more importantly, reproducible notch roots, which are the locations of high stress concentrations. For example, for a 90°-notched specimen, diagonal beams are present at the node closest to the notch root. If focused-ion beam milling was used to create the notch, then the integrity of these structural elements might be compromised and the material composition at this location might change due to ion bombardment.

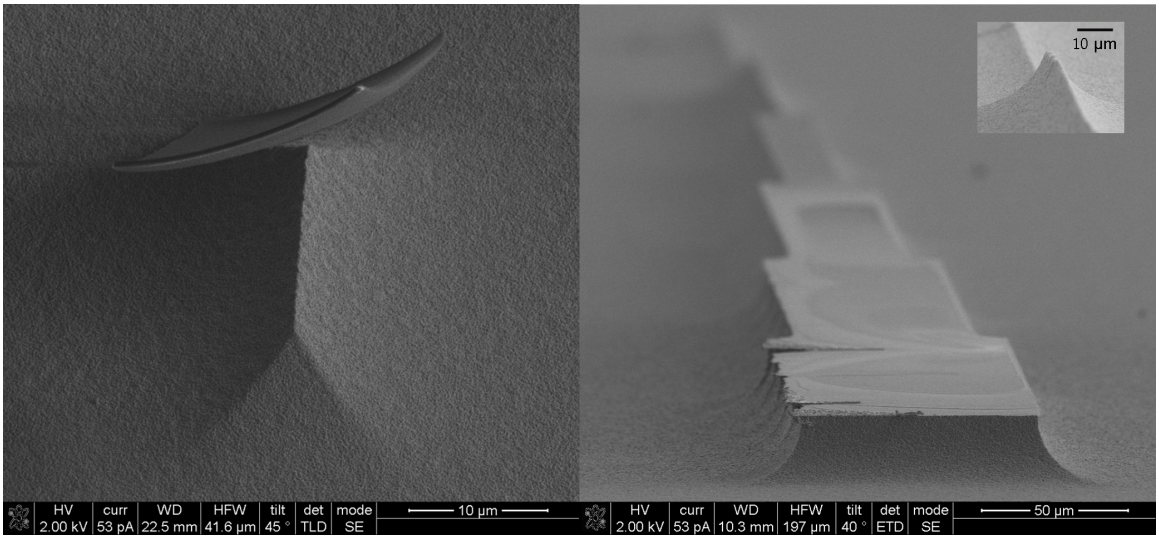

Figure C.3: XeF_2 etching enables the creation of the simple supports for three-point bending experiments at the microscale. After deposition a polymeric plate on top of a silicon substrate, XeF_2 can be used to selectively etch away the substrate and by tuning the etching parameters, a point support can be fabricated. A microscopic three-point bending specimen with a lattice architecture can then be placed on top of these supports.

Appendix D

Details of Finite Element Simulations

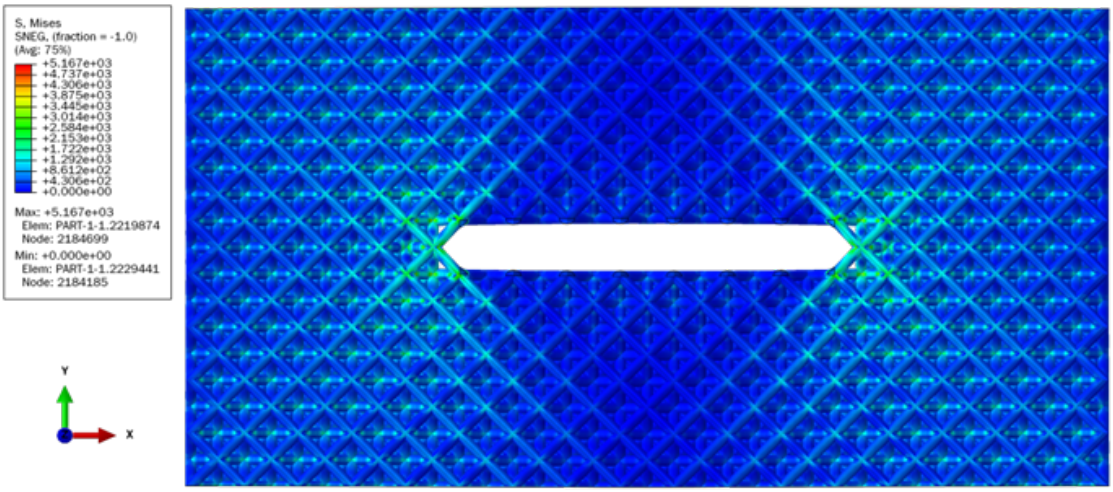

Figure D.1: Von Mises stress distribution from finite element analysis of the central region of the 90°-notched sample. The location of highest stress is at the node closest to the notch root. The finite element simulations were performed by Dr. Yong-Wei Zhang (Institute of High Performance Computing, A*STAR, Singapore) and Dr. Huang Wei (Northwestern Polytechnical University, Xian, China).

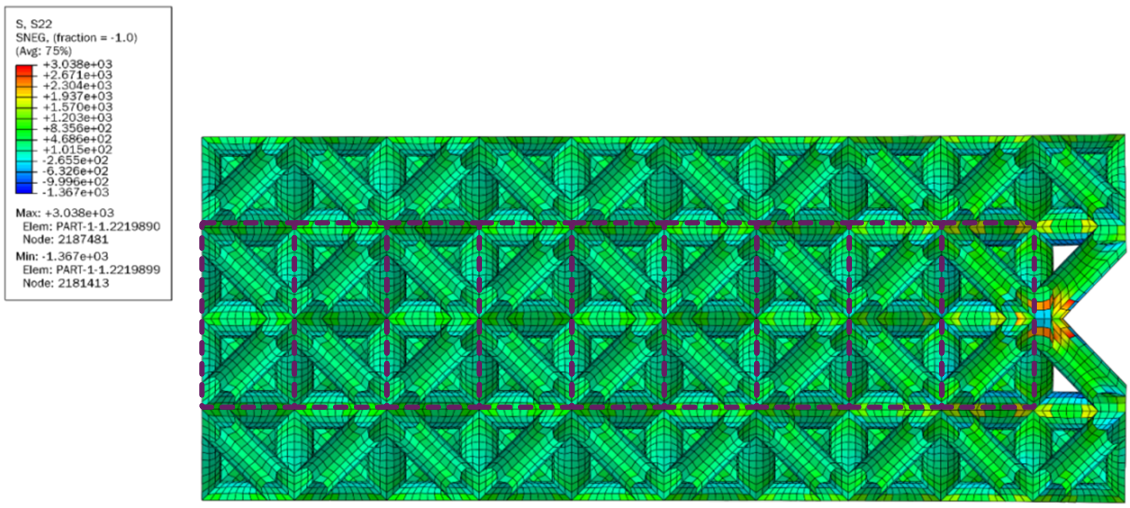

Figure D.2: To evaluate the scaling of stress with distance from the notch root, the von Mises stresses for half unit cells were averaged and plotted as a function of distance where the origin is located at the first element closest to the notch. If the different averaging area is selected, the average stresses will vary since there is a high stress concentration at the nodes; therefore, a dedicated study must be performed to assign an appropriate area. The finite element simulations were performed by Dr. Yong-Wei Zhang (Institute of High Performance Computing, A*STAR, Singapore) and Dr. Huang Wei (Northwestern Polytechnical University, Xian, China).

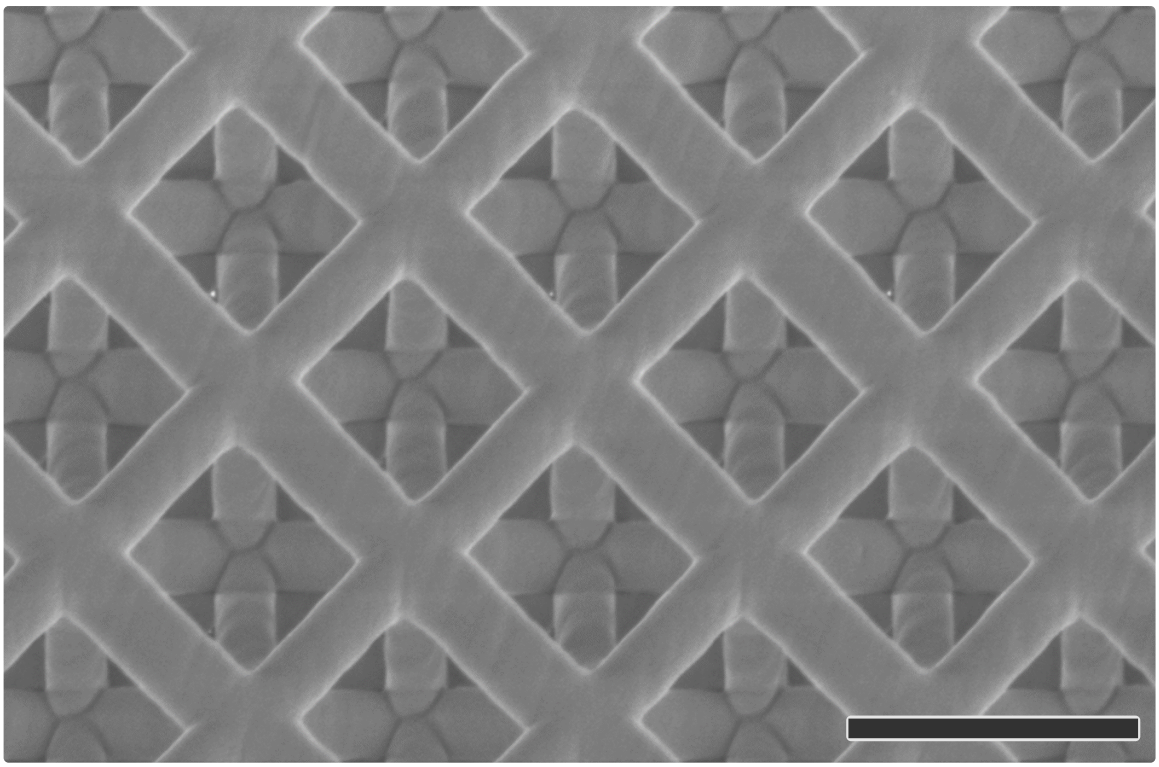

Figure D.3: The finite element simulations do not take into account the effect of the geometric and material defects on the fracture strength of nanolattices, as shown by the SEM image. It would be computationally expensive to model the details of the hollow tube intersections in the finite element model. Scale bar denotes $4\mu m$ The finite element simulations were performed by Dr. Yong-Wei Zhang (Institute of High Performance Computing, A*STAR, Singapore) and Dr. Huang Wei (Northwestern Polytechnical University, Xian, China).

Bibliography

[1] L. R. Meza, A. J. Zelhofer, N. Clarke, A. J. Mateos, D. M. Kochmann, and J. R. Greer, "Resilient 3d hierarchical architected metamaterials," *Proceedings of the National Academy of Sciences of the United States of America*, vol. 112, no. 37, pp. 11502–11507, 2015.

[2] T. A. Schaedler, A. J. Jacobsen, A. Torrents, A. E. Sorensen, J. Lian, J. R. Greer, L. Valdevit, and W. B. Carter, "Ultralight metallic microlattices," *Science*, vol. 334, no. 6058, pp. 962–965, 2011.

[3] L. Montemayor, V. Chernow, and J. R. Greer, "Materials by design: Using architecture in material design to reach new property spaces," *MRS Bulletin*, vol. 40, no. 12, p. 11221129, 2015.

[4] H. Gao, B. Ji, I. L. Jäger, E. Arzt, and P. Fratzl, "Materials become insensitive to flaws at nanoscale: Lessons from nature," *Proceedings of the National Academy of Sciences*, vol. 100, no. 10, pp. 5597–5600, 2003.

[5] A. T. Jennings, M. J. Burek, and J. R. Greer, "Microstructure versus size: Mechanical properties of electroplated single crystalline cu nanopillars," *Phys. Rev. Lett.*, vol. 104, p. 135503, Apr 2010.

[6] J. R. Greer and J. T. D. Hosson, "Plasticity in small-sized metallic systems: Intrinsic versus extrinsic size effect," *Progress in Materials Science*, vol. 56, no. 6, pp. 654 – 724, 2011. Festschrift Vaclav Vitek.

[7] J. Greer and W. Nix, "Size dependence of mechanical properties of gold at the sub-micron scale," *Applied Physics A*, vol. 80, pp. 1625–1629, May 2005.

[8] J. R. Greer, W. C. Oliver, and W. D. Nix, "Size dependence of mechanical properties of gold at the micron scale in the absence of strain gradients," *Acta Materialia*, vol. 53, no. 6, pp. 1821 – 1830, 2005.

[9] R. Dou and B. Derby, "A universal scaling law for the strength of metal micropillars and nanowires," *Scripta Materialia*, vol. 61, no. 5, pp. 524 – 527, 2009.

[10] J. R. Greer, D. Jang, and X. W. Gu, "Exploring deformation mechanisms in nanostructured materials," *JOM*, vol. 64, pp. 1241–1252, Oct 2012.

[11] M. Dietiker, S. Buzzi, G. Pigozzi, J. Lffler, and R. Spolenak, "Deformation behavior of gold nano-pillars prepared by nanoimprinting and focused ion-beam milling," *Acta Materialia*, vol. 59, no. 5, pp. 2180 – 2192, 2011.

[12] C. A. Volkert and E. T. Lilleodden, "Size effects in the deformation of sub-micron au columns," *Philosophical Magazine*, vol. 86, no. 33-35, pp. 5567–5579, 2006.

[13] D. Jang and J. R. Greer, "Size-induced weakening and grain boundary-assisted deformation in 60 nm grained ni nanopillars," *Scripta Materialia*, vol. 64, no. 1, pp. 77 – 80, 2011.

[14] B. Yang, C. Motz, M. Rester, and G. Dehm, "Yield stress influenced by the ratio of wire diameter to grain size a competition between the effects of specimen microstructure and dimension in micro-sized polycrystalline copper wires," *Philosophical Magazine*, vol. 92, no. 25-27, pp. 3243–3256, 2012.

[15] D. Z. Chen, D. Jang, K. M. Guan, Q. An, W. A. Goddard, and J. R. Greer, "Nanometallic glasses: Size reduction brings ductility, surface state drives its extent," *Nano Letters*, vol. 13, no. 9, pp. 4462–4468, 2013. PMID: 23978318.

[16] A. Koller, *Structure and Properties of Ceramics*. Elsevier, 1994.

[17] L. Montemayor, L. R. Meza, and J. R. Greer, "Design and fabrication of hollow rigid nanolattices via twophoton lithography.," *Advanced Engineering Materials*, vol. 16, no. 2, pp. 184–189, 2014.

[18] X. W. Gu, Z. Wu, Y.-W. Zhang, D. J. Srolovitz, and J. R. Greer, "Microstructure versus flaw: Mechanisms of failure and strength in nanostructures," *Nano Letters*, vol. 13, no. 11, pp. 5703–5709, 2013. PMID: 24168654.

[19] J. A.J., B. W., and N. S., "Microscale truss structures formed from selfpropagating photopolymer waveguides," *Advanced Materials*, vol. 19, no. 22, pp. 3892–3896, 2007.

[20] A. J. Jacobsen, W. Barvosa-Carter, and S. Nutt, "Micro-scale truss structures with three-fold and six-fold symmetry formed from self-propagating polymer waveguides," *Acta Materialia*, vol. 56, no. 11, pp. 2540 – 2548, 2008.

[21] H.-B. Sun and S. Kawata, *Two-Photon Photopolymerization and 3D Lithographic Microfabrication*, pp. 169–273. Berlin, Heidelberg: Springer Berlin Heidelberg, 2004.

[22] W. Xiong, Y. Zhou, W. Hou, L. Jiang, M. Mahjouri-Samani, J. Park, X. He, Y. Gao, L. Fan, T. Baldacchini, J.-F. Silvain, and Y. Lu, "Laser-based micro/nanofabrication in one, two and three dimensions," *Frontiers of Optoelectronics*, vol. 8, pp. 351–378, Dec 2015.

[23] A. Torrents, T. Schaedler, A. Jacobsen, W. Carter, and L. Valdevit, "Characterization of nickel-based microlattice materials with structural hierarchy from the nanometer to the millimeter scale," *Acta Materialia*, vol. 60, no. 8, pp. 3511 – 3523, 2012.

[24] X. Zheng, H. Lee, T. H. Weisgraber, M. Shusteff, J. DeOtte, E. B. Duoss, J. D. Kuntz, M. M. Biener, Q. Ge, J. A. Jackson, S. O. Kucheyev, N. X. Fang, and C. M. Spadaccini, "Ultralight, ultrastiff mechanical metamaterials," *Science*, vol. 344, no. 6190, pp. 1373–1377, 2014.

[25] X. Zheng, W. Smith, J. Jackson, B. Moran, H. Cui, D. Chen, J. Ye, N. Fang, N. Rodriguez, W. T., and C. Spadaccini, "Multiscale metallic metamaterials," *Nature Materials*, vol. 15, p. 11001106, 2016.

[26] R. Jan, V. Lorenzo, S. T. A., J. A. J., C. W. B., and G. J. R., "Fabrication and deformation of metallic glass microlattices," *Advanced Engineering Materials*, vol. 16, no. 7, pp. 889–896, 2014.

[27] F. Joachim and W. Martin, "Threedimensional optical laser lithography beyond the diffraction limit," *Laser & Photonics Reviews*, vol. 7, no. 1, pp. 22–44, 2013.

[28] M. Ashby, "Designing architectured materials," *Scripta Materialia*, vol. 68, no. 1, pp. 4 – 7, 2013. Architectured Materials.

[29] X. W. Gu and J. R. Greer, "Ultra-strong architected cu meso-lattices," *Extreme Mechanics Letters*, vol. 2, pp. 7 – 14, 2015.

[30] L. R. Meza, S. Das, and J. R. Greer, "Strong, lightweight, and recoverable three-dimensional ceramic nanolattices," *Science*, vol. 345, no. 6202, pp. 1322–1326, 2014.

[31] L. C. Montemayor, W. H. Wong, Y.-W. Zhang, and J. R. Greer, "Insensitivity to flaws leads to damage tolerance in brittle architected meta-materials," *Scientific Reports*, vol. 6, p. 20570, 2016.

[32] J. Bauer, A. Schroer, R. Schwaiger, and O. Kraft, "The impact of size and loading direction on the strength of architected lattice materials," *Advanced Engineering Materials*, vol. 18, no. 9, pp. 1537–1543, 2016.

[33] R. S. Farr and Y. Mao, "Fractal space frames and metamaterials for high mechanical efficiency," *EPL (Europhysics Letters)*, vol. 84, no. 1, p. 14001, 2008.

[34] H. Wadley, "Multifunctional periodic cellular metals," *Philosophical Transactions of the Royal Society of London A: Mathematical, Physical and Engineering Sciences*, vol. 364, no. 1838, pp. 31–68, 2006.

[35] L. Montemayor and J. R. Greer, "Mechanical response of hollow metallic nanolattices: Combining structural and material size effects.," *J. Appl. Mech.*, vol. 82, no. 7, pp. 071012–071012, 2015.

[36] L. J. Gibson and M. F. Ashby, *Cellular Solids*. Cambridge University Press, 1999.

[37] A. Evans, J. Hutchinson, N. Fleck, M. Ashby, and H. Wadley, "The topological design of multifunctional cellular metals," *Progress in Materials Science*, vol. 46, no. 3, pp. 309 – 327, 2001.

[38] N. A. Fleck, V. S. Deshpande, and M. F. Ashby, "Micro-architectured materials: past, present and future," *Proceedings of the Royal Society of London A: Mathematical, Physical and Engineering Sciences*, vol. 466, no. 2121, pp. 2495–2516, 2010.

[39] V. Deshpande, N. Fleck, and M. Ashby, "Effective properties of the octet-truss lattice material," *Journal of the Mechanics and Physics of Solids*, vol. 49, no. 8, pp. 1747 – 1769, 2001.

[40] V. Deshpande, M. Ashby, and N. Fleck, "Foam topology: bending versus stretching dominated architectures," *Acta Materialia*, vol. 49, no. 6, pp. 1035 – 1040, 2001.

[41] S. Krödel, T. Delpero, A. Bergamini, P. Ermanni, and D. M. Kochmann, "3d auxetic microlattices with independently controllable acoustic band gaps and quasi-static elastic moduli," *Advanced Engineering Materials*, vol. 16, no. 4, pp. 357–363, 2014.

[42] G. von Freymann, A. Ledermann, M. Thiel, I. Staude, S. Essig, K. Busch, and M. Wegener, "Three-dimensional nanostructures for photonics," *Advanced Functional Materials*, vol. 20, no. 7, pp. 1038–1052, 2010.

[43] I. Quintana-Alonso and N. A. Fleck, *Fracture of Brittle Lattice Materials: A Review*, pp. 799–816. Dordrecht: Springer Netherlands, 2010.

[44] H. C. Tankasala, V. S. Deshpande, and N. A. Fleck, "Crack-tip fields and toughness of two-dimensional elastoplastic lattices," *Journal of Applied Mechanics*, vol. 82, no. 9, p. 091004, 2015.

[45] H. Tankasala, V. Deshpande, and N. Fleck, "Tensile response of elastoplastic lattices at finite strain," *Journal of the Mechanics and Physics of Solids*, 2017.

[46] S. Maiti, M. Ashby, and L. Gibson, "Fracture toughness of brittle cellular solids," *Scripta Metallurgica*, vol. 18, no. 3, pp. 213 – 217, 1984.

[47] N. E. Romijn and N. A. Fleck, "The fracture toughness of planar lattices: Imperfection sensitivity," *Journal of the Mechanics and Physics of Solids*, vol. 55, no. 12, pp. 2538 – 2564, 2007.

[48] S. Choi and B. V. Sankar, "A micromechanical method to predict the fracture toughness of cellular materials," *International Journal of Solids and Structures*, vol. 42, no. 5, pp. 1797 – 1817, 2005.

[49] B. Rasto and G. D. J., "Factors controlling the fracture resistance of brittle cellular materials," *Journal of the American Ceramic Society*, vol. 74, no. 5, pp. 1061–1065, 1991.

[50] B. Rasto and G. D. J., "Fracture behavior of opencell ceramics," *Journal of the American Ceramic Society*, vol. 72, no. 7, pp. 1145–1152, 1989.

[51] J. Huang and L. Gibson, "Fracture toughness of brittle honeycombs," *Acta Metallurgica et Materialia*, vol. 39, no. 7, pp. 1617 – 1626, 1991.

[52] J. Huang and L. Gibson, "Fracture toughness of brittle foams," *Acta Metallurgica et Materialia*, vol. 39, no. 7, pp. 1627 – 1636, 1991.

[53] W. A. Curtin and H. Scher, "Mechanics modeling using a spring network," *Journal of Materials Research*, vol. 5, no. 3, p. 554562, 1990.

[54] M. Berdova, T. Ylitalo, I. Kassamakov, J. Heino, P. T. Trm, L. Kilpi, H. Ronkainen, J. Koskinen, E. Hggstrm, and S. Franssila, "Mechanical assessment of suspended ald thin films by bulge and shaft-loading techniques," *Acta Materialia*, vol. 66, pp. 370 – 377, 2014.

[55] F. Hofmann, E. Tarleton, R. J. Harder, N. W. Phillips, P.-W. Ma, J. N. Clark, I. K. Robinson, B. Abbey, W. Liu, and C. E. Beck, "3d lattice distortions and defect structures in ion-implanted nano-crystals," *Scientific Reports*, vol. 7, p. 45993, 2017.

[56] D. Kiener, C. Motz, M. Rester, M. Jenko, and G. Dehm, "Fib damage of cu and possible consequences for miniaturized mechanical tests," *Materials Science and Engineering: A*, vol. 459, no. 1, pp. 262 – 272, 2007.

[57] S. Shim, H. Bei, M. Miller, G. Pharr, and E. George, "Effects of focused ion beam milling on the compressive behavior of directionally solidified micropillars and the nanoindentation response of an electropolished surface," *Acta Materialia*, vol. 57, no. 2, pp. 503 – 510, 2009.

[58] L. Valdevit, S. W. Godfrey, T. A. Schaedler, A. J. Jacobsen, and W. B. Carter, "Compressive strength of hollow microlattices: Experimental characterization, modeling, and optimal design," *Journal of Materials Research*, vol. 28, no. 17, pp. 2461–2473, 2013.

[59] L. R. Meza, G. Phlipot, C. M. Portela, A. Maggi, L. C. Montemayor, A. Comella, D. M. Kochmann, and J. R. Greer, "Reexamining the mechanical property space of three-dimensional lattice architectures," *Acta Materialia*, pp. –, 2017.

[60] W. Weibull, "A statistical distribution function of wide applicability," *Journal of Applied Mechanics*, vol. 18, p. 293297, 1951.

[61] B. Lawn, *Fracture of Brittle Solids*. Cambridge University Press, 1993.

[62] J. Wachtman, W. R. Cannon, and M. J. Matthewson, *Mechanical Properties of Ceramics*. Wiley, 2009.

[63] M. W. Barsoum, *Fundamentals of Ceramics*. McGraw Hill, 1997.

[64] R. W. Davidge, *Mechanical Behavior of Ceramics*. Cambridge University Press, 1979.

[65] A. Bruhner-Foit and D. Munz, "Statistical analysis of flexure strength data," *International Energy Agency Annex II*, 1989.

[66] V. Rontu, A. Nolvi, A. Hokkanen, E. Haeggstrm, I. Kassamakov, and S. Franssila, "Elastic and fracture properties of free-standing amorphous ald al2o3 thin films measured with bulge test," *Materials Research Express*, vol. 5, no. 4, p. 046411, 2018.

[67] M. I. Putkonen, "Ald applications beyond outside ic technology - existing and emerging possibilities," *ECS Transactions*, vol. 25, no. 4, pp. 143–155, 2009.

[68] D. Broek, *Elementary Engineering Fracture Mechanics*. Springer, 1982.

[69] M. R. Begley and J. W. Hutchinson, *The Mechanics and Reliability of Films, Multilayers and Coatings*. Cambridge University Press, 2017.

[70] K. Wallin, "The scatter in kic-results," *Engineering Fracture Mechanics*, vol. 19, no. 6, pp. 1085 – 1093, 1984.

[71] D. Gross and T. Seelig, *Fracture Mechanics*. Springer, 2011.

[72] S. D. J., A. M. R., and P. M. J., "The role of tstress in brittle fracture for linear elastic materials under mixedmode loading," *Fatigue & Fracture of Engineering Materials & Structures*, vol. 24, no. 2, pp. 137–150, 2000.

[73] F. Erdogan and G. C. Sih, "On the crack extension in plates under plane loading and transverse shear," *Journal of Basic Engineering*, vol. 85, no. 4, pp. 519–525, 1963.

[74] D. Gross, *Some Remarks on the History of Fracture Mechanics*, pp. 195–209. Berlin, Heidelberg: Springer Berlin Heidelberg, 2014.

[75] B. Cotterell, "The past, present, and future of fracture mechanics," *Engineering Fracture Mechanics*, vol. 69, no. 5, pp. 533 – 553, 2002.

[76] S. Timoshenko and J. M. Gere, *Theory of elastic stability.* New York: McGraw-Hill, 1961.

[77] D. Jang, L. R. Meza, F. Greer, and J. R. Greer, "Fabrication and deformation of three-dimensional hollow ceramic nanostructures," *Nature Materials*, vol. 12, p. 893898, 2013.

[78] L. R. Meza and J. R. Greer, "Mechanical characterization of hollow ceramic nanolattices," *Journal of Materials Science*, vol. 49, pp. 2496–2508, Mar 2014.

[79] L. Salari-Sharif, T. A. Schaedler, and L. Valdevit, "Energy dissipation mechanisms in hollow metallic microlattices," *Journal of Materials Research*, vol. 29, no. 16, pp. 1755–1770, 2014.

[80] R. O. Ritchie, "The conflicts between strength and toughness," *Nature Materials*, vol. 10, pp. 817–822, 2011.

[81] B. N. Jaya, C. Kirchlechner, and G. Dehm, "Can microscale fracture tests provide reliable fracture toughness values? a case study in silicon," *Journal of Materials Research*, vol. 30, no. 5, pp. 686–698, 2015.

[82] C. E. Feddersen, "Evaluation and prediction of the residual strength of center cracked tension panels," *ASTM*, vol. STP486, 1971.

[83] A. F. Liu, *Mechanics and Mechanisms of Fracture.* Technology and Engineering, 2005.

[84] C. E. Feddersen and W. S. Hyler, "Fracture and fatigue-crack propagation characteristics of 7075-t7351 aluminum alloy sheet and plate," *Battelle Memorial Institute to Naval Air Development Center*, vol. N00156-68-C-1344, 1970.

[85] P. Kuhn, "Residual strength in the presence of fatigue cracks," *Advisory Group tor Aeronautical Research and Developmen*, vol. Structures and Materials Panel, 1967.

[86] P. Kuhn and I. E. Figge, "Unified notch-strength analysis for wrought aluminum alloys," *NASA*, no. TN-D-125, 1962.